

PFC/RR-90-8

**A Method For Estimating Tokamak Poloidal Field Coil
Currents Which Incorporates Engineering Constraints**

Stewart, William A.

May 1990

Plasma Fusion Center
Massachusetts Institute of Technology
Cambridge, Massachusetts 02139 USA

This work was supported by the author and his family. Reproduction, translation, publication, use and disposal, in whole or in part, by or for the United States government is permitted.

A Method For Estimating Tokamak Poloidal Field Coil Currents Which Incorporates Engineering Constraints

by

William Andrew Stewart

B.S., Carnegie-Mellon University (1985)

Submitted to the Department of Nuclear Engineering
in partial fulfillment of the requirements for the degrees of

Nuclear Engineer

and

Master of Science in Nuclear Engineering

at the

MASSACHUSETTS INSTITUTE OF TECHNOLOGY

June 1990

© William A. Stewart, 1990

The author hereby grants to MIT permission to reproduce and
to distribute copies of this thesis document in whole or in part.

Signature of Author _____
Department of Nuclear Engineering
May 15, 1990

Certified by _____
Jeffrey P. Freidberg
Professor, Department of Nuclear Engineering
Thesis Supervisor

Accepted by _____
Allan F. Henry
Chairman, Departmental Committee on Graduate Students

A Method For Estimating Tokamak Poloidal Field Coil Currents Which Incorporates Engineering Constraints

by

William Andrew Stewart

Submitted to the Department of Nuclear Engineering
on May 15, 1990, in partial fulfillment of the
requirements for the degrees of
Nuclear Engineer
and
Master of Science in Nuclear Engineering

Abstract

This thesis describes the development of a design tool for the poloidal field magnet system of a tokamak. Specifically, an existing program for determining the poloidal field coil currents has been modified to: (1) support the general case of asymmetric equilibria and coil sets, (2) determine the coil currents subject to constraints on the maximum values of those currents, and (3) determine the coil currents subject to limits on the forces those coils may carry. The equations representing the current limits and coil force limits are derived and an algorithm based on Newton's method is developed to determine a set of coil currents which satisfies those limits. The resulting program allows the designer to quickly determine whether or not a given coil set is capable of supporting a given equilibrium.

Thesis Supervisor: Jeffrey P. Freidberg
Title: Professor, Department of Nuclear Engineering

Thesis Reader: S. Pekka Hakkarainen
Title: Research Scientist

Acknowledgments

I would like to thank the many people who have helped me complete my education at MIT.

First, I would like to thank my thesis supervisor, Professor Jeffrey P. Freidberg, who originally proposed this project and allowed me to pursue it to my own satisfaction. Through his classes and our conversations, he has always challenged and inspired me, and I am indebted to him for his advice and support throughout my career at MIT.

I would also like to thank Dr. Scott Haney and Dr. S. Pekka Hakkarainen. Dr. Haney's thesis research provided the foundation upon which this thesis is built, and his help in clarifying many of the subtle points in his derivations has proven immeasurable. I would also like to thank him for his impeccable programming style, which greatly eased the amount of work I had to perform to decipher his programs. Dr. Hakkarainen gave me day-to-day support during the period while I was developing the primary algorithm used in this thesis. Additionally, his own work on the minimization problem discussed here clarified many of the issues involved in solving this class of problems.

Next, I would like to thank my friends at the MIT Plasma Fusion Center for the good times we have shared both at and away from work. These include: Dr. Martin Greenwald, Sean Barnett, Justin Schwartz, Manos Chaniotakis, Scott Peng, Warren Krueger, Bob Bieri and Tom and Sue Hsu. In their own way, each of these people has made my experience here quite enjoyable and fun.

Finally, I would like to thank my parents, my brothers, my sister-in-law, my grandparents and all of my far-flung relatives for their concern and good wishes during my stay here. Additionally, I would like to thank my friends Ken and Alysa Studley, Tom and Anna Kovalcik, and Glenn Joyce.

This work is dedicated to my beloved fiancé, Donna Nichols, for her patience, love, support and incredible understanding throughout my education.

Contents

1	Introduction	15
1.1	Some Basic Plasma Physics	16
1.2	The Poloidal Field System	19
1.3	Estimating PF Coil Currents	20
1.4	Extension to Asymmetric Systems	21
1.5	Current Constraints	21
1.6	Force Constraints	21
2	Review of Coil Current Solver	23
2.1	Introduction	23
2.2	Problem Statement	24
2.3	Calculation of the Vacuum Field	28
2.3.1	Simplification of Green's Theorem	29
2.3.2	Conductor Grouping	30
2.3.3	Fourier Analysis	31
2.4	Solution for Group Currents	33
2.5	Summary	34
3	Asymmetric Systems	37
3.1	Discussion	37
3.2	Generalization	39
3.3	Verification	41
3.4	Validation	45

4	Linear Constraints	55
4.1	The Source of the Constraints	55
4.1.1	Resistive Magnets	55
4.1.2	Superconducting Magnets	57
4.2	Problem Statement	57
4.3	Finding a Feasible Point	59
4.4	Numerical Implementation	60
4.5	Avoiding Singularities	62
4.6	Verification, Validation, and Testing	63
4.7	Discussion	69
5	Forces on PF Coils	73
5.1	The Vector Potential	73
5.1.1	Vector Potential of a Distributed Current	74
5.1.2	Filamentary Currents	74
5.2	Magnetic Energy of a System of Currents	75
5.2.1	Two Distributed Currents	75
5.2.2	A Single Distributed Current	76
5.2.3	Two Filamentary Currents	76
5.2.4	A Single Filamentary Current	76
5.3	Force Computations	77
5.3.1	Force Between Two Distributed Currents	78
5.3.2	Self Force of a Distributed Current	79
5.3.3	Force Between Two Filamentary Currents	79
5.3.4	Self Force of a Filamentary Current	79
5.4	Modelling the Coil-Coil Forces	80
5.5	Plasma-Coil Interaction Forces	86
5.5.1	The Scalar Potential	87
5.5.2	Gradient of the Scalar Potential	88
5.6	Plasma Force Equations	90
6	Nonlinear Constraints	91
6.1	The Source of the Constraints	91

CONTENTS	9
6.2 Formulation of the Constraint Equations	92
6.3 Verification, Validation, and Testing	95
6.4 Constraining Grouped Currents	99
6.5 Combining Constraints	107
7 Conclusions and Recommendations	111
A Verification of Asymmetric Program	113
A.1 Case 1: A Conventional Tokamak	113
A.2 Case 2: An Elongated Tokamak	117
B Alcator C-Mod Coil Set	121
C Symmetry Relations	131
C.1 Symmetry of $G(r, z; r', z')$	131
C.1.1 Exchange of r and r'	132
C.1.2 Exchange of z and z'	132
C.1.3 Results	133
C.2 Symmetry of $U_{j \rightarrow i}$	133
C.3 Symmetry of M_{ij}	134
D Derivation of the Intercoil Force Expressions	135
D.1 Filamentary Currents	136
D.1.1 Force Between Two Coils	136
D.1.2 Self Force of a Filamentary Current	138
D.2 Distributed Currents	139
D.2.1 Force Between Two Coils	139
D.2.2 Self Force of a Distributed Current	140
E Gaussian Quadrature	141

List of Figures

1-1	Geometry of a simple screw pinch.	17
1-2	Geometry and coils of an ohmically heated tokamak.	19
2-1	Geometry of the plasma surface and conductors for use in the poloidal field coil current calculation	25
3-1	Example of a symmetric plasma and coil set	38
3-2	Tangential poloidal field for the equilibrium presented in Figure 3-1	38
3-3	Example of a single null diverted plasma	40
3-4	Tangential poloidal field of the single null plasma shown in Figure 3-3	40
3-5	Plasma and coil set for the proposed Versator upgrade	42
3-6	Poloidal fields for the Versator test case	44
3-7	Symmetric filament model of plasma current	46
3-8	Poloidal fields for symmetric test case	48
3-9	Flux surface for the asymmetric case	50
3-10	Poloidal field for the asymmetric test case	52
3-11	Alcator C-Mod single null test case	52
3-12	Poloidal fields of the Alcator C-Mod single null case	53
4-1	Alcator C-Mod equilibrium and coil set	64
4-2	Poloidal fields for the unconstrained case	65
4-3	Poloidal fields for one active constraint	66
4-4	Poloidal fields for the case of two active constraints	67
4-5	Poloidal fields for two active constraints and one inactive constraint	68
4-6	Poloidal fields for the case of two active and two inactive constraints	69

5-1	Simple coil model for computing the magnetic energy	75
5-2	Radial components of the force coefficient for an axially displaced coil	81
5-3	Axial components of the force coefficient for an axially displaced coil	81
5-4	Relative difference of the radial force coefficients for an axially displaced coil	82
5-5	Relative difference of the axial force coefficients for an axially displaced coil	82
5-6	Radial components of the force coefficient for a coil of varying radius	83
5-7	Axial components of the force coefficient for a coil of varying radius	84
5-8	Radial component of the relative difference for a coil with a varying radius	84
5-9	Axial component of the relative difference for a coil with a varying radius	85
6-1	Alcator C-Mod coil set and equilibrium	96
6-2	Poloidal fields for the unconstrained case	97
6-3	Poloidal fields for one force constraint	98
6-4	Poloidal fields for the case of two force constraints	100
6-5	Poloidal fields for the case of three force constraints	101
6-6	Poloidal fields for the case of four force constraints.	102
6-7	Poloidal fields for a force constraint on a set of grouped coils	104
6-8	Poloidal fields for a constrained set of grouped coils	105
6-9	Poloidal fields for the case of a constrained set of grouped coils	106
6-10	Poloidal fields for the previous case with the grouping removed	108
6-11	Poloidal fields for the general case of current and force constraints	109
A-1	A conventional tokamak coil set and circular plasma	114
A-2	Poloidal fields for the conventional tokamak test case	116
A-3	Highly elongated tokamak plasma and coil set.	117
A-4	Poloidal fields for the highly elongated tokamak test case	119
E-1	Self-force coefficient as a function of the number of quadrature points used.	143

List of Tables

3.1	Equilibrium parameters used for the Versator equilibrium.	42
3.2	Grouped coil results for the Versator test case	43
3.3	Ungrouped coil results for the Versator case	43
3.4	Input plasma filament currents for the symmetric test case	46
3.5	Input poloidal field coil currents for cPFC validation	47
3.6	Symmetric test case coil current comparison	49
3.7	Input plasma filament currents for the asymmetric test case	49
3.8	Asymmetric test case coil current comparison	51
3.9	Equilibrium parameters for the Alcator single null equilibrium.	53
4.1	Equilibrium data for the Alcator C-Mod test case.	64
4.2	Summary of the test results for the linear constraint algorithm	70
6.1	Equilibrium data for the Alcator C-Mod test case.	96
6.2	Unconstrained coil forces and currents.	97
6.3	Coil forces and currents for one force constraint	98
6.4	Coil forces and currents for the case of two force constraints.	100
6.5	Coil forces and currents for the case of three force constraints.	101
6.6	Coil forces and currents for the case of four force constraints.	102
6.7	Coil forces and currents for grouped coils subject to a force constraint.	104
6.8	Coil forces and currents for grouped coils subject to force constraints.	105
6.9	Coil forces and currents for the case of constrained grouped coils.	106
6.10	Coil forces and currents for the previous case with ungrouped coils.	108
6.11	Coil forces and currents for the general case of current and force constraints. . .	109

A.1	Equilibrium data for the conventional tokamak test case.	114
A.2	Grouped coil results for the conventional tokamak	115
A.3	Ungrouped coil results for the conventional tokamak case	115
A.4	Equilibrium data for the highly elongated tokamak.	118
A.5	Grouped coil results for the highly elongated tokamak	118
A.6	Ungrouped coil results for the highly elongated tokamak	119
B.1	EF1U and EF1L wire locations.	122
B.2	EF2U and EF2L wire locations.	123
B.3	EF3U and EF3L wire locations.	124
B.4	EFCU and EFCL wire locations.	125
B.5	EF4U and EF4L wire locations.	126
B.6	OH2U and OH2L wire locations.	127
B.7	Wire locations of the OH1 ohmic transformer.	128
B.7	Continued	129
B.7	Continued	130

Chapter 1

Introduction

This thesis is concerned with the development of a design tool for the poloidal field magnet system of a tokamak. Currently, the design process for these systems proceeds along the following lines:

1. The desired plasma physics parameters are determined.
2. From these parameters, the poloidal field necessary to support the desired equilibrium is found.
3. The magnet positions are estimated from the required poloidal field.
4. Once the magnet positions have been determined, the rest of the engineering requirements (i.e. coil currents and forces) are found.
5. Steps 1 through 4 are iterated until the design is finalized.

Because of the complexity of a tokamak, the computer programs available to assist in the design process are quite complex themselves. This complexity makes these tools difficult to learn and use. Additionally, they are often quite slow, requiring anywhere from minutes to hours of processing time on a supercomputer. The result of all this is that a methodical scan over the range of physics parameters for a single design iteration is quite tedious. Furthermore, if a particular iteration is at an early phase in the design process, much of the detailed information produced by these programs may be unnecessary.

The slow execution times of the aforementioned programs arise from their general approach to the problem. They attempt to solve the equations describing the system as accurately and completely as possible. Haney [12] proposed that a tokamak designer might find a set of fast

tools valuable for the first few iterations of the design process. The speed of these tools is achieved by sacrificing some of the accuracy of the solution, although in practice the differences between the fast and standard methods are only a few percent [15]. Once an advanced design is ready, it can be verified using the more accurate tools.

The design tool described herein is built on Haney's method for estimating the currents in the poloidal field magnets [13]. Here, his method will be extended to satisfy the following constraints:

- Realism, specifically the ability to model up-down asymmetric configurations
- The maximum current flowing in a coil
- The maximum force acting on a coil

The realism constraint is more conceptual than physical. The original implementation of Haney's method was applicable only to a limited subset of tokamak configurations. The removal of that limit is the subject of Chapter 3. Finding the coil currents necessary to support an equilibrium subject to limits on the maximum current flowing in those coils is the subject of Chapter 4. To determine the coil currents such that the limits on the forces acting on the coils first requires finding the forces acting on those coils. The derivation of the expressions for the coil forces is presented in Chapter 5, and determining the coil currents such that the limits on the coil forces are satisfied is discussed in Chapter 6. Further introduction to these topics is given later in this chapter. First though, it is necessary to briefly discuss the relevant plasma physics and describe the poloidal field system in detail.

1.1 Some Basic Plasma Physics

The plasma physics required to design a tokamak is contained in the theory of ideal magnetohydrodynamics (MHD). Solving these equations for a given set of plasma parameters fixes the boundary conditions required to solve these equations. These boundary conditions, in turn, make it possible to estimate the currents in the poloidal field magnets.

The MHD equations describing a static plasma equilibrium are [3]:

$$\mathbf{J} \times \mathbf{B} = \nabla p \quad (1.1)$$

$$\nabla \times \mathbf{B} = \mu_0 \mathbf{J} \quad (1.2)$$

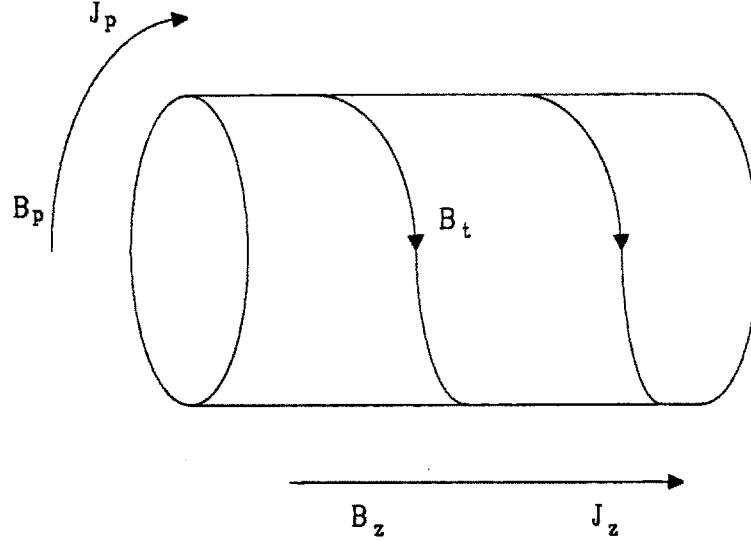


Figure 1-1: Geometry of a simple screw pinch.

$$\nabla \cdot \mathbf{B} = 0 \quad (1.3)$$

Equations 1.2 and 1.3 are just Maxwell's equations. The equilibrium state itself is described by Equation 1.1, which states that the force due to the gradient of the plasma pressure is balanced by the magnetic force acting on the plasma.

The simplest general example of the force balance equation arises by considering a simple screw pinch. This system consists of a cylindrical plasma with both angular and axial components of \mathbf{J} and \mathbf{B} , as shown in Figure 1-1. The resulting magnetic field vector is helical, similar to the threads on a screw. Allowing the field and current density to vary only in the radial direction ensures that Equation 1.3 is satisfied:

$$\frac{1}{r} \frac{\partial B_\theta(r)}{\partial \theta} + \frac{\partial B_z(r)}{\partial z} = 0 \quad (1.4)$$

Combining Equations 1.1 and 1.2 leads to the pressure balance equation for this system, namely:

$$\frac{d}{dr} \left(p + \frac{B_\theta^2 + B_z^2}{2\mu_0} \right) + \frac{B_\theta^2}{\mu_0 r} = 0 \quad (1.5)$$

Examining Equation 1.5 shows that knowledge of the profiles of the plasma pressure and one of the magnetic field components makes it possible to determine the profile of the other magnetic field component. Assuming that the axial component of the field is known, the azimuthal component can be determined from

$$r \frac{d}{dr} \left(\frac{B_\theta^2}{2\mu_0} \right) + \frac{B_\theta^2}{\mu_0} = -r \frac{dp}{dr} - r \frac{d}{dr} \left(\frac{B_z^2}{2\mu_0} \right) \quad (1.6)$$

To find this component of the field exactly, though, requires knowledge of the boundary conditions.

In general, the plasma is supported in equilibrium by an externally applied magnetic field. This field is generated by a set of current carrying conductors surrounding the plasma. Furthermore, a vacuum region is assumed to exist between the plasma and the conductors. From this, it is possible to define the plasma surface (which in general is non-circular) as the curve along which the plasma pressure is effectively zero.

The boundary conditions at the plasma surface are given by

$$\hat{n} \cdot \mathbf{B} |_a = \hat{n} \cdot \hat{\mathbf{B}} |_a \quad (1.7)$$

$$\hat{n} \times \mathbf{B} |_a = \hat{n} \times \hat{\mathbf{B}} |_a \quad (1.8)$$

$$B^2 |_a = \hat{B}^2 |_a \quad (1.9)$$

where \mathbf{B} is the magnetic field within the plasma, $\hat{\mathbf{B}}$ is the vacuum magnetic field, and \hat{n} is the outward pointing unit vector normal to the plasma surface. These boundary conditions ensure that the normal and tangential components of the magnetic field and the magnetic pressure are continuous across the plasma surface and it is assumed that no surface currents flow. Additionally, the condition $\mathbf{B} \cdot \nabla p = 0$ implies that $\mathbf{n} \cdot \mathbf{B} |_a = 0$, which simplifies Equation 1.7 to

$$\hat{n} \cdot \hat{\mathbf{B}} |_a = 0 \quad (1.10)$$

The vacuum field $\hat{\mathbf{B}}$ is determined from

$$\hat{\mathbf{B}} = \mathbf{B}_a + \tilde{\mathbf{B}} \quad (1.11)$$

where \mathbf{B}_a is the magnetic field due to the conductors and $\tilde{\mathbf{B}}$ is the vacuum magnetic field of the plasma.

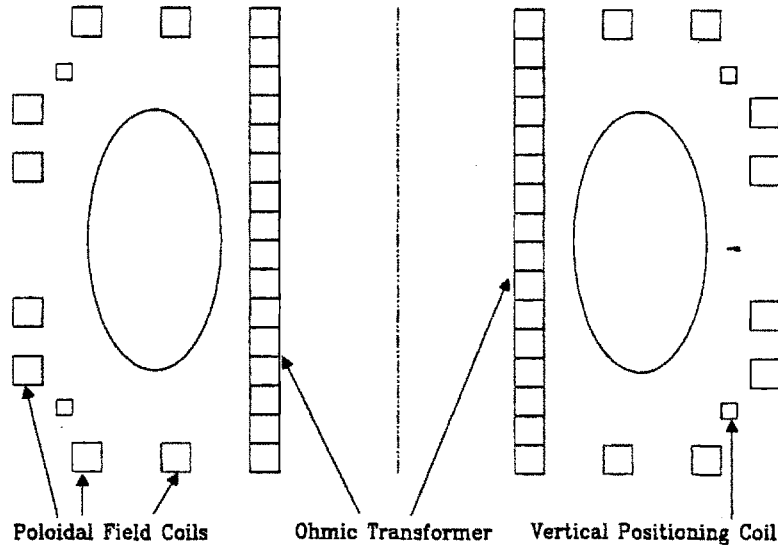


Figure 1-2: Geometry and coils of an ohmically heated tokamak.

Extending the MHD equations to the toroidally axisymmetric geometry of a tokamak results in the Grad-Shafranov equation, given by

$$\Delta^* \psi = -\mu_0 R^2 \frac{dp}{d\psi} - F \frac{dF}{d\psi} \quad (1.12)$$

where ψ is a stream function for the poloidal magnetic field, Δ^* is an elliptic operator given by

$$\Delta^* = R \frac{\partial}{\partial R} \left(\frac{1}{R} \frac{\partial}{\partial R} \right) + \frac{\partial^2}{\partial Z^2} \quad (1.13)$$

p is the plasma pressure, and F is a function related to the net poloidal current. All of the equilibria presented in this thesis were produced by a system which generates an approximate solution to the Grad-Shafranov equation.

1.2 The Poloidal Field System

Figure 1-2 shows the general geometry of an ohmically heated tokamak and the major components of the poloidal field coil system. The first major component is the ohmic transformer. This set of

coils acts as the primary winding of a large transformer, with the plasma acting as the secondary. The current in the plasma is induced by varying the current in the ohmic coils.

The second system is made up of the poloidal field coils themselves. These coils are responsible for shaping the plasma and providing the radial and toroidal pressure balance needed to maintain the plasma in equilibrium.

The third system is a set of feedback controlled vertical positioning coils. These coils are necessary to stabilize the vertical instability associated with highly elongated equilibria. As the plasma drifts in the vertical direction, current is applied to these coils in order to push the plasma back to the midplane of the machine.

1.3 Estimating PF Coil Currents

Equations 1.8 and 1.10 describe the boundary conditions which the equilibrium must satisfy. The equilibrium information provided by the Grad-Shafranov equation provides the poloidal magnetic field at the plasma surface. Combining this information makes it possible to determine the required currents in the external coils. Chapter 2 reviews a method for quickly estimating these currents. This method is based on an application of the scalar version of Green's theorem to compute the tangential component of the vacuum magnetic field at the surface of the plasma. This quantity is expressed in the form

$$\hat{B}_p(\mu) = b^{(1)}(\mu) + \sum_{j=1}^J b_j^{(2)}(\mu) I_j \quad (1.14)$$

where μ is a poloidal angular variable, I_j is the unknown current in the j th poloidal field coil, and the terms $b^{(1)}(\mu)$ and $b_j^{(2)}(\mu)$ are determined by requiring that $\mathbf{n} \cdot \hat{\mathbf{B}} = 0$ on the plasma surface for any arbitrary set of I_j .

The currents are determined by minimizing a functional of the form

$$\epsilon_I = \frac{\int_{S_p} (\hat{B}_p - B_p)^2 dS}{\int_{S_p} B_p^2 dS} \quad (1.15)$$

where B_p is the tangential component of the poloidal field just inside the plasma surface. Minimizing this functional form ensures that the discontinuity in the tangential component of the magnetic field is as small as possible.

It can be shown that the set of currents that minimize ϵ_I satisfy a simple set of linear equations. The currents can, therefore, be found without the need of a potentially fragile and

time consuming iteration process. As a result, this procedure – implemented in a program called cPFC – is extremely fast and robust.

1.4 Extension to Asymmetric Systems

As implemented in the original version of the cPFC program, the method for estimating the coil currents described in the previous section was only applicable to up-down symmetric systems. These systems have both equilibria and poloidal field coil sets which are perfectly symmetric about the midplane of a tokamak. Requiring the system to be symmetric limited the applicability of the cPFC program.

Chapter 3 describes the changes made to cPFC to facilitate its use on asymmetric systems. Such systems include systems with asymmetries in the coil set due to engineering considerations, asymmetric field structures due to the presence of vertical positioning coils, or asymmetric plasmas such as those found in single-null diverted tokamaks.

1.5 Current Constraints

Chapter 4 describes a method for estimating the poloidal field coil currents in light of constraints on those currents. These constraints can arise in several ways. First, the power supply generating the current in a given coil may simply limit the maximum current that coil can carry. Second, the current in a resistive coil may generate so much heat in the coil that the maximum temperature allowed in the coil is exceeded. If this maximum temperature corresponds to the melting point of the coil material, the coil could fail – a situation which should clearly be avoided if possible. Finally, if the coil is superconducting, the maximum current allowed in the coil is simply the critical current of the coil material.

1.6 Force Constraints

The poloidal field coils all experience a force proportional to $\mathbf{J} \times \mathbf{B}$, where \mathbf{J} is the current density in the coil and \mathbf{B} is the total magnetic field sampled by the coil. The coils and their support structure must be capable of withstanding these forces, or else they will fail. The equations needed to compute the forces on the coils are derived in Chapter 5. With these expressions for

the forces, it is possible to apply the method developed in Chapter 4 for simple current constraints to the force constraint problem, which is the subject of Chapter 6.

Chapter 2

Review of Coil Current Solver

The basic foundation for the thesis is the analysis carried out by Haney [12]. In this chapter, his work on finding the poloidal field coil currents is reviewed and summarized. For purposes of clarity, some of the notation has been changed and elaborations have been made to some derivations wherever appropriate. It should also be noted that only information relevant to the current work has been included. For specific details the reader is referred to [12].

2.1 Introduction

Exact computation of the poloidal field coil currents requires the self-consistent solution of Maxwell's equations for the magnetic fields in the plasma and the vacuum regions of a tokamak. The plasma field can be obtained by solving the Grad-Shafranov equation, and the vacuum field can be computed from Laplace's equation. Boundary conditions imposed at the plasma surface connect the two solutions. The assumption that the plasma current and pressure vanish smoothly at the plasma surface dictates that the poloidal magnetic field be continuous across the plasma surface.

Generally, it is not possible to find a finite set of currents that satisfy the governing equations and the boundary conditions when both the plasma surface and the conductor locations are fixed. This is because a finite set of conductor currents is not capable of exactly satisfying the boundary conditions at an infinite number of points along the plasma surface. To compute the exact solution, the plasma surface is allowed to vary with the conductor currents. Since the plasma surface can move, this is referred to as the "free boundary" equilibrium problem.

The free boundary method makes it possible to determine the plasma and vacuum magnetic

fields exactly and self-consistently. The disadvantage is that this method represents a difficult and time-consuming numerical computation. Another possible method involves the sacrifice of some accuracy by maintaining a fixed plasma surface. This assumption makes it impossible to match the boundary conditions exactly – there will be some jump in the magnetic field at the plasma surface. However, for any given set of conductors, there will in general be some set of currents which *minimizes* the jump in the field.

The remainder of this chapter describes a method for determining the poloidal field coil currents in the above manner. Much of this procedure consists of the computation of the vacuum field at the plasma surface. This is accomplished by using Green's theorem to derive an integral equation for the scalar magnetic potential at the plasma surface. By Fourier analyzing this integral equation, an equivalent linear system is found which can be solved by standard techniques. The scalar magnetic potential can then be used to represent the vacuum magnetic field in terms of the unknown conductor currents. The conductor currents are then found by minimizing the root-mean-square jump in the field across the plasma surface.

2.2 Problem Statement

The first step in determining the conductor currents involves stating the problem in precise mathematical terms. Figure 2-1 shows the surface of a toroidally axisymmetric plasma. The plasma surface is characterized by

$$R = R_p(\mu) \quad (2.1)$$

$$Z = Z_p(\mu) \quad (2.2)$$

where μ is an arbitrary angular coordinate.

With this parameterization of the plasma surface, it is possible to define a number of quantities, including the unit normal vector,

$$\mathbf{e}_n = \frac{1}{Q} [Z_\mu \mathbf{e}_R - R_\mu \mathbf{e}_Z] \quad (2.3)$$

and the unit tangent vector,

$$\mathbf{e}_t = \frac{1}{Q} [R_\mu \mathbf{e}_R + Z_\mu \mathbf{e}_Z] \quad (2.4)$$

where \mathbf{e}_R and \mathbf{e}_Z are the unit vectors in the R and Z coordinate directions respectively, and

$$Q \equiv [R_\mu^2 + Z_\mu^2]^{1/2} \quad (2.5)$$

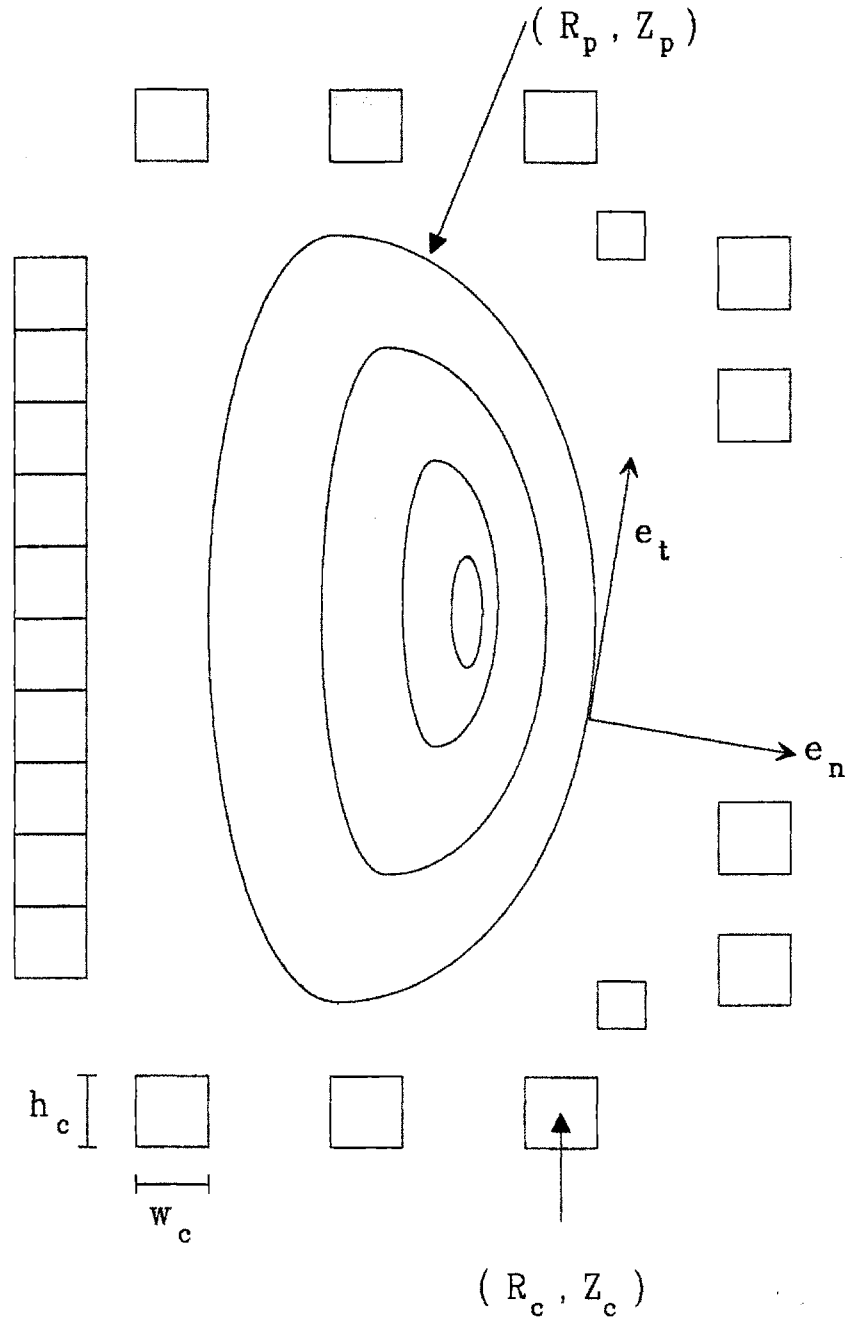


Figure 2-1: Geometry of the plasma surface and conductors for use in the poloidal field coil current calculation

From the definitions of the unit vectors, it is possible to define the normal and tangential derivatives with respect to the plasma surface. The normal derivative is given by

$$Q \mathbf{e}_n \cdot \nabla \equiv \frac{\partial}{\partial n} = Z_\mu \frac{\partial}{\partial R} - R_\mu \frac{\partial}{\partial Z} \quad (2.6)$$

and the tangential derivative by

$$Q \mathbf{e}_t \cdot \nabla \equiv \frac{\partial}{\partial \mu} = R_\mu \frac{\partial}{\partial R} + Z_\mu \frac{\partial}{\partial Z} \quad (2.7)$$

The differential element of arc length is computed from

$$ds^2 = dR_p^2 + dZ_p^2 = R_\mu^2 d\mu + Z_\mu^2 d\mu = Q^2 d\mu^2 \quad (2.8)$$

and the differential surface area is

$$dS = R ds d\phi = R Q d\mu d\phi \quad (2.9)$$

The plasma depicted in Figure 2-1 is assumed to be surrounded by vacuum. Within this vacuum region there are a total of J toroidally axisymmetric conductors. The position of each conductor is given by (R_j, Z_j) . These conductors are treated as filaments to simplify the calculation of the coil currents, but in order to compute the resistance of the coil, each conductor is assumed to have a rectangular cross-section with a width w_j and height h_j . The goal of the analysis, then, is to determine the current I_j flowing in each conductor.

Calculation of the coil currents requires knowledge of the plasma and vacuum magnetic fields at the plasma surface. For the purpose of this derivation, the tangential field at the plasma surface due to the plasma is assumed known from the solution to the Grad-Shafranov equation. The magnetic field in the vacuum region (\mathbf{B}_v) can then be written as the sum of the plasma field (\mathbf{B}_p) and the field due to the external coils (\mathbf{B}_c):

$$\mathbf{B}_v = \mathbf{B}_p + \mathbf{B}_c \quad (2.10)$$

Within the vacuum region, the field due to the plasma satisfies

$$\nabla \cdot \mathbf{B}_p = 0 \quad (2.11)$$

$$\nabla \times \mathbf{B}_p = 0 \quad (2.12)$$

and is required to remain regular everywhere. It is then possible to express \mathbf{B}_p as

$$\mathbf{B}_p = \nabla \phi + \mathbf{B}_i \quad (2.13)$$

where ϕ is the scalar magnetic potential and \mathbf{B}_i is the field due to a single filament assumed to carry all of the plasma current and located at the plasma magnetic axis (R_m, Z_m) . The exact location of this filament is not critical and does not affect the results. From equation 2.11 the scalar potential satisfies Laplace's equation

$$\nabla^2 \phi = 0 \quad (2.14)$$

The filamentary plasma field \mathbf{B}_i has been introduced into this formulation to guarantee that ϕ is single-valued. This is necessary to ensure that the application of Ampere's law to the plasma boundary yields the correct value of the plasma current.

From magnetostatics, the \mathbf{B}_i field can be expressed as

$$\mathbf{B}_i = \mu_0 I_p \frac{\nabla \Psi_p \times \mathbf{e}_\phi}{R} \quad (2.15)$$

where

$$\Psi_p = \frac{(RR_m)^{1/2}}{2\pi} \left[\frac{(2 - k_p^2)K(k_p) - 2E(k_p)}{k_p} \right] \quad (2.16)$$

K and E are the complete elliptic integrals of the first and second kind, respectively, and

$$k_p^2 = \frac{4RR_m}{(R + R_m)^2 + (Z - Z_m)^2} \quad (2.17)$$

The J conductors are assumed to be small in cross-section and far from the plasma surface (relative to the dimensions of the conductor). This makes it possible to compute the applied field \mathbf{B}_c in a manner similar to \mathbf{B}_i :

$$\mathbf{B}_c = \sum_{j=1}^J \mu_0 I_j \frac{\nabla \Psi_j \times \mathbf{e}_\phi}{R} \quad (2.18)$$

where

$$\Psi_j = \frac{(RR_j)^{1/2}}{2\pi} \left[\frac{(2 - k_j^2)K(k_j) - 2E(k_j)}{k_j} \right] \quad (2.19)$$

and

$$k_j^2 = \frac{4RR_j}{(R + R_j)^2 + (Z - Z_j)^2} \quad (2.20)$$

One property of the ideal MHD model is that the plasma is perfectly conducting. This requires that the component of the magnetic field normal to the plasma surface vanish within and just outside of the plasma surface:

$$\mathbf{e}_n \cdot \mathbf{B}_i |_{S_p} = \mathbf{e}_n \cdot \mathbf{B}_v |_{S_p} = 0 \quad (2.21)$$

where B_i is the plasma field inside the plasma. The solution of the Grad-Shafranov equation for the plasma equilibrium already satisfy this condition. For the vacuum field, however, it is necessary to apply Equation 2.21 explicitly. In the following section, it is shown that this condition allows the tangential component of the vacuum field to be expressed in the form

$$B_v(\mu) = b^{(1)}(\mu) + \mathbf{b}^{(2)}(\mu) \cdot \mathbf{i} \quad (2.22)$$

where \mathbf{i} and $\mathbf{b}^{(2)}$ are column vectors of length J containing the currents I_j and a set of geometric coefficients $b_j^{(2)}$ respectively. The currents I_j are then determined by minimizing the functional

$$\epsilon_I(\mathbf{i}) = \frac{\int_{S_p} (B_p - B_v)^2 dS}{\int_{S_p} B_p^2 dS} \quad (2.23)$$

where B_p and B_v represent the tangential components of the plasma and vacuum fields, respectively. Equation 2.23 can be thought of as the net deviation from exact radial pressure balance. Minimization of ϵ_I is thus equivalent to minimizing the net deviation from exact radial pressure balance at the plasma boundary.

2.3 Calculation of the Vacuum Field

The method used to determine the vacuum field B_v is based on an application of Green's theorem [20]. This choice is facilitated by the fact that the field must only be calculated on the plasma surface. Additionally, several analyses have shown that this formalism is well suited for fast numerical computation [7,5,6,11].

Green's theorem for the scalar magnetic potential is written as

$$\sigma \phi(\mathbf{r}) + \int_{S_p} \left[\phi(\mathbf{r}') (\mathbf{e}'_n \cdot \nabla' \hat{G}(\mathbf{r}, \mathbf{r}')) - \hat{G}(\mathbf{r}, \mathbf{r}') (\mathbf{e}'_n \cdot \nabla' \phi(\mathbf{r}')) \right] dS' = 0 \quad (2.24)$$

In this equation, $\mathbf{r}' \equiv (R', \varphi', Z')$ and $\mathbf{r} \equiv (R, \varphi, Z)$. Additionally, \mathbf{r} denotes the observation point and \mathbf{r}' represents the variables of integration. Also, a regularity condition is imposed on ϕ so that the integral over an infinite bounding surface (S_∞) vanishes.

As discussed earlier, the plasma surface coordinates are parameterized with respect to μ , so that $R' = R_p(\mu')$ and $Z' = Z_p(\mu')$. The function \hat{G} is the infinite space Green's function given by

$$\hat{G}(\mathbf{r}, \mathbf{r}') = -\frac{1}{4\pi |\mathbf{r}' - \mathbf{r}|} \quad (2.25)$$

where

$$|\mathbf{r}' - \mathbf{r}| = \left[R^2 + R'^2 - 2RR' \cos(\varphi' - \varphi) + (Z' - Z)^2 \right]^{1/2} \quad (2.26)$$

Finally, σ is a coefficient which depends on the location of the observation point relative to the plasma surface, and is given by

$$\sigma = \begin{cases} 1 & \text{if } \mathbf{r} \text{ is outside the plasma,} \\ \frac{1}{2} & \text{if } \mathbf{r} \text{ is on the plasma surface,} \\ 0 & \text{if } \mathbf{r} \text{ is inside the plasma.} \end{cases} \quad (2.27)$$

Since the goal of this analysis is to compute ϕ on the plasma surface, σ is taken to be $1/2$, and R and Z are set to $R_p(\mu)$ and $Z_p(\mu)$, respectively.

2.3.1 Simplification of Green's Theorem

Through the assumption of toroidal axisymmetry, it is possible to eliminate the φ dependence in the integral of equation 2.24. This reduces equation 2.24 to

$$\frac{1}{2}\phi(\mu) + \int_0^{2\pi} \left[\phi(\mu') \frac{\partial G(\mu, \mu')}{\partial n'} - G(\mu, \mu') \frac{\partial \phi(\mu')}{\partial n'} \right] R' d\mu' = 0 \quad (2.28)$$

where G is the reduced Green's function defined as

$$G = \int_0^{2\pi} \hat{G} d\varphi' \quad (2.29)$$

Integrating equation 2.29 gives

$$G = -\frac{kK(k)}{2\pi\sqrt{RR'}} \quad (2.30)$$

where k is given by

$$k^2 = \frac{4RR'}{(R' + R)^2 + (Z' - Z)^2} \quad (2.31)$$

The solution of equation 2.28 requires the evaluation of the normal derivatives of G and ϕ . Using the definition of the normal derivative (equation 2.6) and the identities [10]

$$\frac{dE(k)}{dk} = \frac{1}{k} [E(k) - K(k)] \quad (2.32)$$

$$\frac{dK(k)}{dk} = \frac{1}{k} \left[\frac{E(k)}{1 - k^2} - K(k) \right] \quad (2.33)$$

results in

$$R' \frac{\partial G}{\partial n'} = \frac{1}{2\pi} \left(\frac{R'}{R} \right)^{1/2} [\Lambda k E(k) + \Gamma k (K(k) - E(k))] \quad (2.34)$$

where

$$\Lambda = \frac{Z'_\mu(R' - R) - R'_\mu(Z' - Z)}{(R' - R)^2 + (Z' - Z)^2} \quad (2.35)$$

$$\Gamma = \frac{Z'_\mu}{2R'} \quad (2.36)$$

The normal derivative of ϕ can be found by invoking the boundary condition on \mathbf{B}_v , namely

$$R' \frac{\partial \phi}{\partial n'} = \frac{\partial}{\partial \mu'} \left(\mu_0 I_p \Psi_p + \sum_{j=1}^J \mu_0 I_j \Psi_j \right) \quad (2.37)$$

Since no assumptions have been made about either the plasma shape or the location of the various conductors, equation 2.37 shows that it is always possible to make the normal component of the vacuum field exactly vanish at the plasma surface.

2.3.2 Conductor Grouping

For a given PF system, it often occurs that several conductors are constrained to carry the same current, while others carry a fixed current dictated by external conditions. Thus, the number of unique currents that must be determined is often much less than J . Incorporating these cases now may save a significant amount of computation.

Generally, conductors can be constrained to carry the same current for a number of reasons. One such reason is conductor geometry. In general, several filaments are used to model the windings of a finite sized coil. These conductors are linked in series electrically, causing them to carry the same current. Another reason is symmetry. Often, the conductors are located symmetrically with respect to the midplane of the machine ($Z = 0$). This case usually occurs for up-down symmetric plasmas. Finally, it may be the case that there are too few power supplies to drive each coil independently, so some coils must be grouped together.

Fixed conductor currents can also occur for a number reasons. One example of this is the flat-top portion of an ohmically heated discharge. In this phase of operation, the current in the ohmic transformer is preprogrammed to generate a constant plasma current. Calculation of the poloidal field system currents at a given time requires taking a "snapshot" of the equilibrium and computing the coil currents while the ohmic stack current is held constant at its preprogrammed value.

Accounting for grouped and fixed currents is straightforward. It is assumed that the currents in F of the conductors are fixed. The remaining conductors are assumed to belong to one of G

groups, where each conductor in each group is constrained to carry the same current I_g . The G currents are then computed using the technique described in the next section.

From the above discussion, the vacuum field due to the conductors (B_c) can be expressed as

$$\mathbf{B}_c = \mu_0 I_p \frac{\nabla \Psi_F \times \mathbf{e}_\phi}{R} + \sum_{g=1}^G \mu_0 I_g \frac{\nabla \Psi_g \times \mathbf{e}_\phi}{R} \quad (2.38)$$

where

$$\Psi_F = \sum_{j=1}^J \frac{I_j}{I_p} \delta_j^{(F)} \Psi_j \quad (2.39)$$

and

$$\Psi_g = \sum_{j=1}^J \delta_j^{(g)} \Psi_j \quad (2.40)$$

Here, Ψ_F accounts for the poloidal flux from the conductors carrying fixed currents, while Ψ_g represents the total poloidal flux from the g -th conductor group. The selection functions $\delta_j^{(F)}$ and $\delta_j^{(g)}$ are defined by

$$\delta_j^{(F)} = \begin{cases} 1 & \text{if } I_j \text{ is a fixed current,} \\ 0 & \text{otherwise.} \end{cases} \quad (2.41)$$

$$\delta_j^{(g)} = \begin{cases} 1 & \text{if conductor } j \text{ is in group } g, \\ 0 & \text{otherwise.} \end{cases} \quad (2.42)$$

Utilizing these results to rewrite equation 2.37 gives

$$R' \frac{\partial \phi}{\partial n'} = \frac{\partial}{\partial \mu'} \left(\mu_0 I_p \Psi_p + \mu_0 I_p \Psi_F + \sum_{g=1}^G \mu_0 I_g \Psi_g \right) \quad (2.43)$$

In the right hand side of this expression, only the quantities I_g , where $1 \leq g \leq G$ are unknown.

2.3.3 Fourier Analysis

Equation 2.28 can be solved through standard Fourier analysis techniques. This is done by first expanding ϕ and its normal derivative in Fourier series:

$$\phi = \sum_{m=-M}^M a_m e^{im\mu} \quad (2.44)$$

$$R \frac{\partial \phi}{\partial n} = \sum_{m=-M}^M \left(c_m + \sum_{g=1}^G D_{mg} I_g \right) e^{im\mu} \quad (2.45)$$

where, in principle, the summation over m should range from $-\infty$ to $+\infty$. Practical considerations, however, require that the Fourier series be truncated after a finite number of terms given by $m = \pm M$.

The coefficients c_m and D_{mg} are assumed known. They can be calculated from the Fourier transform of equation 2.43, and are given by

$$c_m = \frac{im}{2\pi} \int_0^{2\pi} (\mu_0 I_p \Psi_p + \mu_0 I_p \Psi_F) e^{-im\mu} d\mu \quad (2.46)$$

$$D_{mg} = \frac{im}{2\pi} \int_0^{2\pi} \mu_0 \Psi_g e^{-im\mu} d\mu \quad (2.47)$$

The goals of this analysis are to first find the coefficients a_m and then the values of the I_g by minimizing ϵ_I . The a_m are determined by using the expansions given by equations 2.44 and 2.45. These expansions are substituted into equation 2.28, which is then multiplied by $e^{-im'\mu}$ and integrated over μ . The end result of this process is

$$\begin{aligned} a_m + \frac{a_m}{\pi} \sum_{m'=-M}^M \int_0^{2\pi} \int_0^{2\pi} R' \frac{\partial G(\mu, \mu')}{\partial n'} e^{im'\mu' - im\mu} d\mu d\mu' \\ = \left(c_m + \sum_{g=1}^G D_{mg} I_g \right) \sum_{m'=-M}^M \frac{1}{\pi} \int_0^{2\pi} \int_0^{2\pi} G(\mu, \mu') e^{im'\mu' - im\mu} d\mu d\mu' \end{aligned} \quad (2.48)$$

The integrands on the left and right sides of this equation can be expressed as

$$A_{mm'} = \frac{1}{\pi} \int_0^{2\pi} \int_0^{2\pi} R' \frac{\partial G(\mu, \mu')}{\partial n'} e^{im'\mu' - im\mu} d\mu d\mu' \quad (2.49)$$

$$C_{mm'} = \frac{1}{\pi} \int_0^{2\pi} \int_0^{2\pi} G(\mu, \mu') e^{im'\mu' - im\mu} d\mu d\mu' \quad (2.50)$$

where A and C have dimension $(2M+1) \times (2M+1)$. With these definitions, equation 2.48 can be expressed in a linear algebraic form:

$$[\mathbf{I} + \mathbf{A}] \cdot \mathbf{a} = \mathbf{C} \cdot [\mathbf{c} + \mathbf{D} \cdot \mathbf{i}] \quad (2.51)$$

where \mathbf{I} is the identity matrix and \mathbf{i} is a vector of length G containing the values of the grouped currents I_g . The solution to this equation is

$$\mathbf{a} = \mathbf{d} + \mathbf{E} \cdot \mathbf{i} \quad (2.52)$$

where

$$\mathbf{d} = [\mathbf{I} + \mathbf{A}]^{-1} \cdot \mathbf{C} \cdot \mathbf{c} \quad (2.53)$$

$$\mathbf{E} = [\mathbf{I} + \mathbf{A}]^{-1} \cdot \mathbf{C} \cdot \mathbf{D} \quad (2.54)$$

Note that the elements d_m and $E_{mm'}$ are known quantities depending only upon the coil locations, the plasma shape, and the known fixed currents.

Equation 2.52 can then be substituted into equation 2.13 to express the tangential component of the vacuum field as

$$B_v = b^{(F)}(\mu) + b^{(G)}(\mu) \cdot \mathbf{i} \quad (2.55)$$

where $b^{(F)}(\mu)$ represents the tangential field (at the plasma surface) due to those conductors carrying fixed currents and $b^{(G)}(\mu)$ is the tangential field from the grouped conductors. Written in terms of 2.53 and 2.54, these fields are

$$b^{(F)}(\mu) = \frac{1}{Q} \left(\sum_{m=-M}^M (im d_m e^{im\mu}) + \mu_0 \frac{I_p}{R} \frac{\partial \Psi_p}{\partial n} + \mu_0 \frac{I_p}{R} \frac{\partial \Psi_F}{\partial n} \right) \quad (2.56)$$

$$b_g^{(G)}(\mu) = \frac{1}{Q} \left(\sum_{m=-M}^M (im E_{mg} e^{im\mu}) + \mu_0 \frac{1}{R} \frac{\partial \Psi_g}{\partial n} \right) \quad (2.57)$$

2.4 Solution for Group Currents

Recall that the ultimate goal of this analysis is to find the conductor currents I_j in such a way as to minimize the jump in the tangential field across the plasma surface. From equation 2.23 this jump is written as

$$\epsilon_I(\mathbf{i}) = \frac{\int_{S_p} (B_p - B_v)^2 dS}{\int_{S_p} B_p^2 dS}$$

Substituting equations 2.56 and 2.57 into this expression casts the expression for ϵ_I into a simpler form:

$$\epsilon_I(\mathbf{i}) = \mathbf{i} \cdot \mathbf{M} \cdot \mathbf{i} - 2\mathbf{n} \cdot \mathbf{i} + p \quad (2.58)$$

where \mathbf{i} is a vector of length G representing the group currents being solved for, \mathbf{M} is a $(G \times G)$ symmetric matrix, \mathbf{n} is a vector of length G , and p is a scalar. The quantities \mathbf{M} , \mathbf{n} , and p are, in turn, defined as

$$M_{gg'} = \frac{\int_0^{2\pi} RQ b_g^{(G)} b_{g'}^{(G)} d\mu}{\int_0^{2\pi} RQ B_p^2 d\mu} \quad (2.59)$$

$$n_g = \frac{\int_0^{2\pi} RQ b_g^{(G)} (B_p - b^{(F)}) d\mu}{\int_0^{2\pi} RQ B_p^2 d\mu} \quad (2.60)$$

$$p = \frac{\int_0^{2\pi} RQ (B_p - b^{(F)})^2 d\mu}{\int_0^{2\pi} RQ B_p^2 d\mu} \quad (2.61)$$

The tangential field error given by equation 2.58 can now be minimized with respect to the group currents. This is done by formally computing the derivative of ϵ_I and setting it to zero:

$$\frac{\partial \epsilon_I}{\partial I_g} = 0; \quad g = 1, \dots, G \quad (2.62)$$

Applying equation 2.62 to equation 2.58 results in a simple linear system given by

$$\mathbf{M} \cdot \mathbf{i} = \mathbf{n} \quad (2.63)$$

This system can be solved through standard matrix techniques [22]. In typical tokamak configurations, G ranges from 4 to 10, so equation 2.63 presents a trivial computational task for current computer systems. Finally, it should be observed that the entire calculation is carried out without iteration or searching, implying that this technique will be extremely fast and robust.

Once the vector \mathbf{i} is found, it can be substituted into Equation 2.58 to compute the value of ϵ_I . This value of ϵ_I represents an absolute estimate of the error in the radial pressure balance from using this set of coil currents to support the given equilibrium.

2.5 Summary

Although the calculations described in this chapter are fairly complex, they can be summarized in a relatively simple manner. The solution procedure assumes that the following information is known:

- Equilibrium information:
 1. The plasma shape.
 2. The total plasma current.
 3. The tangential component of the plasma magnetic field at the plasma surface, denoted B_p .
- Conductor information:
 1. The locations (R, Z) of the J conductors surrounding the plasma.
 2. The currents in F of the J conductors (i.e., the conductors carrying fixed pre-programmed currents)

3. The grouping of the conductors carrying the same current (i.e., the multifilament model of a finite size coil).

These quantities are the inputs to the solution procedure. The output consists of the ϵ_I minimizing values of the G group conductor currents. These group currents are calculated as follows. First, the plasma shape information is used to compute the matrices A and C in equations 2.49 and 2.50. The plasma shape information is combined with the conductor information to compute the c vector and the D matrix in equations 2.46 and 2.47. These matrices are then used to compute the vacuum field surrounding the plasma, B_v . Substituting B_v and the plasma equilibrium field B_p into equations 2.59 – 2.61 gives M and n . The group currents i are then found by solving equation 2.63.

Chapter 3

Asymmetric Systems

The model developed in Chapter 2 was implemented by Haney in a program called cPFC. This software takes the data about a given equilibrium and generates a set of poloidal field coil currents which support that equilibrium. Haney's version of the program, however, is applicable only to equilibria and coil sets which are up-down symmetric. Thus, the results produced are not applicable to coil sets with asymmetries, single-null diverted equilibria, or systems with current applied to the vertical positioning coils. In this chapter, the original version of the software is extended to include general asymmetric cases.

3.1 Discussion

In Chapter 2, the theory behind the original coil current solver was presented. Other than the toroidal axisymmetry requirement, that derivation made no assumptions about plasma or conductor symmetries. In particular, all of the Fourier transforms used to determine the coil currents were expressed in complex form, thereby allowing any plasma-coil configuration to be solved.

To simplify the implementation of this scheme, it was assumed that both the plasma and the coils were symmetric in e_z . An example of such a system is shown in Figure 3-1, and the corresponding tangential component of the poloidal field is shown in Figure 3-2. Note that the poloidal field is symmetric about $\mu = \pi$.

By assuming that the plasma and coil set were symmetric, it was only necessary to work with the real components of the various Fourier series and transforms presented in Chapter 2. For

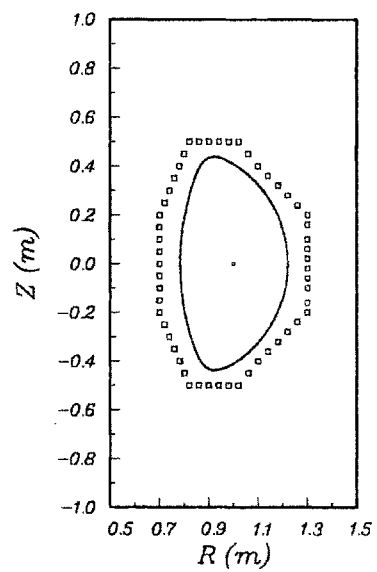


Figure 3-1: Example of a symmetric plasma and coil set

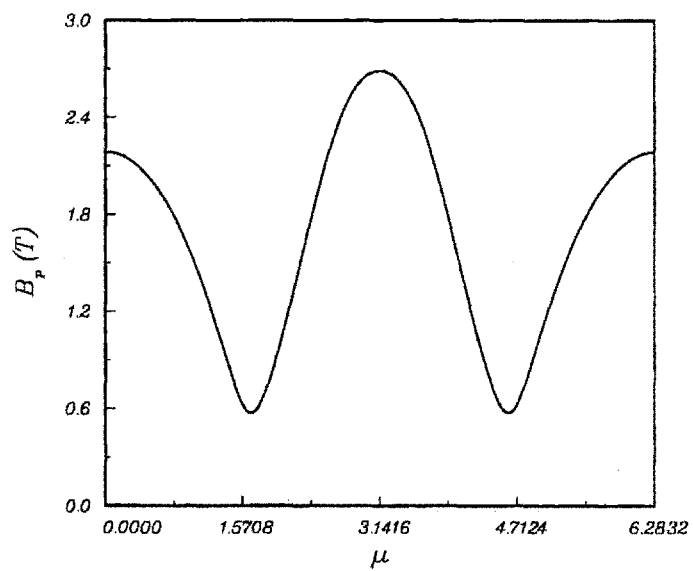


Figure 3-2: Tangential poloidal field for the equilibrium presented in Figure 3-1

example, in expressing the scalar magnetic potential as a Fourier series, Equation 2.44

$$\phi(\mu) = \sum_{m=-M}^M a_m e^{im\mu}$$

was programmed in the form

$$\phi(\mu) = \sum_{m=-M}^M a_m \cos(m\mu) \quad (3.1)$$

where the a_m were assumed to be purely real. The other arrays and vectors used to compute the scalar potential were treated in a similar manner. Such treatment is warranted since the Fourier transform of a symmetric (i.e. even) function contains only real components [18].

3.2 Generalization

Consider now the single null diverted plasma shown in Figure 3-3. The poloidal field due to this plasma is shown in Figure 3-4. As this last figure clearly shows, the poloidal field is no longer symmetric about $\mu = \pi$, making it impossible to find a set of coil currents to support that equilibrium using the original (symmetric) version of cPFC.

Generalizing cPFC to the asymmetric case proved fairly straightforward. First, all of the real vectors and matrices used to compute the scalar potential and its normal derivative on the plasma surface were converted to complex form. Then, a suitable matrix inversion routine was applied to determine \mathbf{d} and \mathbf{E} , which in turn were used to compute \mathbf{a} . Finally, the equations for the fixed and grouped components of the vacuum field were explicitly written in the form

$$b^{(F)}(\mu) = \frac{1}{Q} \left(\sum_{m=-M}^M \Re(imd_m e^{im\mu}) + \mu_0 \frac{I_p}{R} \frac{\partial \Psi_p}{\partial n} + \mu_0 \frac{I_p}{R} \frac{\partial \Psi_F}{\partial n} \right) \quad (3.2)$$

$$b_g^{(G)}(\mu) = \frac{1}{Q} \left(\sum_{m=-M}^M \Re(imE_{mg} e^{im\mu}) + \mu_0 \frac{1}{R} \frac{\partial \Psi_g}{\partial n} \right) \quad (3.3)$$

where \Re is the real operator.

Since the magnetic field is purely real, one test of the accuracy of this transformation is to compute the quantities

$$Ib^{(F)}(\mu) = \frac{1}{Q} \sum_{m=-M}^M \Im(imd_m e^{im\mu}) \quad (3.4)$$

$$Ib_g^{(G)}(\mu) = \frac{1}{Q} \sum_{m=-M}^M \Im(imE_{mg} e^{im\mu}) \quad (3.5)$$

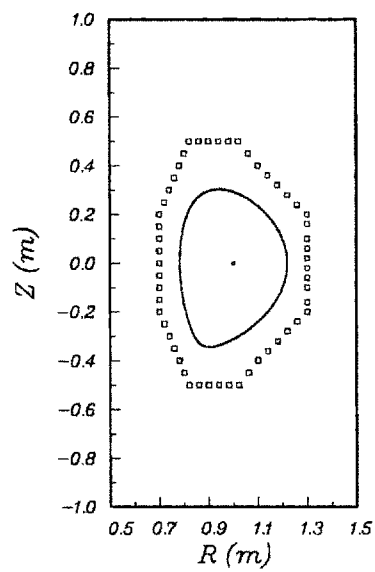


Figure 3-3: Example of a single null diverted plasma

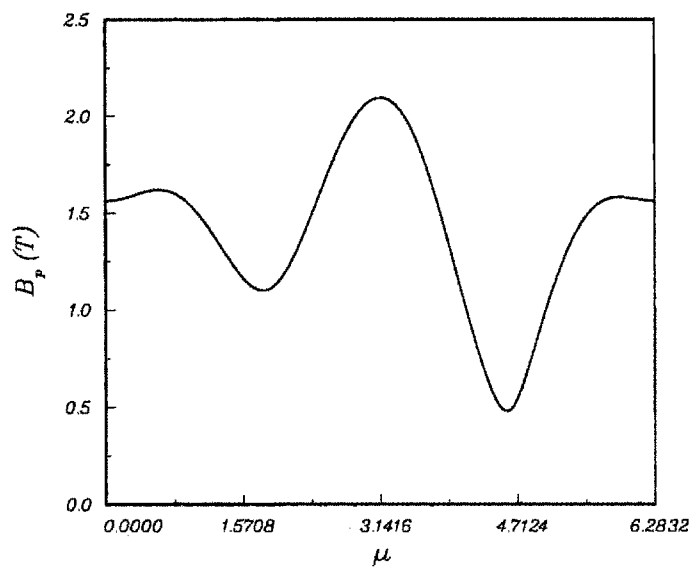


Figure 3-4: Tangential poloidal field of the single null plasma shown in Figure 3-3

where \Im is the imaginary operator. For a purely symmetric case, these two quantities should be zero. In practice, these values come out 6 to 10 orders of magnitude less than their real components for the purely up-down symmetric systems presented in the next section and in Appendix A

3.3 Verification

With the required modifications completed, it is necessary to verify the new version of the cPFC program. Here, the first verification process is a consistency check against the symmetric version of the program [21]. If everything has been done properly, the results obtained from the symmetric and asymmetric versions of the cPFC code should be identical for symmetrical coil sets and plasmas. This is the case since, as mentioned previously, the Fourier transform of a symmetric function has only real values.

The first verification process presented here consists of testing three different tokamak configurations. For brevity, only one case is given in this chapter, and the others are presented in Appendix A. Each sample configuration is tested in two modes, one where the coils are grouped up-down (i.e. a symmetric pair of coils is forced to carry the same current), and one where each coil in the system is allowed to carry a different current. This provides two checks of the system. First, the currents found using the symmetric and asymmetric versions of the cPFC program should be identical in each mode. Second, since the configurations are perfectly up-down symmetric, the currents found for the grouped and ungrouped modes should also be identical.

Figure 3-5 shows the plasma and coil set of a D shaped tokamak based on the proposed upgrade of the Versator tokamak at MIT. The plasma parameters for this particular case are given in Table 3.1. The coils labeled OHT4, OHB4, OHT5, and OHB5 all carry a fixed current of 15 kiloamps. The remaining coil currents were determined using both the symmetric and asymmetric versions of cPFC. The data for the grouped mode is presented in Table 3.2, while the data for the ungrouped mode is listed in Table 3.3. Finally, as a comparison of how well the equilibrium poloidal field is reproduced by the coil currents, this data is shown in Figure 3-6. The value of ϵ_I for these currents is 0.04, showing that the combination of the coil and plasma currents reproduce the equilibrium poloidal field reasonably well.

It is readily apparent that the data for both the symmetric and asymmetric versions of the cPFC code are identical for both the grouped and ungrouped modes. Similar results are found for

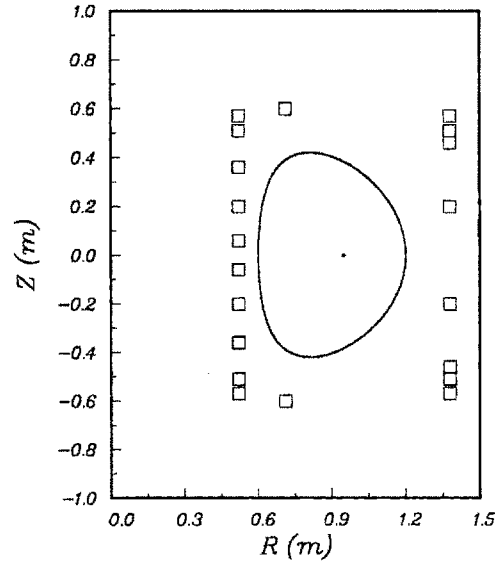


Figure 3-5: Plasma and coil set for the proposed Versator upgrade

Table 3.1: Equilibrium parameters used for the Versator equilibrium.

<i>Parameter</i>	<i>Value</i>
R_0 (m)	0.900
a (m)	0.300
δ	0.300
κ	1.400
B_0 (T)	1.000
I_p (kA)	15.000
β_p	1.031
β_t (%)	0.692

Table 3.2: Data for coil groups OHT1-OHT3 and OHB1-OHB3, EFT1 and EFB1, EFT2 and EFB2, and EFT3-EFT5 and EFB3-EFB5 carrying symmetric currents.

	<i>Symmetric</i>	<i>Asymmetric</i>		<i>Symmetric</i>	<i>Asymmetric</i>
Coil	Current (kA)		Coil	Current (kA)	
OHT1	-2.131	-2.131	OHB1	-2.131	-2.131
OHT2	-2.131	-2.131	OHB2	-2.131	-2.131
OHT3	-2.131	-2.131	OHB3	-2.131	-2.131
EFT1	-1.327	-1.327	EFB1	-1.327	-1.327
EFT2	-9.388	-9.388	EFB2	-9.388	-9.388
EFT3	-14.824	-14.824	EFB3	-14.824	-14.824
EFT4	-14.824	-14.824	EFB4	-14.824	-14.824
EFT5	-14.824	-14.824	EFB5	-14.824	-14.824
	Error (%)				
<i>Field Error</i>	0.04137	0.04137			

Table 3.3: Data for coil groups OHT1-OHT3, OHB1-OHB3, EFT1, EFB1, EFT2, EFB2, EFT3-EFT5 and EFB3-EFB5 carrying unique currents.

	<i>Symmetric</i>	<i>Asymmetric</i>		<i>Symmetric</i>	<i>Asymmetric</i>
Coil	Current (kA)		Coil	Current (kA)	
OHT1	-2.131	-2.131	OHB1	-2.131	-2.131
OHT2	-2.131	-2.131	OHB2	-2.131	-2.131
OHT3	-2.131	-2.131	OHB3	-2.131	-2.131
EFT1	-1.327	-1.327	EFB1	-1.327	-1.327
EFT2	-9.388	-9.388	EFB2	-9.388	-9.388
EFT3	-14.824	-14.824	EFB3	-14.824	-14.824
EFT4	-14.824	-14.824	EFB4	-14.824	-14.824
EFT5	-14.824	-14.824	EFB5	-14.824	-14.824
	Error (%)				
<i>Field Error</i>	0.04137	0.04137			

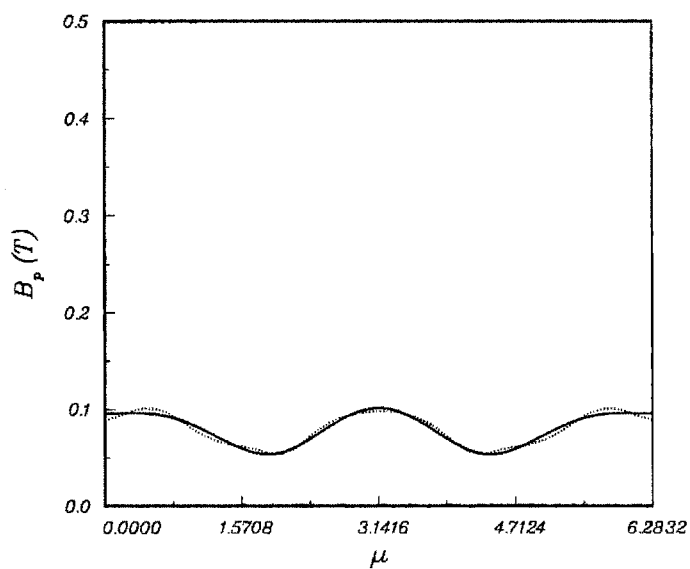


Figure 3-6: Tangential magnetic field as a function of μ . The solid line corresponds to the tangential field at the plasma surface, while the dotted line represents the best fit possible using this coil set and algorithm.

the two cases presented in Appendix A. This supplies verification that the asymmetric version is correct with respect to symmetric plasmas and coil sets. The second step is to test and validate the asymmetric version using an asymmetric system.

3.4 Validation

Validation of the asymmetric version of the program is accomplished using the method described and used by Haney [14]. This method uses several filaments to model the current distribution within the plasma, thereby eliminating the problem of trying to compute an equilibrium using a method which may not be entirely suitable for the given set of poloidal field coils.

The current distribution in the plasma is modeled using a number of filaments. These filaments and those representing the poloidal field coils are then fixed at some appropriate (but essentially arbitrary) values. When the fluxes due to all of these coils are summed, a number of closed flux surfaces are found. By summing the fields from all of these conductors, it is a straightforward matter to compute the tangential field on these closed surfaces. The information about the shape of one particular closed flux surface, the tangential field at that surface, and the total current carried by the filaments representing the plasma is then given to cPFC. The currents found by cPFC can then be compared to those originally used to generate the flux surface. Small differences between the currents used to generate the flux surface and the currents produced by cPFC can be expected due to rounding errors and the finite number of terms used in the Fourier series. Large differences would indicate that the method fails to compute the coil currents correctly.

This procedure will be carried out for two plasma models: one for a symmetric model to demonstrate the method, and one for an asymmetric model to test the asymmetric version of cPFC. Both plasma models are placed within the same coil set, namely a crude model of the Alcator C-Mod coil set.

The symmetric plasma model is shown in Figure 3-7. Note that the eight filaments representing the plasma are symmetrically distributed about the z axis. The triangular shape reasonably models the effects of a double-null divertor configuration.

The locations of the plasma filaments and the currents carried by those filaments are listed in Table 3.4. The currents carried by the poloidal field coils and their locations are given in Table 3.5. The results of running the cPFC program on this system are presented in Table 3.6. For this calculation, each coil was allowed to carry a unique current. The Difference column

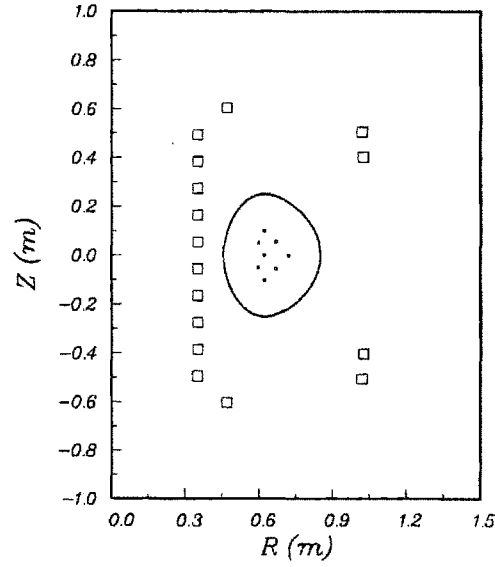


Figure 3-7: Symmetric filament model of plasma current

Table 3.4: Input plasma filament currents for the symmetric test case

<i>Label</i>	<i>R(m)</i>	<i>Z(m)</i>	<i>Current (MA)</i>
Plasma1	0.6190	+0.0000	-1.0000
Plasma2	0.7190	+0.0000	-0.1000
Plasma3a	0.5950	+0.0500	-0.1000
Plasma3b	0.5950	-0.0500	-0.1000
Plasma4a	0.6680	+0.0550	-0.7000
Plasma4b	0.6680	-0.0550	-0.7000
Plasma5a	0.6190	+0.1010	-0.1000
Plasma5b	0.6190	-0.1010	-0.1000

Table 3.5: Input poloidal field coil currents for cPFC validation

<i>Label</i>	<i>R(m)</i>	<i>Z(m)</i>	<i>Current (MA)</i>
PF1a	0.4690	+0.6040	-0.5870
PF1b	0.4690	-0.6040	-0.5870
PF2a	1.0200	+0.5060	+0.9340
PF2b	1.0200	-0.5060	+0.9340
PF3a	1.0250	+0.4030	+0.9340
PF3b	1.0250	-0.4030	+0.9340
OH1a	0.3500	+0.0550	+0.9900
OH1b	0.3500	-0.0550	+0.9900
OH2a	0.3500	+0.1650	+0.9900
OH2b	0.3500	-0.1650	+0.9900
OH3a	0.3500	+0.2740	+0.9900
OH3b	0.3500	-0.2740	+0.9900
OH4a	0.3500	+0.3840	+0.9900
OH4b	0.3500	-0.3840	+0.9900
OH5a	0.3500	+0.4940	+0.9900
OH5b	0.3500	-0.4940	+0.9900

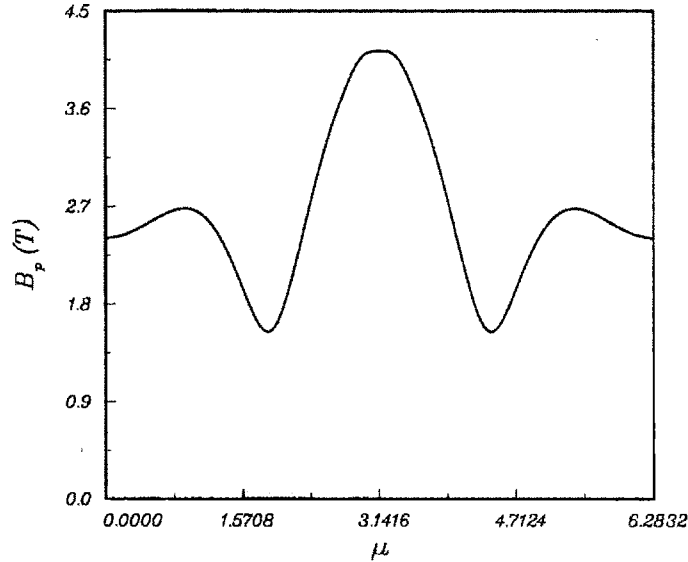


Figure 3-8: Poloidal fields for the symmetric test case. The solid line is the poloidal field at the plasma surface for the equilibrium. The dotted line (indistinguishable here) represents the combined fields of the plasma and the poloidal field coils.

listed in Table 3.6 is computed from

$$d = (i - o)/i$$

where d is the difference, i is the input current and o is the output current. A negative difference simply means that the coil current found by cPFC was larger than the input current.

Inspection of the values in Table 3.6 shows that the cPFC program reproduces the input coil currents to an accuracy of better than 0.02 %. This indicates that the program is correctly calculating the coil currents for this case. Further indication of how well the coil currents are being reproduced is illustrated in Figure 3-8, which compares the input poloidal field with that generated by the coil currents listed in Table 3.6. The field error (ϵ_I) for this case is $1.4 \cdot 10^{-4}$ %.

For the asymmetric case, two of the filaments listed in Table 3.4 were removed and the current carried by those filaments was redistributed accordingly. The resulting asymmetric plasma current distribution is modeled by the filaments in Table 3.7. The poloidal field coil currents and positions used for this case are identical to those listed in 3.5. Figure 3-9 shows the coils, plasma filaments,

Table 3.6: Comparison between input and output values of the poloidal field coil currents used for the symmetric test case.

<i>Label</i>	Input Current (MA)	Output Current (MA)	Difference (%)
PF1a	-0.5870	-0.5868	+0.02480
PF1b	-0.5870	-0.5869	+0.02467
PF2a	+0.9340	+0.9339	+0.00694
PF2b	+0.9340	+0.9339	+0.00693
PF3a	+0.9340	+0.9340	-0.00420
PF3b	+0.9340	+0.9340	-0.00419
OH1a	+0.9900	+0.9899	+0.00137
OH1b	+0.9900	+0.9899	+0.00136
OH2a	+0.9900	+0.9899	+0.00132
OH2b	+0.9900	+0.9899	+0.00132
OH3a	+0.9900	+0.9899	+0.00213
OH3b	+0.9900	+0.9899	+0.00211
OH4a	+0.9900	+0.9901	-0.01337
OH4b	+0.9900	+0.9901	-0.01325
OH5a	+0.9900	+0.9896	+0.03746
OH5b	+0.9900	+0.9896	+0.03724

Table 3.7: Input plasma filament currents for the asymmetric test case

<i>Label</i>	R(m)	Z(m)	Current (MA)
Plasma1	0.6190	+0.0000	-1.3500
Plasma2	0.7190	+0.0000	-0.4500
Plasma3a	0.5950	+0.0500	-0.1000
Plasma3b	0.5950	-0.0500	-0.2500
Plasma4b	0.6680	-0.0550	-0.7500
Plasma5b	0.6190	-0.1010	-0.1000

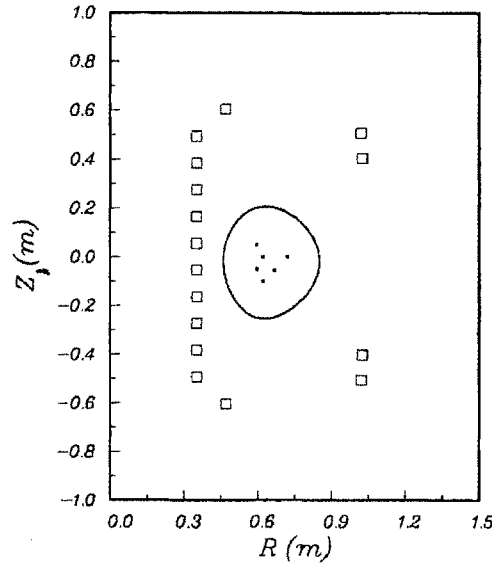


Figure 3-9: Flux surface for the asymmetric case

and resulting flux surface for this case. Here, the triangularity in the lower half of the flux surface models a single-null divertor.

As for the symmetric case, the results obtained by running cPFC for this case indicate that the program is computing the coil currents correctly. This can be verified by examining Table 3.8. Here, the worst case differs from the input current by 0.614 % (coil OH5a). This is a factor of twenty higher than the symmetric case, but is still acceptable as proof that cPFC is finding the coil currents properly. This can also be seen by examining Figure 3-10, which shows both the poloidal field at the flux surface and the resulting poloidal field computed by cPFC. The field error for this case is $1.2 \cdot 10^{-4}$ %, so the two lines in Figure 3-10 are indistinguishable.

As a final example, consider the plasma and coil set shown in Figure 3-11. This equilibrium is far more asymmetric than that used for the previous test. The coil set shown in Figure 3-11 is a more advanced design of the Alcator C-Mod poloidal field coil system. The locations of the wires making up the various coils shown in Figure 3-11 are given in Appendix B. The equilibrium used in this case is characterized by the parameters given in Table 3.9. The poloidal fields for this case are shown in Figure 3-12. Examining this figure shows that cPFC is doing a reasonable job of reproducing the equilibrium field, with a field error of 5.693 %.

Table 3.8: Comparison between input and output values of the poloidal field coil currents used for the asymmetric test case.

<i>Label</i>	Input Current (MA)	Output Current (MA)	Difference (%)
PF1a	-0.5870	-0.5849	-0.35024
PF1b	-0.5870	-0.5876	-0.10126
PF2a	+0.9340	+0.9336	-0.04354
PF2b	+0.9340	+0.9340	+0.00869
PF3a	+0.9340	+0.9342	+0.02466
PF3b	+0.9340	+0.9339	-0.00701
OH1a	+0.9900	+0.9899	+0.00761
OH1b	+0.9900	+0.9899	+0.00595
OH2a	+0.9900	+0.9900	-0.00289
OH2b	+0.9900	+0.9899	+0.00768
OH3a	+0.9900	+0.9893	+0.06891
OH3b	+0.9900	+0.9900	-0.00345
OH4a	+0.9900	+0.9933	-0.33552
OH4b	+0.9900	+0.9893	+0.07122
OH5a	+0.9900	+0.9839	+0.61364
OH5b	+0.9900	+0.9911	-0.11596

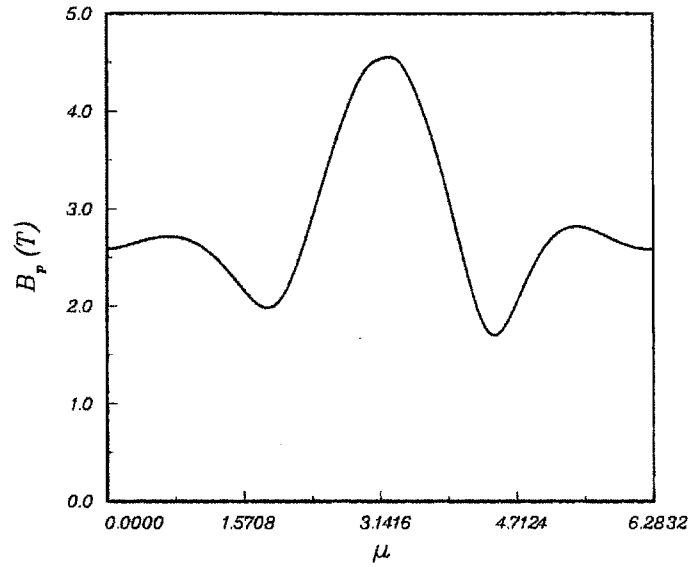


Figure 3-10: Plot of the tangential component of the poloidal field for the asymmetric test case. The solid line represents the field due to the plasma. The indistinguishable dotted line is the field due to the plasma and the PF coils.

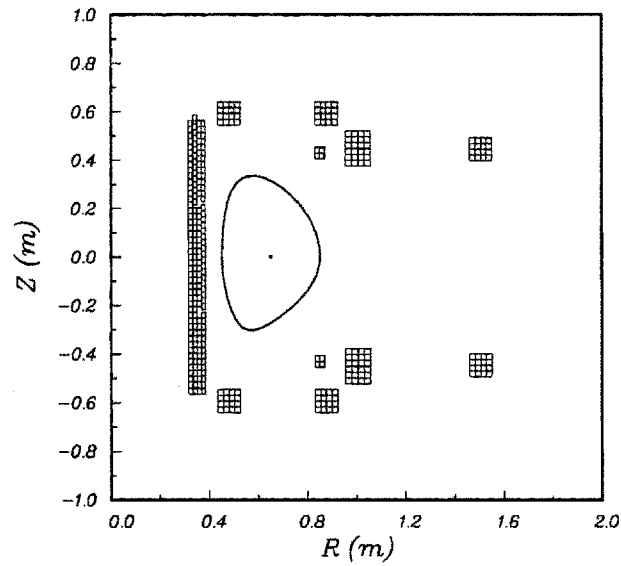


Figure 3-11: A single null diverted plasma and the Alcator C-Mod coil set

Table 3.9: Equilibrium parameters for the Alcator single null equilibrium.

<i>Parameter</i>	<i>Value</i>
R_0 (m)	0.650
a (m)	0.210
δ_u	0.384
δ_l	0.446
κ_u	1.708
κ_l	1.554
B_0 (T)	9.000
I_p (MA)	2.500
β_p	0.292
β_t (%)	1.070

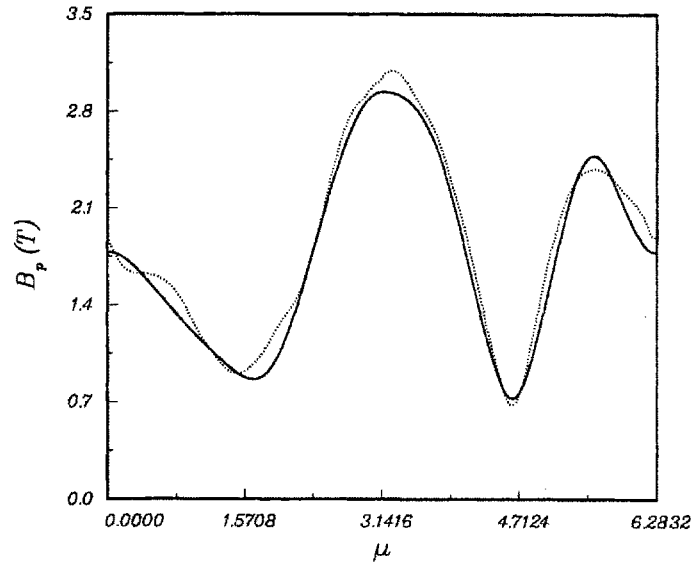


Figure 3-12: Poloidal fields for the C-Mod single null test case. The solid line is the tangential component of the poloidal field due to the plasma. The dotted line represents the combined fields of the plasma and the PF coil set.

Chapter 4

Linear Constraints

The previous chapter discussed the transformation of the cPFC program into a general purpose tool for computing the coil currents required to support a given equilibrium. In this chapter, linear limits on the coil currents are incorporated into cPFC. These limits arise from engineering considerations for the poloidal field coils. The chapter begins with a discussion of the engineering factors that limit the current that a coil can carry.

4.1 The Source of the Constraints

The way in which current limits arise depends on the type of magnet being used. In resistive magnets, the coil temperature is one limiting factor on the magnitude of the current, while superconducting magnets have temperature, magnetic field, and current limits that must be satisfied. The details of these limits are examined in the next two sections.

4.1.1 Resistive Magnets

Linear constraints on the coil currents of a system of resistive magnets come about due to temperature considerations. As a demonstration of how the maximum allowable temperature in a coil limits the current flowing in that coil, consider a long, straight resistive wire with a circular cross section. The maximum temperature allowed in the wire is defined to be T_0 . The amount of power (P) deposited as heat in the wire is given by

$$P = I^2 RL$$

where R is the wire's resistance per unit length, L is the total length of the wire and I is the current flowing through the wire.

Knowing the power dissipated in the wire makes it possible to determine the temperature distribution of the wire from

$$\kappa \nabla^2 T + P = \rho c_p \frac{\partial T}{\partial \tau}$$

where τ is time, κ is the thermal conductivity of the wire, ρ is the wire's density and c_p is the specific heat of the wire. For simplicity, κ , ρ and c_p are assumed to be independent of temperature. Furthermore, assuming a steady state condition removes the time dependence from this equation, resulting in

$$\nabla^2 T = -\frac{P}{\kappa}$$

The general solution to this Equation [19] is given by

$$T = \frac{\dot{q}}{4\kappa} (r_0^2 - r^2) + T_s \quad (4.1)$$

where r is the radial position, r_0 is the radius of the wire, T_s is the temperature at the surface of the wire ($r = r_0$), and \dot{q} is the volumetric heat generation, given by

$$\dot{q} = \frac{P}{\pi r_0^2 L}$$

The temperature distribution described by Equation 4.1 is parabolic and has a maximum at $r = 0$, corresponding to the center of the wire.

The surface temperature of the wire is found by applying an appropriate boundary condition. For this case, the wire is assumed to be undergoing convective heat transfer with a cooling medium. The heat transfer rate to the coolant (C) is given by

$$C = hA(T_s - T_b)$$

where h is a heat transfer coefficient, A is the surface area over which cooling is taking place, T_s is the temperature of the wire's surface, and T_b is the bulk temperature of the coolant. The previous assumption of being at steady state gives

$$I^2 RL = hA(T_s - T_b)$$

This equation yields T_s , which can then be substituted into Equation 4.1 to obtain the temperature at the center of the wire (T_c). The equation for T_c is

$$T_c = \frac{P}{4\pi L\kappa} + T_s = I^2 R \left(\frac{1}{4\pi\kappa} + \frac{L}{hA} \right) + T_b$$

As discussed earlier, the maximum temperature occurs at the center of the wire. For the current case, this means that T_c must be less than or equal to T_0 . This translates into

$$I^2 R \leq \frac{4\pi\kappa h A (T_0 - T_b)}{h A + 4\pi\kappa L}$$

The maximum current in the wire is then found by taking the square root in the previous equation:

$$I_{max} = \left[\frac{1}{R} \left(\frac{4\pi\kappa h A (T_0 - T_b)}{h A + 4\pi\kappa L} \right) \right]^{1/2} \quad (4.2)$$

Thus, the current allowed to flow through the coil due to the temperature considerations is given by $-I_{max} \leq I \leq I_{max}$. The upper and lower bounds on I act as a constraint, and since the exponent of I is unity, the constraint is linear.

4.1.2 Superconducting Magnets

Superconducting magnet materials exhibit a complex behavior in the phase space defined by current density, magnetic field, and temperature. The critical values of these parameters are defined as the point at which the superconducting nature of the material is lost. Since a superconductor has essentially no electrical resistance, Ohmic heating is not a factor in the current limits. Instead, the temperature of the superconductor can change through internal energy fluctuations or nuclear interactions. For the purposes of this discussion, the critical current will be assumed to be the only limiting factor to the coil current.

Present designs for superconducting magnets consist of a series of superconducting filaments embedded in a metallic substrate. The substrate serves as a backup in case part of the superconductor fails temporarily due to a local temperature increase and acts as a heat sink. Consider a magnet composed of Niobium-Tin filaments which have a circular cross-section. At 4.2 K and in a 5 T magnetic field, the critical current density for Niobium-Tin is approximately $5 \cdot 10^9$ A/m². If the total filaments have a cross-sectional area of 5 cm², the maximum current the magnet can carry is 100 kA. Thus, in a grossly oversimplified situation, the critical current acts as the limiting factor on the current that a superconducting magnet can carry.

4.2 Problem Statement

As presented in Chapter 2, the problem of finding the poloidal field coil currents was simply that of minimizing the functional

$$\epsilon_I(\mathbf{i}) = \mathbf{i}^T \cdot \mathbf{M} \cdot \mathbf{i} - 2\mathbf{n}^T \cdot \mathbf{i} + p \quad (4.3)$$

Since M is a symmetric matrix, this problem reduces to finding the solution of

$$M \cdot \mathbf{i} = \mathbf{n} \quad (4.4)$$

Now, assume that a particular current i_k is subject to a maximum current constraint of the form

$$|i_k| \leq b_k$$

More generally, if a finite subset of the group currents is subject to a set of inequality constraints, the constraint equations take the form

$$-b \leq \mathbf{l} \leq b \quad (4.5)$$

where \mathbf{l} denotes the constrained subset of the grouped currents. The problem of finding the coil currents subject to the linear constraints is formally expressed as

$$\begin{aligned} &\text{Minimize} && \mathbf{i}^T \cdot M \cdot \mathbf{i} - 2\mathbf{n}^T \cdot \mathbf{i} + p \\ &\text{Subject to} && -b \leq \mathbf{l} \leq b \end{aligned} \quad (4.6)$$

Equation 4.6 is commonly referred to as an *optimization* problem. To simplify the discussion, some of the nomenclature involved in optimization problems is now presented [9]. Any set of currents \mathbf{i} that satisfy the constraints defined by Equation 4.5 represents a *feasible* point. A point \mathbf{i} which satisfies all of the constraints and minimizes ϵ_I is called *optimal*. For constraints involving inequalities, a satisfied constraint is called *inactive* and one which is violated is described as *active*. In general, solving a problem with inequality constraints is difficult. This difficulty arises because at any step in the solution process, none, some, or all of the constraints may be active, so that it is impossible to tell *a priori* which of the inequalities ultimately appear as constraints.

There are a variety of problems associated with the determination of an optimal point of a quadratic system with linear inequality constraints – precisely the problem expressed in Equation 4.6. The worst of these is the issue of convergence. Since one of the goals of this work is to build a fast, robust system, a system which may not converge to one set of \mathbf{i} is undesirable. Rather than face these problems, the goal of minimizing $\epsilon_I(\mathbf{i})$ subject to the constraints is simplified to that of finding a feasible point. This is accomplished by assuming that if the global minimum found in Equation 4.4 does not satisfy the constraints, then a feasible point will not perturb the system too far from the global minimum, with the field error serving as an estimate of the quality of the solution. The formulae for estimating a feasible point are developed in the next section.

4.3 Finding a Feasible Point

The goal of this section is to find a feasible point of Equation 4.6. To do this, an intermediate expression for Equation 4.6 is developed using the Lagrange multiplier technique. The result can then be treated in a fairly straightforward manner.

Originally, the problem simply required finding a minimum of the expression

$$\epsilon_I(\mathbf{i}) = \mathbf{i}^T \cdot \mathbf{M} \cdot \mathbf{i} - 2\mathbf{n}^T \cdot \mathbf{i} + p$$

The presence of linear inequality constraints transformed this problem to the problem stated by Equation 4.6. Since each constraint is independent of the others, Equation 4.6 can be replaced by the auxiliary function [16]

$$\varphi(\mathbf{i}) = \mathbf{i}^T \cdot \mathbf{M} \cdot \mathbf{i} - 2\mathbf{n}^T \cdot \mathbf{i} + p + \lambda^T \cdot \mathbf{g} \quad (4.7)$$

where λ is a vector of Lagrange multipliers and \mathbf{g} is a vector whose elements are defined by the constraint equations:

$$g_n = l_n - b_n \quad (4.8)$$

Here, l is the constrained subset of \mathbf{i} . The combination of Equation 4.7 and the constraint equations form a linear system which can be minimized. This is accomplished by setting the derivative of Equation 4.7 with respect to \mathbf{i} equal to zero and imposing the constraint equations. The first three terms on the right-hand side of Equation 4.7 can simply be replaced by $\epsilon_I(\mathbf{i})$, whose derivative with respect to \mathbf{i} is known, resulting in

$$\frac{\partial \varphi}{\partial \mathbf{i}} = \mathbf{M} \cdot \mathbf{i} - \mathbf{n} + \frac{\lambda^T}{2} \cdot \frac{\partial \mathbf{g}}{\partial \mathbf{i}} \quad (4.9)$$

The derivative of \mathbf{g} can be found using

$$\frac{\partial g_n}{\partial i_j} = \delta_{n,j} \quad (4.10)$$

where $\delta_{n,j}$ is a selection function defined as

$$\delta_{n,j} = \begin{cases} 1 & \text{if } l_n \text{ corresponds to the current } i_j \\ 0 & \text{otherwise} \end{cases} \quad (4.11)$$

For N total grouped currents, of which K are constrained, Equation 4.9 yields N equations in $N + K$ unknowns (the N variables \mathbf{i} and the K values of λ). The K constraint equations complete the system, giving $N + K$ equations in $N + K$ unknowns. The next step is to find a method of solving the system in light of the inequalities in the constraint equations.

4.4 Numerical Implementation

Although the equations developed in the previous section appear straightforward to solve, this is not the case because of the inequalities in the constraint equations. The algorithm which is best suited to this case is an adaptation of Newton's method to systems of nonlinear equations [2]. The details of this algorithm are presented in this section.

Newton's method arises from attempting to find a fixed point x for the function $h(x)$ defined by

$$h(x) = x - \phi(x)f(x)$$

The fixed point of $h(x)$ is defined as the point p where $h(p) = p$. From this definition, it is obvious that $\phi(p)f(p) = 0$. The one dimensional version of Newton's method arises from the desire to find a functional form for $\phi(x)$ with the property that $h(x)$ converges quadratically to the fixed point p . Newton's method comes about directly from this condition by choosing $\phi(x) = 1/f'(x)$, provided that $f'(p) \neq 0$.

Approaching the n -dimensional case in a similar manner involves finding a matrix

$$\mathbf{A}(\mathbf{x}) = \begin{bmatrix} a_{11}(\mathbf{x}) & a_{12}(\mathbf{x}) & \cdots & a_{1n}(\mathbf{x}) \\ a_{21}(\mathbf{x}) & a_{22}(\mathbf{x}) & \cdots & a_{2n}(\mathbf{x}) \\ \vdots & \vdots & & \vdots \\ a_{n1}(\mathbf{x}) & a_{n2}(\mathbf{x}) & \cdots & a_{nn}(\mathbf{x}) \end{bmatrix} \quad (4.12)$$

such that the equation

$$\mathbf{H}(\mathbf{x}) = \mathbf{x} - \mathbf{A}(\mathbf{x})^{-1}\mathbf{F}(\mathbf{x}) \quad (4.13)$$

gives quadratic convergence to the fixed point of $\mathbf{F}(\mathbf{x}) = \mathbf{0}$, provided that $\mathbf{A}(\mathbf{x})$ is nonsingular at the fixed point. The appropriate choice for the matrix $\mathbf{A}(\mathbf{x})$ is the Jacobian of $\mathbf{F}(\mathbf{x})$. Denoting the Jacobian $\mathbf{J}(\mathbf{x})$, Equation 4.13 becomes

$$\mathbf{H}(\mathbf{x}) = \mathbf{x} - \mathbf{J}(\mathbf{x})^{-1}\mathbf{F}(\mathbf{x}) \quad (4.14)$$

where the Jacobian is determined from [17]:

$$\mathbf{J}(\mathbf{x}) = \begin{bmatrix} \frac{\partial F_1(\mathbf{x})}{\partial x_1} & \frac{\partial F_1(\mathbf{x})}{\partial x_2} & \cdots & \frac{\partial F_1(\mathbf{x})}{\partial x_N} \\ \frac{\partial F_2(\mathbf{x})}{\partial x_1} & \frac{\partial F_2(\mathbf{x})}{\partial x_2} & \cdots & \frac{\partial F_2(\mathbf{x})}{\partial x_N} \\ \vdots & \vdots & & \vdots \\ \frac{\partial F_N(\mathbf{x})}{\partial x_1} & \frac{\partial F_N(\mathbf{x})}{\partial x_2} & \cdots & \frac{\partial F_N(\mathbf{x})}{\partial x_N} \end{bmatrix} \quad (4.15)$$

The solution to this system is found by iterating from an initial guess, with the iteration scheme being

$$\mathbf{x}^{n+1} = \mathbf{x}^n - \mathbf{J}(\mathbf{x}^n)^{-1} \cdot \mathbf{F}(\mathbf{x}^n) \quad (4.16)$$

Adapting this system to the formulae presented in the previous section is fairly straightforward. The first N elements of \mathbf{x} represent the grouped currents \mathbf{i} of the system. The remaining K elements are the Lagrange multipliers. From Equation 4.9, the first N equations of the $\mathbf{F}(\mathbf{x})$ vector are of the form

$$F_i(\mathbf{x}) = \sum_{j=1}^N M_{ij} x_j - n_j + \frac{1}{2} \sum_{j=1}^K \lambda_j \frac{\partial g_j}{\partial i_i} \quad (4.17)$$

and the final K equations are given by the constraint equations \mathbf{g} . $\mathbf{F}(\mathbf{x})$ for the K constraint equations is evaluated from

$$F_j(\mathbf{x}) = \begin{cases} l_j - b_j & \text{if } l_j > b_j \\ 0 & \text{if } -b_j \leq l_j \leq b_j \\ l_j + b_j & \text{if } l_j < -b_j \end{cases} \quad (4.18)$$

where l_j corresponds to the k th constrained element of \mathbf{x} . Finally, the first N rows of the Jacobian matrix are evaluated directly from Equation 4.17, and the derivatives of the K constraint equations are evaluated from the form given in Equations 4.10 and 4.11.

There are two potential problems to using the iteration scheme defined by Equation 4.16. The first of these is the need to evaluate the Jacobian matrix for each iteration. Careful examination of the equations used, however, shows that the Jacobian is constant for this case, so it only has to be evaluated once. The other problem is that the Jacobian has to be inverted at each iteration. In practice, Equation 4.16 is evaluated in two steps: first

$$\mathbf{J}(\mathbf{x}) \cdot \mathbf{y} = -\mathbf{F}(\mathbf{x}) \quad (4.19)$$

is computed, followed by

$$\mathbf{x}^{n+1} = \mathbf{x}^n + \mathbf{y} \quad (4.20)$$

where \mathbf{y} is the update vector corresponding to $-\mathbf{J}(\mathbf{x})^{-1}\mathbf{F}(\mathbf{x})$.

The stopping criterion for this algorithm is simply that the solution has been found when all of the constraints are inactive. This condition indicates that a feasible point has been found.

To summarize, the algorithm for finding the feasible point works in the following manner. First, the unconstrained solution is found. Then, the Jacobian matrix is computed. The Jacobian

matrix is then used to iteratively solve $F(\mathbf{x}) = 0$, with the iteration process terminating when all of the constraints are satisfied.

With an algorithm capable of finding a feasible point of the system given in Equation 4.6, the next step is to test it. But first, it is necessary to go over the derivation just presented and clarify a few points.

4.5 Avoiding Singularities

The iteration scheme for Newton's method is based on

$$x^{n+1} = x^n - \frac{f(x)}{f'(x)} \quad (4.21)$$

This scheme's major downfall occurs when $f'(x) = 0$, resulting in a singularity. A similar problem occurs with the algorithm given in the previous section. Recall that the constraint equations were expressed as

$$g_n = l_n - b_n \quad (4.22)$$

where l is the constrained subset of the coil currents. Rigorously, the constraint equations are

$$g_n = \begin{cases} l_n - b_n & \text{if } l_n > b_n \\ 0 & \text{if } -b_n < l_n < b_n \\ l_n + b_n & \text{if } l_n < -b_n \end{cases} \quad (4.23)$$

The derivative of this expression is

$$\frac{\partial g_n}{\partial i_j} = \begin{cases} \delta_{n,j} & \text{if } l_n > b_n \\ 0 & \text{if } -b_n < l_n < b_n \\ \delta_{n,j} & \text{if } l_n < -b_n \end{cases} \quad (4.24)$$

where $\delta_{n,j}$ is given by Equation 4.11. If the constraint is inactive, the derivative is zero, resulting in a singular Jacobian.

The standard approach to this would be to eliminate the inactive constraint from the system [8]. This results in a computationally intensive algorithm which shrinks and expands the system of equations as constraints become inactive or active. This method can also converge to a set of two points, one where a constraint is inactive and another where the constraint is active. The iteration scheme would then move from one point to another, never converging. Since the goal of this process is to find a feasible point rather than an optimum, these issues can be avoided entirely.

The algorithm presented in the previous section should suffice, provided that the singularities can be eliminated or avoided.

The problem of a singular Jacobian can be avoided by using Equation 4.10. Treating the derivative in this manner has no effect on the calculation of the coil currents, as will now be demonstrated.

Consider an inactive constraint equation from the linear system in Equation 4.19. This equation has the form

$$\frac{\partial g_j}{\partial i_n} y_n = F_n(i)$$

Since the constraint is inactive, $F_n(i) = 0$. Using Equation 4.24 to evaluate the derivative would result in the indeterminate solution

$$y_n = \frac{0}{0}$$

If Equation 4.10 is used, the solution would be

$$y_n = \frac{0}{1} = 0$$

The expected solution is $y_n = 0$: the current should not be changed if the constraint is inactive. Finally, using equation 4.10 to evaluate the derivative of g in Equation 4.17 affects only the calculation of the Lagrange multipliers, not the coil currents. Thus, by using Equation 4.10 the correct results are obtained and the problem of a singular Jacobian is avoided.

4.6 Verification, Validation, and Testing

Since the algorithm described in Section 4.5 is invoked only if current constraints are specified, verification of the program only requires ensuring that the results obtained for the cases presented in Section 3.3 and in Appendix A are identical. As expected, the results did match, indicating that the linear constraint algorithm has no global side effects in the cPFC program.

Validation and testing the linear constraint algorithm is straightforward. It is only necessary to run a set of cases which have varying numbers of constraints and ensure that the results satisfy those constraints. This will be done for the equilibrium and coil set depicted in Figure 4-1. The parameters characterizing this equilibrium are listed in Table 4.1.

The coil set shown in Figure 4-1 represents the Alcator C-Mod tokamak at MIT. It is composed of 335 wires making up 13 unique coils. Of these, 3 coils carry fixed currents: the OH1 coil carries a total current of 1.4964 MA, the EFC upper coil carries 3.0000 kA, and the lower EFC

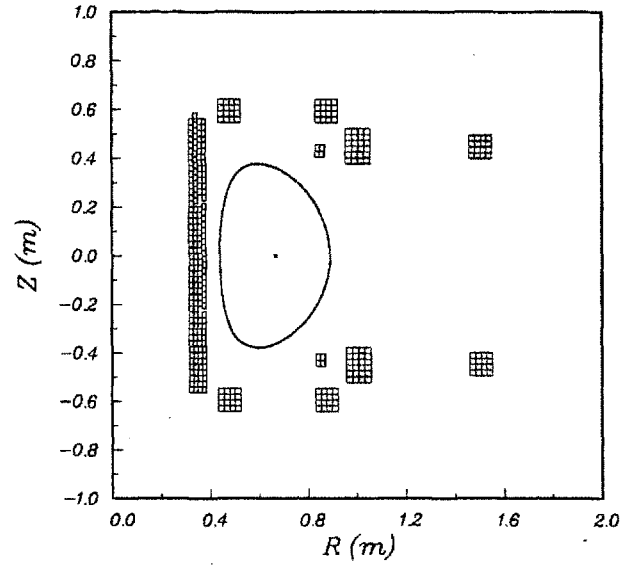


Figure 4-1: The Alcator C-Mod equilibrium and coil set used to validate and test the linearly constrained coil current algorithm.

Table 4.1: Equilibrium data for the Alcator C-Mod test case.

<i>Parameter</i>	<i>Value</i>
R_0 (m)	0.665
a (m)	0.225
δ	0.310
κ	1.680
B_0 (T)	8.500
I_p (MA)	2.500
β_p	0.500
β_t (%)	0.017

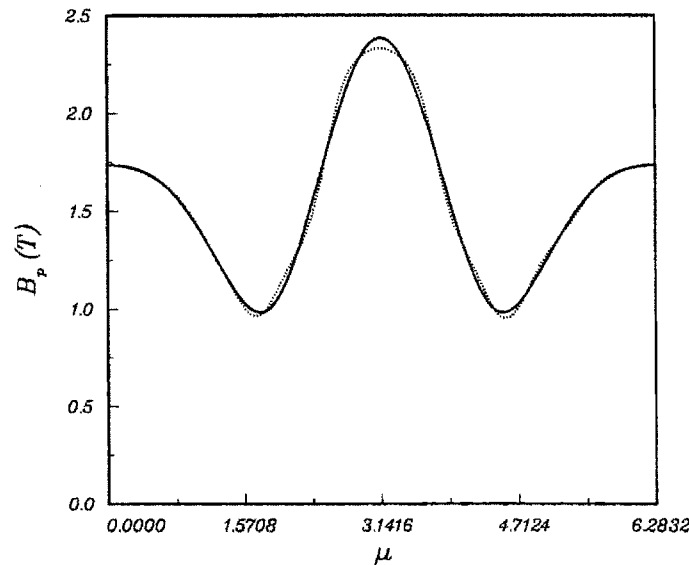


Figure 4-2: Comparison of the tangential components of the equilibrium poloidal field (solid line) and that produced by the combination of the plasma and coil set (dotted line) for the Alcator C-Mod test case with no constraints.

coil carries -3.0000 kA. The sign on the currents is relative to the direction of the plasma current, so a negative current is flowing opposite the plasma current. As a reference, locations of the wires making up the various coils are listed in Appendix B. In addition, the initial operating mode has the EF3 and EF4 coils grouped. The results obtained for the unconstrained case are shown in Figure 4-2. The field error for this case is 1.408 %.

The first test to be made is to determine if the algorithm of Section 4.5 actually works. Examining the coil currents produced by the unconstrained case (listed with the results of all of the tests in Table 4.2) shows that the current in each wire of the upper EF1 coil is 51.27 kA. Limiting this current to 50.00 kA should provide a good test of the system. The results of this test are shown in Figure 4-3. Comparing this figure to Figure 4-2 shows a slight difference in the region of $\mu = \pi/2$. Since the constraint was set to a value very nearly equal to that produced by the unconstrained case, only slight differences are expected between the two cases. This is further born out by the field error, which for this case is 1.431 %, just a little larger than the 1.408 % error produced by the unconstrained case. Finally, examining the results listed in Table 4.2 shows that the constraint has been satisfied.

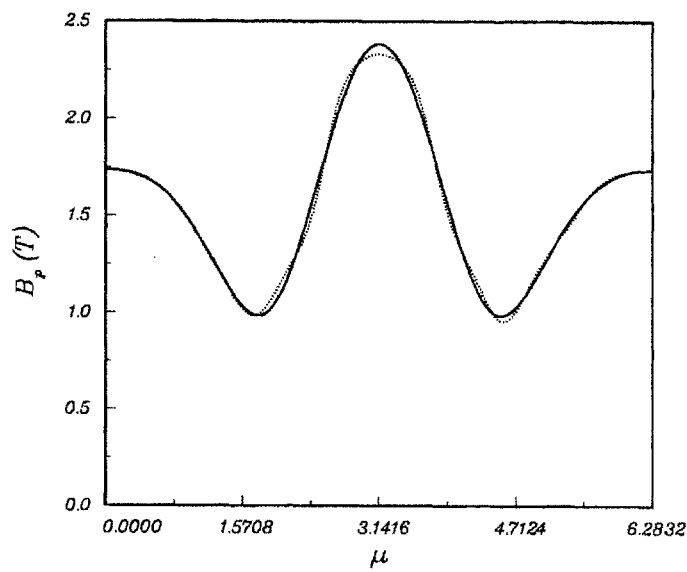


Figure 4-3: Comparison of the equilibrium poloidal field and that produced by the combination of the plasma and coil set when the upper EFC coil current is constrained to a maximum current of 50.00 kA.

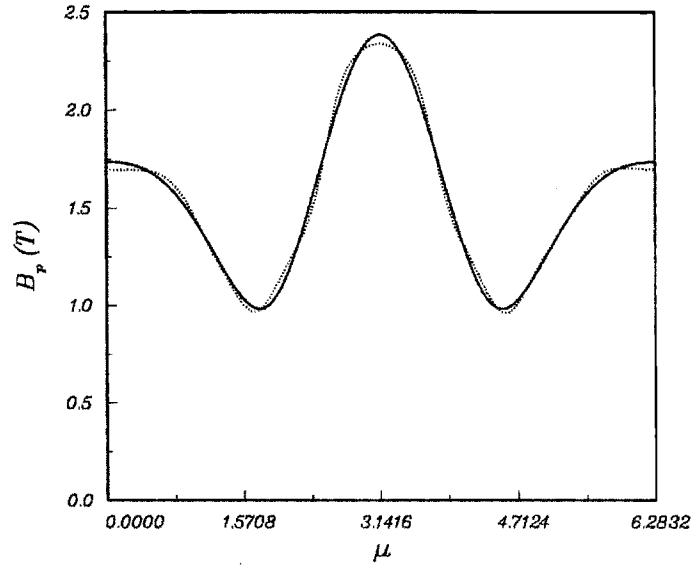


Figure 4-4: Comparison of the equilibrium poloidal field and that produced by the combination of the plasma and coil set when both the upper EFC coil current and the EF4 coil currents are constrained to a maximum current of 50.00 kA.

The next test is to ensure that multiple violated constraints are satisfied. This is accomplished by setting the maximum current in the EF4 coils to 50.00 kA and retaining the constraint on the EF1 upper coil. This constraint is also violated by the currents found in the unconstrained case. The effects of this constraint are much larger, as can be seen by examining Figure 4-4. The difference between the equilibrium poloidal field and the field produced by the coils is now markedly different in the region around $\mu = 0 = 2\pi$. The field error for this case is 1.822 %.

The next case retains the two constraints just tested, and adds one which is satisfied in the unconstrained case but is violated by the feasible point found in the previous test. For this, the current flowing in the wires of the EF3 coils is limited to a maximum value of 8.35 kA. The current in these wires from the unconstrained case is 4.45 kA. The tangential poloidal field for this test is illustrated in Figure 4-5. The field error for this test is 2.977 %.

These results are substantially worse than those of the previous test. If the goal of the constraint solving algorithm was to find an optimal or near optimal point of this system, these results would be unacceptable. Since, however, the goal of the algorithm was to determine a feasible point, these results satisfy that requirement. The reason for this discrepancy will be

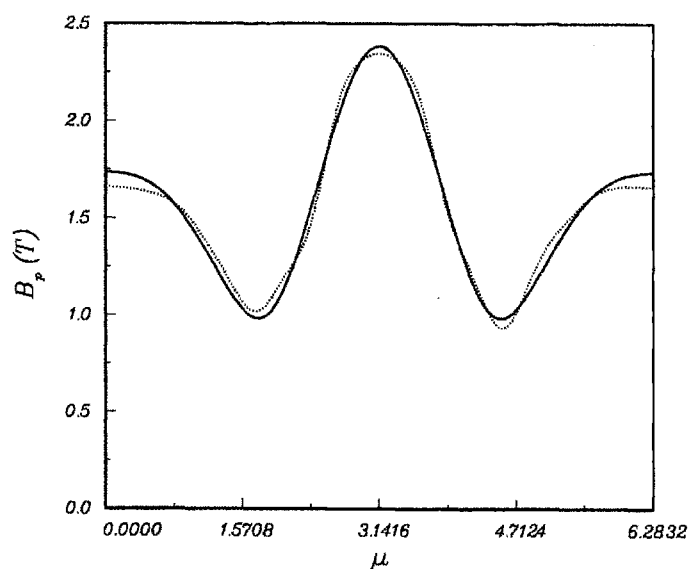


Figure 4-5: Comparison of the equilibrium poloidal field and that produced by the combination of the plasma and coil set when both the upper EFC coil current and the EF4 coil currents are constrained to a maximum current of 50.00 kA, and the current in the EF3 coil is set to a maximum of 8.35 kA.

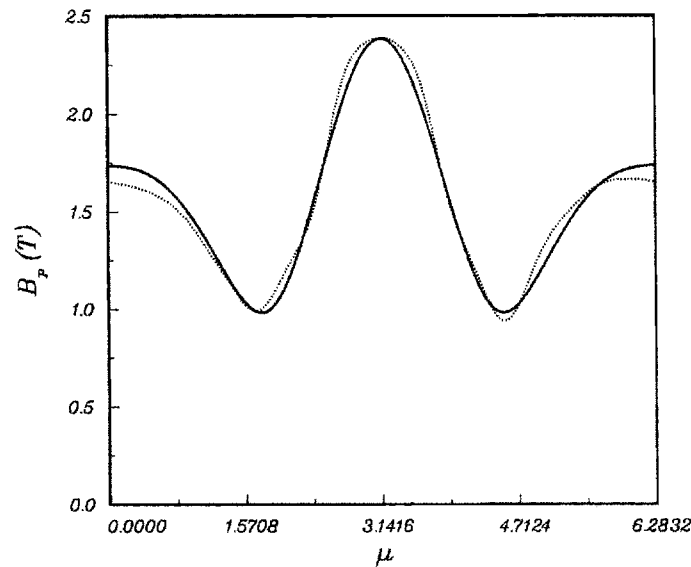


Figure 4-6: Comparison of the equilibrium poloidal field and that produced by the combination of the plasma and coil set when both the upper EFC coil current and the EF4 coil currents are constrained to a maximum current of 50.00 kA, the current in the EF3 coil is set to a maximum of 8.35 kA, and the current in the upper coil of EF2 is limited to 100.00 kA.

discussed at the end of the present chapter.

The final test to run is an extension of the previous case, namely a test where the unconstrained result violate two constraints and satisfy two constraints. Based on the results of the previous case, the results of this test should be worse. Here, in addition to the three constraints imposed previously, the current in the wires of the EF2 upper coil is limited to a maximum value of 100.00 kA. This case yields a field error of 3.718 %, and the resulting field is compared with the equilibrium field in Figure 4-6.

The coil currents for these 5 test cases are summarized in Table 4.2.

4.7 Discussion

As demonstrated in the previous section, the algorithm presented in Section 4.5 finds a feasible point for the system. However, for inactive constraints, the solution has a larger field error than

Table 4.2: Summary of the test results for the linear constraint algorithm

	Number of constraints:				
	0	1	2	3	4
Coil	Current (kA)				
OH2U	30.885	31.260	31.155	31.785	31.871
OH2L	30.186	30.273	30.545	29.685	30.455
EF1U	51.274	50.000	50.000	50.000	50.000
EF1L	54.836	54.505	53.271	58.140	58.774
EF2U	6.618	7.685	10.097	3.042	6.618
EF2L	-0.589	0.101	3.005	-5.975	-6.654
EF3U	-4.450	-4.921	-8.352	-4.450	-4.450
EF3L	-4.450	-4.921	-8.352	-4.450	-4.450
EF4U	-54.720	-54.421	-50.000	-50.000	-50.000
EF4L	-54.720	-54.421	-50.000	-50.000	-50.000
Field Error (%)					
	1.408	1.431	1.822	2.977	3.718

necessary. Specifically, the last three columns of Table 4.2 should be identical.

These undesirable results are directly related to the algorithm. Recall that the update vector y is found from

$$\mathbf{J}(\mathbf{x}) \cdot \mathbf{y} = \mathbf{F}(\mathbf{x})$$

If the i th constraint is inactive, then $F_m(x) = 0$, where F_m is the equation corresponding to the i th constraint equation. This sets $y_m = 0$, which does not allow the current to vary. Since the current does not vary, the constraint is inactive for the next iteration. The net effect of this is that a constraint which is inactive from the global minimization process locks the value of the corresponding current to the value of that current at the global minimum.

With a small number of coils (13 for the case of Alcator C-Mod), a simple method for using the program would be to:

- Run cPFC for the unconstrained case, and determine which constraint is most violated
- Set the corresponding current to its maximum value and run cPFC again, looking for the next most violated constraint
- Set the current for this constraint to its maximum value, run cPFC with these two constraints and repeat the procedure until no more constraints are violated.

This method avoids the problem of an inactive constraint locking the corresponding current to its initial value, thereby making it possible to find the “best” or near “best” set of currents to support a given equilibrium. Applying this technique to the tests performed in the previous section, the user would have stopped after the case with two active constraints. Recall that this case had a field error (1.822 %) very close to the field error of the unconstrained case (1.408 %). It should be noted that if too many of the constraints are violated by a large margin, even the optimum set of coil currents will not represent a good solution, since the field error will be much larger than desired.

Finally, some mention should be made of the execution times required to obtain these results. The unconstrained case required 0.6084 CPU seconds on a Cray-2 to estimate the currents, and needed a total of 11.07 CPU seconds to run. For the case of two active and two inactive constraints (the final case in the previous section), estimating the currents use 0.6854 CPU seconds and a total of 10.99 CPU seconds to run. These results indicate that the implementation of the linear constraint algorithm does not appreciably increase the total amount of CPU time required to run the program.

Chapter 5

Forces on PF Coils

The next set of constraints to be imposed on the coil currents arise from the forces acting on the coils. In this chapter, the equations used to calculate those forces are derived. This force model will be used in the next chapter to compute the coil currents such that the coil force limits are not exceeded.

The coil-coil interaction forces are derived over the next four sections. These forces are computed from the potential energy of a set of coils. The potential energy, in turn, is computed from the vector potential, which is the subject of the next section.

5.1 The Vector Potential

Maxwell's equation for the divergence of a magnetic field \mathbf{B} states

$$\nabla \cdot \mathbf{B} = 0$$

throughout all space. By making use of the property that

$$\nabla \cdot (\nabla \times \mathbf{A}) = 0$$

for any vector \mathbf{A} , the magnetic field may be expressed in terms of \mathbf{A} through the relation

$$\mathbf{B} = \nabla \times \mathbf{A}$$

With the magnetic field defined in this manner, \mathbf{A} is referred to as the *vector potential* of \mathbf{B} .

5.1.1 Vector Potential of a Distributed Current

From the Biot-Savart law, the vector potential describing a distributed current (carrying a current density \mathbf{J}) is given by

$$\mathbf{A}(\mathbf{r}) = \frac{\mu_0}{4\pi} \int_{V'} \frac{\mathbf{J}(\mathbf{r}')}{|\mathbf{r} - \mathbf{r}'|} d\tau$$

where V' is the volume containing the current \mathbf{J} . Although this expression appears quite straightforward, substantial manipulation of it is required to obtain a form appropriate to cylindrical systems. Now, consider the case of a coil with a rectangular cross-section (of width w , height h , major radius R , and elevation Z) carrying a uniform current density J . In this case, $\mathbf{J} = J\mathbf{e}_\phi$, and the vector potential is given by:

$$\mathbf{A}(\mathbf{r}) = \mathbf{e}_\phi \frac{\mu_0 J}{4\pi} \int_{Z-(h/2)}^{Z+(h/2)} \int_0^{2\pi} \int_{R-(w/2)}^{R+(w/2)} \frac{\cos(\phi' - \phi) r' dr' d\phi' dz'}{[r^2 + r'^2 - 2rr'\cos(\phi' - \phi) + (z - z')^2]^{1/2}} \quad (5.1)$$

where the direction of \mathbf{e}_ϕ is the \mathbf{e}_ϕ of the observation point.

With some work, it is possible to perform the integral in ϕ' . Making the transformation $\beta = \phi' - \phi$ gives

$$A_\phi = \frac{\mu_0 J}{4\pi} \int_{Z-(h/2)}^{Z+(h/2)} \int_{-\phi}^{2\pi-\phi} \int_{R-(w/2)}^{R+(w/2)} \frac{\cos(\beta) r' dr' d\beta dz'}{[r^2 + r'^2 - 2rr'\cos(\beta) + (z - z')^2]^{1/2}}$$

This integrand is cyclic in β with a period of 2π , so the limits on the β integral can be rewritten as $(0, 2\pi)$, thereby removing all ϕ dependence from the vector potential. It is now possible to evaluate the β integral, resulting in [4]

$$\mathbf{A}(\mathbf{r}) = \mathbf{e}_\phi \frac{\mu_0 J}{4\pi} \int r' G(r, z; r', z') dr' dz' \quad (5.2)$$

where

$$G(r, z; r', z') = \frac{2A}{rr'} [(1 - k^2/2)K(k) - E(k)] \quad (5.3)$$

$$A^2 = (r + r')^2 + (z - z')^2 \quad (5.4)$$

$$k^2 = 4rr'/A^2 \quad (5.5)$$

where $K(k)$ and $E(k)$ are the complete elliptic integrals of the first and second kind, respectively.

5.1.2 Filamentary Currents

A current \mathbf{J} flowing in a very thin loop can be considered filamentary, so that

$$\mathbf{J}(\mathbf{r}) = I\delta(r' - R)\delta(z' - Z)\mathbf{e}_\phi$$

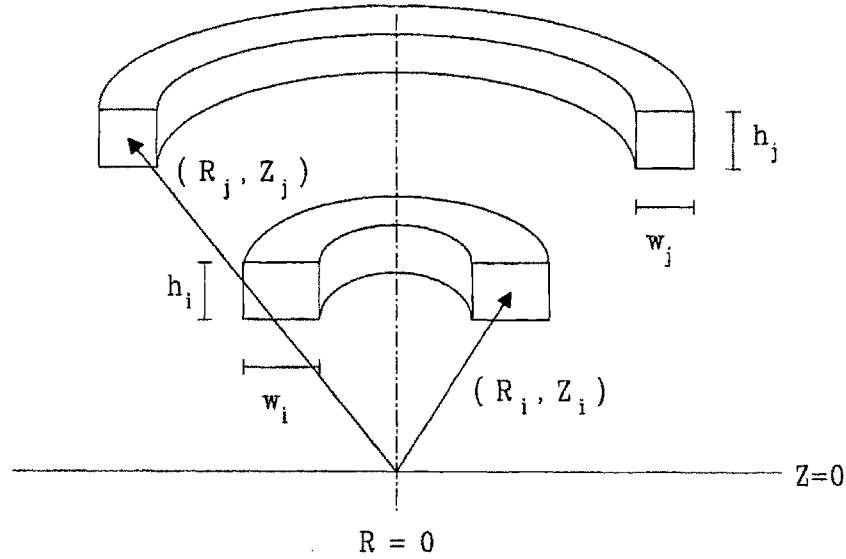


Figure 5-1: Simple coil model for computing the magnetic energy

where I is the total current flowing in the loop and δ is the Dirac delta function. Using this relation to derive an expression analogous to equation 5.2 results in

$$\mathbf{A}(\mathbf{r}) = \mathbf{e}_\phi \frac{\mu_0 I}{4\pi} RG(r, z; R, Z) \quad (5.6)$$

5.2 Magnetic Energy of a System of Currents

In this section, the energy of interaction between the coils producing a magnetic field and the currents flowing through those coils will be determined. As in the previous section, a general expression will be developed for distributed currents and a simplification for filamentary currents will follow.

5.2.1 Two Distributed Currents

Consider the set of coils shown in Figure 5-1. One coil has height h_i , radial width w_i , major radius R_i , and elevation given by Z_i . The characteristics of the other coil are denoted with a subscript j . The energy associated with the interaction of \mathbf{J}_i with the magnetic field produced

by \mathbf{J}_j is found from [25]

$$U_{j \rightarrow i} = \frac{1}{2} \int_V \mathbf{J}_i(\mathbf{r}) \cdot \mathbf{A}_j(\mathbf{r}) d\tau \quad (5.7)$$

where $\mathbf{A}_j(\mathbf{r})$ is the vector potential associated with \mathbf{J}_j and V is the volume encompassing \mathbf{J}_i .

5.2.2 A Single Distributed Current

In addition to interacting with the field produced by all other coils in a system, a current also interacts with its own magnetic field. For this case,

$$U_{i \rightarrow i} = \frac{1}{2} \int_V \mathbf{J}_i(\mathbf{r}) \cdot \mathbf{A}_i(\mathbf{r}) d\tau \quad (5.8)$$

5.2.3 Two Filamentary Currents

For the case of two filamentary currents, the substitution

$$\mathbf{J}_i(\mathbf{r}) = \mathbf{e}_\phi I_i \delta(r - R_i) \delta(z - Z_i)$$

is made in equation 5.7 and equation 5.6 is used for $\mathbf{A}_j(\mathbf{r})$. The resultant expression for the energy is

$$U_{j \rightarrow i} = \frac{\mu_0 I_i I_j}{4} R_i R_j G(R_i, Z_i; R_j, Z_j) \quad (5.9)$$

5.2.4 A Single Filamentary Current

Equation 5.9 describes the energy of a set of two filamentary currents. For the case of one filamentary current, this equation becomes infinite, a clearly unacceptable situation. A filamentary current results in $k = 1$ in Equation 5.5, and leads to a singularity in the elliptic integrals in Equation 5.3, making it impossible to find an analytic form for the vector potential of a single filament. A suitable approximation can, however, be found by assuming that the coil has a circular cross section and then taking the limit as k approaches 1. In this limit, the vector potential becomes [4]

$$A_{\phi i} = \frac{\mu_0 I_i R_i}{2\pi} \left[\ln\left(\frac{8R_i}{a}\right) - 2 \right]$$

where a is the equivalent radius of the coil, given by

$$a^2 = h_i w_i / \pi$$

The magnetic energy for this coil is given by

$$U_{i \rightarrow i} = \frac{\mu_0}{2} I_i^2 R_i \left[\ln\left(\frac{8R_i}{a}\right) - 2 \right] \quad (5.10)$$

It will be shown in a later section that approximating a rectangular coil as circular does not adversely affect the results.

5.3 Force Computations

Given expressions for the interaction energies of one and two coil systems, it is relatively simple to compute the force on a given coil. This is done by observing how the total energy of the system changes as the coils undergo an infinitesimal displacement from their starting positions. The net force acting on the system can then be written as

$$\mathbf{F} = -\nabla \sum_{i,j} U_{j \rightarrow i}$$

For a two coil system, the total energy is given by

$$\begin{aligned} U_t &= U_{i \rightarrow i} + U_{i \rightarrow j} + U_{j \rightarrow i} + U_{j \rightarrow j} \\ &= U_{i \rightarrow i} + 2U_{i \rightarrow j} + U_{j \rightarrow j} \end{aligned}$$

where use has been made of the relation $U_{i \rightarrow j} = U_{j \rightarrow i}$ as demonstrated in Appendix C.

To compute the force on coil i , the ∇ operator is replaced with ∇_i , which is defined as

$$\nabla_i = \mathbf{e}_R \frac{\partial}{\partial R_i} + \mathbf{e}_Z \frac{\partial}{\partial Z_i}$$

This operator perturbs the coil about its equilibrium position, giving \mathbf{F}_i .

As one coil of the two coil system is perturbed, the flux passing through both coils will, in general, change. Conservation of flux, however, requires that the flux passing through each coil remain constant. The next step of the derivation is to find a flux-conserving form for the force expression.

The inductance M of a coil can be expressed in terms of the energy,

$$M_{ij} = \frac{2U_{j \rightarrow i}}{I_i I_j}$$

With this equation, it is possible to express the flux through coil i due to coil j as

$$\phi_{j \rightarrow i} = M_{ij} I_j$$

and the total flux through each coil as

$$\begin{aligned}\Phi_i &= M_{ii}I_i + M_{ij}I_j \\ \Phi_j &= M_{ji}I_i + M_{jj}I_j = M_{ij}I_i + M_{jj}I_j\end{aligned}$$

where use has been made of the symmetry relation $M_{ij} = M_{ji}$ derived in Appendix C. The constant flux requirement then gives

$$\begin{aligned}\nabla_i \Phi_i &= M_{ii} \nabla_i I_i + I_i \nabla_i M_{ii} + M_{ij} \nabla_i I_j + I_j \nabla_i M_{ij} = 0 \\ \nabla_i \Phi_j &= M_{ij} \nabla_i I_i + I_i \nabla_i M_{ij} + M_{jj} \nabla_i I_j = 0\end{aligned}$$

where the M_{jj} term is completely independent of R_i and Z_i . The total energy can be expressed in terms of the fluxes as

$$U_t = \frac{1}{2} (\Phi_i I_i + \Phi_j I_j)$$

Taking the local gradient (∇_i) of this expression and invoking the flux conservation requirement results in

$$\nabla_i U_t = -\frac{1}{2} I_i^2 \nabla_i M_{ii} - I_i I_j \nabla_i M_{ij}$$

The force on coil i is, in turn, given by

$$\mathbf{F}_i = -(\nabla_i U_t)_\phi = \frac{1}{2} I_i^2 \nabla_i M_{ii} + I_i I_j \nabla_i M_{ij}$$

where the subscript ϕ indicates that the energy gradient has been computed with respect to the constant flux requirement. This expression can now be generalized to an N coil system, giving

$$\mathbf{F}_i = I_i^2 \nabla_i \left(\frac{U_{i \rightarrow i}}{I_i^2} \right) + I_i \sum_{j=1, j \neq i}^N 2I_j \nabla_i \left(\frac{U_{j \rightarrow i}}{I_i I_j} \right)$$

Note that in the previous expression, all of the energy terms are independent of the currents I_i and I_j . Given this expression for the forces, it is only a matter of performing some straightforward algebra¹ to obtain the net force acting on a given coil.

5.3.1 Force Between Two Distributed Currents

The force on a current \mathbf{J}_i due to a current \mathbf{J}_j is computed from

$$\begin{aligned}\mathbf{F}_{j \rightarrow i} &= \mathbf{e}_R \frac{1}{2} \frac{\partial}{\partial R_i} \int_V \mathbf{J}_i(\mathbf{r}) \cdot \mathbf{A}_j(\mathbf{r}) d\tau \\ &+ \mathbf{e}_Z \frac{1}{2} \frac{\partial}{\partial Z_i} \int_V \mathbf{J}_i(\mathbf{r}) \cdot \mathbf{A}_j(\mathbf{r}) d\tau\end{aligned}$$

¹See Appendix D for the full set of derivations.

Since the derivatives do not involve variables of integration, it is possible to evaluate this expression directly. The result found in equation D.4 is

$$\begin{aligned}
 \mathbf{F}_{j \rightarrow i} = & \mathbf{e}_R \frac{\mu_0 J_i J_j}{4} \int_{Z_i - \frac{h_i}{2}}^{Z_i + \frac{h_i}{2}} \int_{Z_j - \frac{h_j}{2}}^{Z_j + \frac{h_j}{2}} \int_{R_j - \frac{w_j}{2}}^{R_j + \frac{w_j}{2}} (R_i + \frac{w_i}{2}) r' G(R_i + \frac{w_i}{2}, z; r', z') dr' dz' dz \\
 & - \mathbf{e}_R \frac{\mu_0 J_i J_j}{4} \int_{Z_i - \frac{h_i}{2}}^{Z_i + \frac{h_i}{2}} \int_{Z_j - \frac{h_j}{2}}^{Z_j + \frac{h_j}{2}} \int_{R_j - \frac{w_j}{2}}^{R_j + \frac{w_j}{2}} (R_i - \frac{w_i}{2}) r' G(R_i - \frac{w_i}{2}, z; r', z') dr' dz' dz \\
 & + \mathbf{e}_Z \frac{\mu_0 J_i J_j}{4} \int_{R_i - \frac{w_i}{2}}^{R_i + \frac{w_i}{2}} \int_{Z_j - \frac{h_j}{2}}^{Z_j + \frac{h_j}{2}} \int_{R_j - \frac{w_j}{2}}^{R_j + \frac{w_j}{2}} r r' G(r, Z_i + \frac{h_i}{2}; r', z') dr' dz' dr \\
 & - \mathbf{e}_Z \frac{\mu_0 J_i J_j}{4} \int_{R_i - \frac{w_i}{2}}^{R_i + \frac{w_i}{2}} \int_{Z_j - \frac{h_j}{2}}^{Z_j + \frac{h_j}{2}} \int_{R_j - \frac{w_j}{2}}^{R_j + \frac{w_j}{2}} r r' G(r, Z_i - \frac{h_i}{2}; r', z') dr' dz' dr
 \end{aligned}$$

5.3.2 Self Force of a Distributed Current

Computation of a distributed current's self force is comparatively simple. Due to symmetry, the \mathbf{e}_Z component is zero. Taking the gradient of equation 5.8 results in equation D.5

$$\begin{aligned}
 \mathbf{F}_{i \rightarrow i} = & \frac{\mu_0 J_i^2}{2} \int_{Z_i - \frac{w_i}{2}}^{Z_i + \frac{w_i}{2}} \int_{Z_i - \frac{h_i}{2}}^{Z_i + \frac{h_i}{2}} \int_{R_i - \frac{w_i}{2}}^{R_i + \frac{w_i}{2}} (R_i + \frac{w_i}{2}) r' G(R_i + \frac{w_i}{2}, z; r', z') dr' dz' dz \\
 & - \frac{\mu_0 J_i^2}{2} \int_{Z_i - \frac{w_i}{2}}^{Z_i + \frac{w_i}{2}} \int_{Z_i - \frac{h_i}{2}}^{Z_i + \frac{h_i}{2}} \int_{R_i - \frac{w_i}{2}}^{R_i + \frac{w_i}{2}} (R_i - \frac{w_i}{2}) r' G(R_i - \frac{w_i}{2}, z; r', z') dr' dz' dz
 \end{aligned}$$

5.3.3 Force Between Two Filamentary Currents

The magnetic energy of two filamentary currents is given by equation 5.9. The corresponding expression for the force is given by equation D.1:

$$\begin{aligned}
 \mathbf{F}_{j \rightarrow i} = & \frac{\mu_0 I_i I_j}{2} \frac{R_i + R_j}{A} \left\{ K(k) \left[\frac{R_i}{R_i + R_j} \right] + \frac{E(k)}{1 - k^2} \left[\frac{k^2}{2} - \frac{R_i}{R_i + R_j} \right] \right\} \mathbf{e}_R \\
 & + \frac{\mu_0 I_i I_j}{2} \frac{Z_i - Z_j}{A} \left\{ K(k) - E(k) \left(1 + \frac{k^2}{2(1 - k^2)} \right) \right\} \mathbf{e}_Z
 \end{aligned}$$

5.3.4 Self Force of a Filamentary Current

As in the case of a distributed current, the \mathbf{e}_Z component of the force is zero due to symmetry. The gradient of the energy can then be directly computed, resulting in equation D.2

$$\mathbf{F}_{i \rightarrow i} = \frac{\mu_0}{2} I_i^2 \left[\ln \left(\frac{8R_i}{a} \right) - 1 \right] \mathbf{e}_R$$

5.4 Modelling the Coil-Coil Forces

The three previous sections developed two possible sets of equations for use in computing the coil-coil interaction forces. This section is concerned with finding the best combination of these expressions to use in the final form of the force model. The selection process will concentrate on the computational speed with which the forces can be computed and the overall accuracy of those forces. The first step in this process is to compare the results of the distributed and filamentary force equations.

Reconsider the two coil system shown in Figure 5-1. The first comparison consists of giving both coils the same major radius ($R_0 = 0.500$ m) and the same height and width ($h = 0.050$ m, $w = 0.050$ m). Coil one is positioned at $Z_1 = 0.000$ and coil two is moved from $Z_2 = -1.000$ m to $Z_2 = 1.000$ m. In the region where coil two would intersect coil one ($-0.050 \text{ m} \leq Z_2 \leq 0.050 \text{ m}$), the only point computed is $Z_2 = Z_1 = 0$, which corresponds to the self-force of coil one.

Defining the force coefficient, f_{21} , as

$$f_{21} = F_{2 \rightarrow 1} / \mu_0 I_1 I_2 \quad (5.11)$$

makes it possible to directly compare the results of the filamentary and distributed force models. The radial components of the force coefficient are compared in Figure 5-2, and the axial components of the force coefficient are compared in Figure 5-3. These two figures show that, for this case, the filamentary and distributed models are quite comparable.

An estimate of how well the distributed and filamentary current models agree can be obtained from the relative difference between them. This difference is defined as

$$d_r = \frac{f_f - f_d}{f_f}$$

where f_f is the force coefficient of the filamentary model and f_d is the coefficient found with the distributed current model. The relative differences of the radial and axial components of the force coefficients are presented in Figures 5-4 and 5-5, respectively.

Figure 5-4 shows a sharp minimum at $Z_2 = 0$, illustrating the difference between the filamentary and distributed current self-forces. That the relative difference for this case is negative simply means that the self-force computed with the distributed current model is larger than the self-force from the filamentary model. The relative difference for the remainder of the Z_2 values

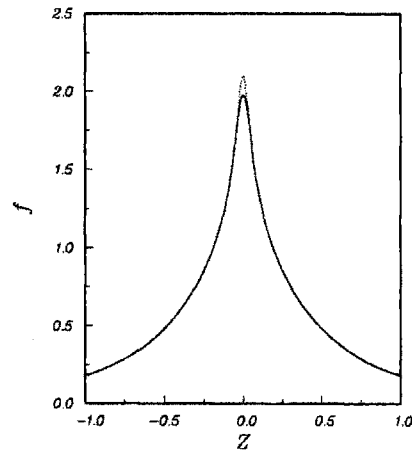


Figure 5-2: Comparison of the radial components of the force coefficient for an axially displaced coil. The solid line is the force coefficient found from the filamentary model. The dotted line represents the force coefficient computed from the distributed current model.

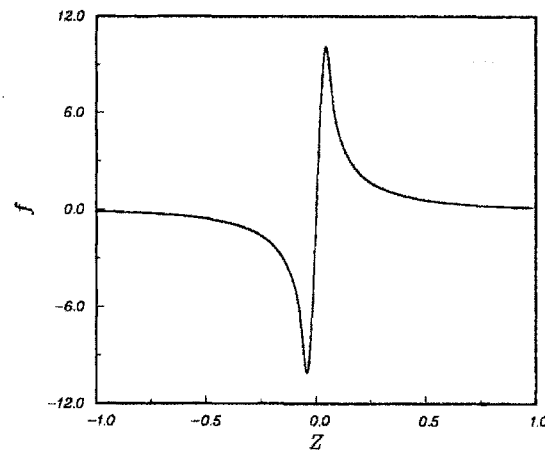


Figure 5-3: Comparison of the axial components of the force coefficient for an axially displaced coil. The solid line in this figure is the force coefficient computed using the filamentary current model. The indistinguishable dotted line is the coefficient found from the distributed current model.

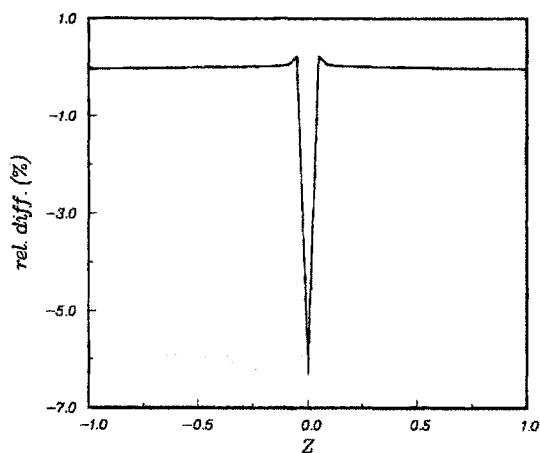


Figure 5-4: Relative difference between the radial force coefficients for the case of an axially displaced coil.

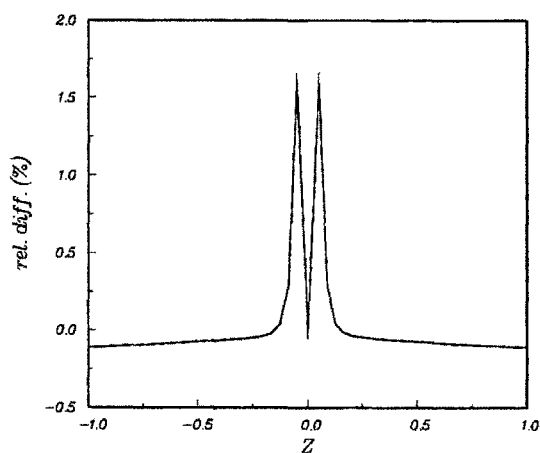


Figure 5-5: Relative difference between the axial force coefficients for the case of an axially displaced coil.

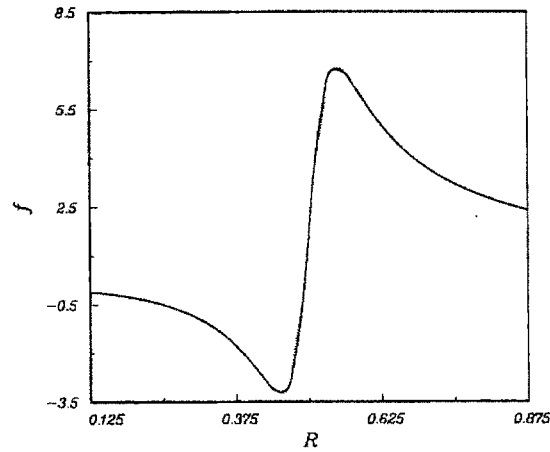


Figure 5-6: Comparison of the radial components of the force coefficient for the case of a coil with a varying radius. The solid line is the force coefficient found from the filamentary model. The dotted line represents the force coefficient computed from the distributed current model.

is very nearly zero, indicating that, except for the self-force, there is practically no difference between the force coefficients found with the two models.

Examining Figure 5-5 shows similar behavior. Since the axial component of the self-force has been set to zero by symmetry, the relative difference at $Z_2 = 0$ is zero. The remainder of the figure shows a very small relative difference except when the coils are very close together. In the region very near coil one, the magnetic field is decreasing very rapidly (recall that a dipole field falls off as $1/R^2$ near the dipole). The filamentary current model is sampling this field at one specific point while the distributed current is sampling the field over its entire cross-section, leading to a smaller force coefficient for the distributed current model.

The next comparison to be made fixes Z_2 at a position of 0.050 m while the major radius varies in the range $0.25R_1 \leq R_2 \leq 1.75R_1$. The radial component of the force coefficient for this case is shown in Figure 5-6 and the axial component is shown in Figure 5-7. These two figures show that both the qualitative and quantitative behavior of the filamentary and distributed current force models agree quite well for this case.

The radial component of the relative difference for this case is shown in Figure 5-8. This figure shows two spikes near the position $R_2 = R_1$. These spikes are again due to the overestimate

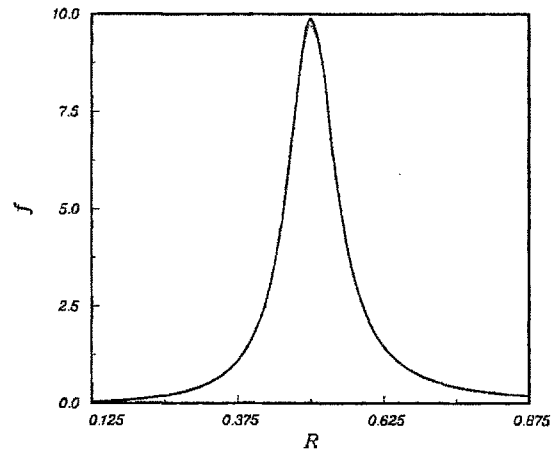


Figure 5-7: Comparison of the axial components of the force coefficient for the case of a coil with a varying radius. The solid line is the force coefficient found from the filamentary model. The dotted line represents the force coefficient computed from the distributed current model.

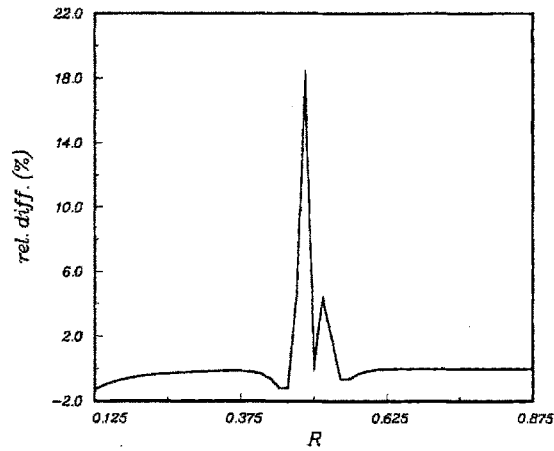


Figure 5-8: Radial component of the relative difference for a coil with a varying radius

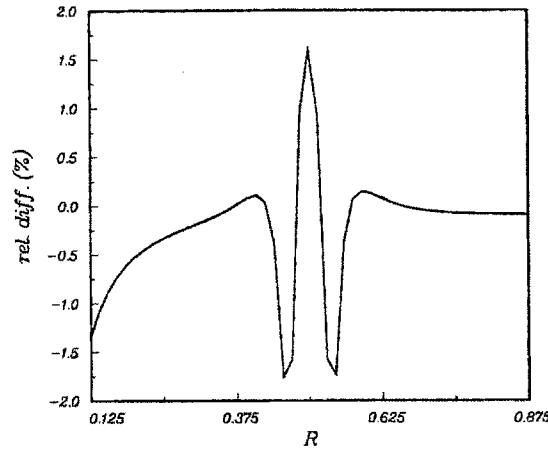


Figure 5-9: Axial component of the relative difference for a coil with a varying radius

of the force obtained from the filamentary model. The small value of the difference at $R_2 = R_1$ is due to the negligible axial component of the magnetic field which occurs when coil two is positioned directly above coil one.

The axial component of the relative difference is shown in Figure 5-9. This figure again shows a large positive spike at $R_2 = R_1$, indicating that the axial component of the force is being overestimated by the filamentary model. The smaller negative spikes on either side of $R_2 = R_1$ show that the filamentary model underestimates the force in that region, again due to the fact that the filament is sampling only one point of the field while the distributed current is sampling the field over its cross-section.

The worst case results obtained from these two tests occur when the coils are very close together. In general, this situation occurs when there are a number of coils (wires) grouped together into a larger coil in which each of the wires carries the same current. The force interactions between the wires making up a single coil can, however, be ignored, since these forces are internal to the coil. Computation of the coil's self-force is performed by simply summing the self-forces of the wires making up the coil.

Since the two models produce nearly the same results, either of them would be suitable for estimating the coil-coil interaction forces. The next step is to estimate the amount of computation necessary to calculate the forces. The integrations required by the distributed current model were performed using the eight point Gaussian quadrature scheme presented in Appendix E. Thus,

each integral required calculating the integrand 512 times. To calculate the force between two coils required evaluating the integrand 2048 times, and determining the self-force requires an additional 1024 evaluations. Calculation of force between two coils using the filamentary model is done in only 2 functional evaluations, and the self-force is found from 1 additional evaluation.

For an N wire system, the total number of coil-coil forces that must be calculated is given by $(N^2 - N)/2$. For the Alcator C-Mod coil set presented in the previous chapter, this number is 55,945. Using the distributed current model to compute all of these forces would be computationally prohibitive (over 100 CPU minutes on a Cray 2). For this reason, the filamentary model is used to compute all of the wire-wire interaction forces. Since only N self-forces have to be computed, the user of the cPFC program is given the option to use either model, although the distributed current model is more accurate for this case.

5.5 Plasma-Coil Interaction Forces

In the previous sections, the forces due to coil-coil interactions were derived and calculated. This section is concerned with the calculation of the forces acting on the coils due to the plasma itself. The calculation itself uses a variation of the Green's function methodology presented in Chapter 2.

The force on a given coil due to the plasma can be found from

$$\mathbf{F}_{p \rightarrow i} = \int_{V_i} \mathbf{J}_i \times \mathbf{B}_p d\tau \quad (5.12)$$

where \mathbf{J}_i is the current flowing in the i th conductor, \mathbf{B}_p is the plasma magnetic field in the vacuum region, and V_i is the volume of the i th conductor. Since the coils are considered to be far from the plasma (relative to the coil dimensions), \mathbf{J}_i can be represented as a filamentary current:

$$\mathbf{J}_i = I_i \delta(r - R_i) \delta(z - Z_i) \mathbf{e}_\phi \quad (5.13)$$

where I_i is the magnitude of the current flowing in coil i . By substituting equation 5.13 into equation 5.12 and invoking the toroidal symmetry assumption, $\mathbf{F}_{p \rightarrow i}$ becomes:

$$\mathbf{F}_{p \rightarrow i} = 2\pi I_i (\mathbf{e}_\phi \times \mathbf{B}_p(R_i, Z_i)) \quad (5.14)$$

As discussed in Chapter 2, the vacuum magnetic field due to the plasma can be represented as

$$\mathbf{B}_p = \nabla \phi + \mathbf{B}_i$$

where ϕ is the scalar magnetic potential of the plasma and \mathbf{B}_i is the field due to a single filament assumed to carry all of the plasma current and located at the plasma magnetic axis. Substituting this into equation 5.14 results in

$$\mathbf{F}_{p \rightarrow i} = 2\pi I_i (\mathbf{e}_\phi \times \nabla \phi + \mathbf{e}_\phi \times \mathbf{B}_i) \quad (5.15)$$

The last expression on the right hand side of equation 5.15 is simply the force between two filamentary coils. It is possible to replace that component of equation 5.15 with the equivalent expression formulated using the potential energy techniques described earlier in this chapter. Denoting this component as $\mathbf{F}_{pf \rightarrow i}$, equation 5.15 becomes

$$\mathbf{F}_{p \rightarrow i} = 2\pi I_i (\mathbf{e}_\phi \times \nabla \phi) + \mathbf{F}_{pf \rightarrow i} \quad (5.16)$$

where

$$\begin{aligned} \mathbf{F}_{pf \rightarrow i} = & \frac{\mu_0 I_i I_p}{2} \frac{R_i + R_m}{A} \left\{ K(k) \left[\frac{R_i}{R_i + R_m} \right] + \frac{E(k)}{1 - k^2} \left[\frac{k^2}{2} - \frac{R_i}{R_i + R_m} \right] \right\} \mathbf{e}_R \\ & + \frac{\mu_0 I_i I_p}{2} \frac{Z_i - Z_m}{A} \left\{ K(k) - E(k) \left(1 + \frac{k^2}{2(1 - k^2)} \right) \right\} \mathbf{e}_Z \end{aligned} \quad (5.17)$$

In equation 5.17, R_m and Z_m represent the coordinates of the magnetic axis of the plasma.

5.5.1 The Scalar Potential

With equations 5.16 and 5.17, it is only necessary to compute $\nabla \phi$ to determine the force due to the plasma. In Chapter 2, ϕ was found on the plasma surface using Green's theorem. Green's theorem can also be used to compute ϕ in the space surrounding the plasma. Recall from Chapter 2

$$\sigma \phi(\mathbf{r}) + \int_{S_p} \left[\phi(\mathbf{r}') (\mathbf{e}'_n \cdot \nabla' \hat{G}(\mathbf{r}, \mathbf{r}')) - \hat{G}(\mathbf{r}, \mathbf{r}') (\mathbf{e}'_n \cdot \nabla' \phi(\mathbf{r}')) \right] dS' = 0 \quad (5.18)$$

where \mathbf{r} refers to the observation point, \mathbf{r}' refers to the plasma surface, and the value of σ depends on the location of the observation point. For this case, the observation point is outside of the plasma surface, so $\sigma = 1$.

In Chapter 2, use was made of the toroidal symmetry assumption to simplify equation 5.18. As before, the primed variables denote the plasma surface, which is parameterized in terms of μ . Thus, equation 5.18 can be simplified to

$$\phi(r, z) + \int_0^{2\pi} \left[\phi(\mu') \frac{\partial G(r, z, \mu')}{\partial n'} - G(r, z, \mu') \frac{\partial \phi(\mu')}{\partial n'} \right] R' d\mu' = 0 \quad (5.19)$$

where G is the reduced Green's function given by

$$G = -\frac{kK(k)}{2\pi\sqrt{RR'}} \quad (5.20)$$

and k is again defined as

$$k^2 = \frac{4RR'}{(R+R')^2 + (Z-Z')^2} \quad (5.21)$$

The majority of Chapter 2 was concerned with finding $\phi(\mu')$ and $R'\partial\phi(\mu')/\partial n'$. With this information, it is a simple matter to evaluate equation 5.19 to find the scalar potential of the plasma at any point in space. It is also fairly easy to compute the gradient of equation 5.19, which is the goal of the next section.

5.5.2 Gradient of the Scalar Potential

It is a reasonably straightforward process to compute the gradient of equation 5.19. Noting that the gradient involves only the spatial variables r and z and not the surface variables $R_p(\mu')$ and $Z_p(\mu')$ results in

$$\nabla\phi(r, z) = \int_0^{2\pi} \left[(\nabla G(r, z, \mu')) \frac{\partial\phi(\mu')}{\partial n'} - \phi(\mu') \left(\nabla \frac{\partial G(r, z, \mu')}{\partial n'} \right) \right] R' d\mu' \quad (5.22)$$

The problem of computing $\nabla\phi$ has now been reduced to finding expressions for the gradients of G and $\partial G/\partial n'$, which is the subject of the next two subsections.

The Gradient of G

Computing the gradient of the reduced Green's function is fairly simple. Starting with the e_R component gives

$$\begin{aligned} \frac{\partial G}{\partial R} &= -\frac{kK(k)}{2\pi} \frac{\partial}{\partial R} \left(\frac{1}{\sqrt{RR_p}} \right) - \frac{1}{2\pi\sqrt{RR_p}} \frac{\partial}{\partial k} (kK(k)) \frac{\partial k}{\partial R} \\ &= \frac{kK(k)}{4\pi R\sqrt{RR_p}} - \frac{1}{2\pi\sqrt{RR_p}} \frac{E(k)}{1-k^2} \frac{\partial k}{\partial R} \end{aligned}$$

where use has been made of the identities in equation 2.33.

Using the definition of k gives

$$\frac{\partial k}{\partial R} = k \left(\frac{1}{2R} - \frac{R_p + R}{A^2} \right) \quad (5.23)$$

where

$$A^2 = (R_p + R)^2 + (Z_p - Z)^2$$

The net result of this derivation is

$$\frac{\partial G}{\partial R} = \frac{k}{4\pi R\sqrt{RR_p}} \left[K(k) - \frac{E(k)}{1-k^2} \left(1 - \frac{k^2}{2} \left(1 + \frac{R_p}{R} \right) \right) \right] \quad (5.24)$$

Determining the e_Z component is a little easier, since the only dependence on Z is in k .

Noting that

$$\frac{\partial k}{\partial Z} = \frac{k(Z_p - Z)}{A^2} \quad (5.25)$$

results in

$$\frac{\partial G}{\partial Z} = \frac{k}{4\pi R\sqrt{RR_p}} \left[\frac{E(k)}{1-k^2} \left(\frac{k^2}{2R_p} (Z - Z_p) \right) \right] \quad (5.26)$$

The Gradient of $\partial G/\partial n'$

The normal derivative of the reduced Green's function is given by

$$R' \frac{\partial G(R, Z, \mu)}{\partial n'} = \frac{1}{2\pi} \sqrt{\frac{R_p(\mu)}{R}} [\Lambda k E(k) + \Gamma k (K(k) - E(k))] \quad (5.27)$$

where

$$\Lambda = \frac{Z_{p\mu}(R_p(\mu) - R) - R_{p\mu}(Z_p(\mu) - Z)}{(R_p(\mu) - R)^2 + (Z_p(\mu) - Z)^2} \quad (5.28)$$

$$\Gamma = \frac{Z_{p\mu}}{2R_p(\mu)} \quad (5.29)$$

In the above relations,

$$Z_{p\mu} = \frac{\partial Z_p(\mu)}{\partial \mu} \quad (5.30)$$

$$R_{p\mu} = \frac{\partial R_p(\mu)}{\partial \mu} \quad (5.31)$$

Determining the gradient of the normal derivative of the reduced Green's function is more difficult due to the complexity of equation 5.27. Propagating the $\partial/\partial R$ operator through equation 5.27 results in

$$\begin{aligned} \frac{\partial}{\partial R} \left(R' \frac{\partial G}{\partial n'} \right) &= -\frac{1}{4\pi R} \sqrt{\frac{R_p}{R}} [\Lambda k E(k) + \Gamma k (K(k) - E(k))] \\ &\quad - 2RE(k) \left\{ k\Lambda_R + k_R \left((\Lambda - \Gamma) \left(2 - \frac{K(k)}{E(k)} \right) + \frac{\Gamma}{1-k^2} \right) \right\} \end{aligned} \quad (5.32)$$

where the derivative of Λ with respect to R is given by

$$\Lambda_R = \frac{Z_{p\mu} [(R_p - R)^2 - (Z_p - Z)^2] - 2R_{p\mu}(Z_p - Z)(R_p - R)}{[(R_p - R)^2 + (Z_p - Z)^2]^2}$$

and k_R is given by equation 5.23.

The e_Z component is found similarly, resulting in

$$\frac{\partial}{\partial Z} \left(R' \frac{\partial G}{\partial n'} \right) = \frac{E(k)}{2\pi} \sqrt{\frac{R_p}{R}} \left\{ k\Lambda_Z + k_Z \left((\Lambda - \Gamma)(2 - \frac{K(k)}{E(k)}) + \frac{\Gamma}{1 - k^2} \right) \right\} \quad (5.33)$$

where

$$\Lambda_Z = \frac{R_{p\mu} [(R_p - R)^2 - (Z_p - Z)^2] + 2Z_{p\mu}(Z_p - Z)(R_p - R)}{[(R_p - R)^2 + (Z_p - Z)^2]^2}$$

and k_Z is given by equation 5.25.

5.6 Plasma Force Equations

The various equations for the plasma-coil force components can now be combined to determine the total force due to the plasma. The radial component of the plasma force on a coil is found from

$$\begin{aligned} (\mathbf{F}_{p \rightarrow i})_R &= 2\pi I_i \frac{\partial \phi}{\partial Z} + \frac{\mu_0 I_i I_p}{2} \frac{R_i + R_m}{A} \\ &\times \left\{ K(k) \left[\frac{R_i}{R_i + R_m} \right] + \frac{E(k)}{1 - k^2} \left[\frac{k^2}{2} - \frac{R_i}{R_i + R_m} \right] \right\} \end{aligned} \quad (5.34)$$

while the axial component is given by

$$\begin{aligned} (\mathbf{F}_{p \rightarrow i})_Z &= -2\pi I_i \frac{\partial \phi}{\partial R} \\ &+ \frac{\mu_0 I_i I_p}{2} \frac{Z_i - Z_m}{A} \left\{ K(k) - E(k) \left(1 + \frac{k^2}{2(1 - k^2)} \right) \right\} \end{aligned} \quad (5.35)$$

The derivatives of ϕ used in the preceeding equations correspond to the appropriate component of Equation 5.22.

Combining the plasma-coil force expressions with those obtained for the coil-coil forces makes it possible to compute the total force acting on a coil. This, in turn, makes it possible to invoke force constraints on the coil currents in the same way that limits to the coil currents were invoked in Chapter 4. The details of implementing these constraints and the results are the subject of the next chapter.

Chapter 6

Nonlinear Constraints

In Chapter 5, the expressions needed to compute the forces on the poloidal field coils were developed. This chapter is concerned with the force constraints and presents the formulation used to determine the coil currents in the presence of these constraints. The resulting system is then tested. Since the methods used in this chapter to constrain the coil currents are identical to those used in Chapter 4, a demonstration of the system for a coil set with both current and force constraints is then given.

6.1 The Source of the Constraints

As discussed in the previous chapter, the coils experience a force given by $\mathbf{J} \times \mathbf{B}$. The engineering properties of the coil limit the amount of force it can carry.

Consider a single copper coil 1.0 cm wide in the radial direction, 1.0 cm in height, and with a major radius of 1.0 m. For the purposes of this discussion, this coil will be treated as a 1.0 cm slice of an infinitely long pressure vessel. This approximation is made to simplify the derivation of the maximum forces in the radial direction. The maximum force the coil can carry in the radially outward direction is determined from

$$S = \frac{pr}{t}$$

where p is the internal pressure acting on the coil, r is the major radius of the coil, t is the (radial) thickness of the coil, and S is the tensile stress in the coil. To determine the maximum pressure this coil can carry, the tensile stress is replaced by the yield strength of the coil material. For annealed copper, the yield strength is 5000 psi. For the coil described above, the maximum

internal pressure is 50 psi, corresponding to a maximum force of 10.83 kN acting on the coil in the radially outward direction.

When a thin walled cylinder is subjected to a radially inward force the cylinder can fail by collapsing. The collapsing pressure is given by [1]

$$p_c = KE \left(\frac{t}{2r} \right)^3$$

where E is the Young's modulus of the coil material and K is a numerical coefficient. Assuming that the coil is a section of an infinitely long cylinder allows K to be approximated from

$$K = \frac{2}{1 - \mu^2}$$

where μ is Poisson's ratio for the material. Poisson's ratio for copper is 0.355 and Young's modulus is $15.6 \cdot 10^6$ psi. These values result in a collapsing pressure of 35.169 psi, so that the maximum allowable force in the radially inward direction for this coil is 7.62 kN.

Because the radially inward and outward force limits may be different, the force constraints in the radial direction are written in the form

$$\mathbf{F}_{Ri} \leq \mathbf{F}_R \leq \mathbf{F}_{Ro}$$

where \mathbf{F}_R is the vector of coil forces, \mathbf{F}_{Ri} is the vector of radially inward force limits, and \mathbf{F}_{Ro} corresponds to the radially outward force limits. Each of these vectors has a length of J , where J is the total number of coils in the system.

The forces in the axial direction are assumed to be limited by the force that the coil supports can withstand. Denoting these axial force limits as F_{Zm} , the allowable force in the axial direction is specified by

$$-F_{Zm} \leq F_Z \leq F_{Zm}$$

where F_Z is the vector of coil forces in the axial direction. Again, these vectors are all of length J .

6.2 Formulation of the Constraint Equations

The force expressions derived in Chapter 5 can be cast into two sets of linear equations with the form

$$\mathbf{F}_R = \mathbf{I}_i \cdot (\mathbf{P}_R \cdot \mathbf{i} + \mathbf{Q}_R) \quad (6.1)$$

$$\mathbf{F}_Z = \mathbf{I}_i \cdot (\mathbf{P}_Z \cdot \mathbf{i} + \mathbf{Q}_Z) \quad (6.2)$$

where \mathbf{F}_R and \mathbf{F}_Z are vectors of length J representing the radial and axial components of the coil forces. \mathbf{P}_R and \mathbf{P}_Z represent the intercoil forces in the radial and axial directions, as given by

$$\mathbf{P}_R = \begin{bmatrix} R_{11} & R_{12} & \cdots & \cdots & R_{1n} \\ R_{21} & R_{22} & R_{23} & \cdots & R_{2n} \\ \vdots & R_{32} & & & \vdots \\ \vdots & \vdots & & & \vdots \\ R_{n1} & R_{n2} & \cdots & \cdots & R_{nn} \end{bmatrix} \quad \mathbf{P}_Z = \begin{bmatrix} 0 & Z_{12} & \cdots & \cdots & Z_{1n} \\ Z_{21} & 0 & Z_{23} & \cdots & Z_{2n} \\ \vdots & Z_{32} & & & \vdots \\ \vdots & \vdots & & & \vdots \\ Z_{n1} & Z_{n2} & \cdots & \cdots & 0 \end{bmatrix}$$

where the R_{ij} and Z_{ij} are given by

$$R_{ij} = \frac{\partial}{\partial R_i} \left(\frac{U_{j \rightarrow i}}{I_i I_j} \right)$$

$$Z_{ij} = \frac{\partial}{\partial Z_i} \left(\frac{U_{j \rightarrow i}}{I_i I_j} \right)$$

as found in Chapter 5. The \mathbf{Q}_R and \mathbf{Q}_Z vectors represent the radial and axial components of the sum of the forces due to any fixed coil currents and the plasma. Finally, the matrix of grouped currents \mathbf{I}_i is defined as

$$\mathbf{I}_i = \begin{bmatrix} i_1 & 0 & \cdots & \cdots & 0 \\ 0 & i_2 & 0 & \cdots & 0 \\ \vdots & 0 & & & \vdots \\ \vdots & \vdots & & & \vdots \\ 0 & 0 & \cdots & \cdots & i_n \end{bmatrix}$$

Thus, the radial force on the j th coil carrying the n th grouped current is given by

$$\mathbf{F}_{Rj} = i_n \left(\sum_{k=1}^N \mathbf{P}_{Rj,k} i_k + \mathbf{Q}_{Rj} \right) \quad (6.3)$$

where N is the total number of grouped currents in the coil set.

Algebraically, the problem of minimizing the coil currents such that the force constraints are satisfied is expressed as

$$\begin{aligned} &\text{Minimize} && \mathbf{i}^T \cdot \mathbf{M} \cdot \mathbf{i} - 2\mathbf{n}^T \cdot \mathbf{i} + p \\ &\text{Subject to} && \mathbf{F}_{Ri} \leq \mathbf{F}_R(\mathbf{i}) \leq \mathbf{F}_{Ro} \\ &&& -\mathbf{F}_{Zm} \leq \mathbf{F}_Z(\mathbf{i}) \leq \mathbf{F}_{Zm} \end{aligned} \quad (6.4)$$

The nonlinear nature of the force equations makes this a very difficult problem to solve. As in Chapter 4, it is assumed that a feasible point of Equation 6.4 is a satisfactory solution.

The method used to find a feasible point for the force constraint problem is identical to that presented in Sections 4.3 and 4.5 for the linearly constrained problem. Equation 6.4 is first replaced by the auxiliary function

$$2\gamma(\mathbf{i}) = \mathbf{i}^T \cdot \mathbf{M} \cdot \mathbf{i} - 2\mathbf{n}^T \cdot \mathbf{i} + p + \alpha^T \cdot \mathbf{q} + \beta^T \cdot \mathbf{r} \quad (6.5)$$

where α and β are vectors of Lagrange multipliers and \mathbf{q} and \mathbf{r} are vectors corresponding to the constraint equations:

$$q_n = \begin{cases} \mathbf{F}_{R_n} - \mathbf{F}_{R_{in}} & \text{if } \mathbf{F}_{R_n} < 0 \\ \mathbf{F}_{R_n} - \mathbf{F}_{R_{on}} & \text{if } \mathbf{F}_{R_n} > 0 \end{cases} \quad (6.6)$$

$$r_n = \mathbf{F}_{Z_n} - \mathbf{F}_{Z_{m_n}} \quad (6.7)$$

Equation 6.5 can now be minimized. This is done by setting its derivative with respect to the grouped currents \mathbf{i} to zero. Formally, this results in

$$\frac{\partial \gamma(\mathbf{i})}{\partial \mathbf{i}} = \mathbf{M} \cdot \mathbf{i} - \mathbf{n} + \frac{\alpha^T}{2} \cdot \frac{\partial \mathbf{q}(\mathbf{i})}{\partial \mathbf{i}} + \frac{\beta^T}{2} \cdot \frac{\partial \mathbf{r}(\mathbf{i})}{\partial \mathbf{i}} = 0 \quad (6.8)$$

To simplify matters, consider the equation for the n th current group with only one coil (coil j) being constrained:

$$\frac{\partial \gamma(\mathbf{i})}{\partial i_n} = \sum_{k=0}^N M_{k,n} i_k - n_n + \frac{\alpha}{2} \frac{\partial q_j(\mathbf{i})}{\partial i_n} + \frac{\beta}{2} \frac{\partial r_j(\mathbf{i})}{\partial i_n} = 0 \quad (6.9)$$

Using the general form of the constraint equations given in Equation 6.3, the derivatives of \mathbf{q} and \mathbf{r} with respect to i_n are given by

$$\frac{\partial q_j(\mathbf{i})}{\partial i_n} = \frac{\partial i_j}{\partial i_n} \left(\sum_{k=1}^N \mathbf{P}_{R,j,k} i_k + \mathbf{Q}_{R,j} \right) + i_j \mathbf{P}_{R,j,n} \quad (6.10)$$

$$\frac{\partial r_j(\mathbf{i})}{\partial i_n} = \frac{\partial i_j}{\partial i_n} \left(\sum_{k=1}^N \mathbf{P}_{Z,j,k} i_k + \mathbf{Q}_{Z,j} \right) + i_j \mathbf{P}_{Z,j,n} \quad (6.11)$$

For the case of N grouped currents with K force constraints, Equation 6.8 has dimensions N by $N + 2K$. The remaining $2K$ equations needed to complete the system are simply the force constraint equations given by Equations 6.6 and 6.7. The resulting $N + 2K$ by $N + 2K$ system can then be solved using the algorithm presented in Section 4.5.

Computing the Jacobian of this system is a much more involved process, simply because of the nonlinearity of the force expressions. Additionally, the iterative nature of the algorithm requires that, after each iteration, the forces and the Jacobian be recomputed. The result is a computationally intensive algorithm for finding a feasible point of the system.

6.3 Verification, Validation, and Testing

As with the linear constraint algorithm in Chapter 4, the force constraint algorithm is invoked only if the constraints are specified by the user. Verification of the program for this case requires ensuring that the results obtained for the cases presented in Section 3.3, Appendix A, and Section 4.6 are identical to the results obtained using the force constraint version of cPFC. These results were reproduced, indicating that the force constraint algorithm has no adverse effects on the results of the previous versions of the cPFC program.

Validation and testing the force constraint system requires running a number of cases with varying numbers of constraints and examining the results. Additionally, one case will be run using several values of the maximum force to illustrate the behavior of the system as the constraints become more restrictive. These tests will be run on the equilibrium and coil set shown in Figure 6-1. This coil set and equilibrium are identical to those used in Chapter 4. The wires making up the various coils are listed in Appendix B, and the OH1, EFCU, and EFCL coils are carrying fixed total currents of 1.4964 MA, 3.0000 kA, and -3.0000 kA, respectively. The equilibrium parameters are listed in Table 6.1, and the unconstrained field and the equilibrium poloidal field are shown in Figure 6-2. The field error for the unconstrained case is 1.408346 %. Finally, the coil forces and currents are listed in Table 6.2.

The first test case involves constraining the forces on the EF2L coil. For this case, the maximum force in the radially outward direction is set to 41.00 kN, and the maximum force in the axial direction is limited to 18.50 kN. Both of these constraints are violated by the unconstrained coil currents. The tangential component of the poloidal field produced by the coils and plasma is compared with that of the plasma itself in Figure 6-3. The field error for this case is 1.408669 %, and the coil forces and currents are listed in Table 6.3. The very small difference between the field error for this case and the unconstrained case is due to the very slight amount by which the constraints are violated. Because the difference between this field error and the field error for the unconstrained case is so slight, there is no perceivable difference between the poloidal

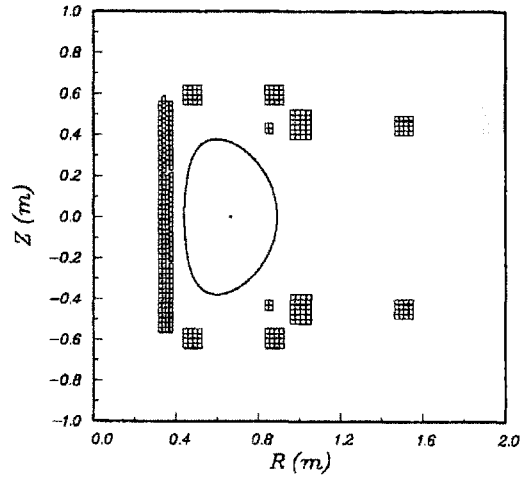


Figure 6-1: Alcator C-Mod coil set and equilibrium used for testing the force constraint algorithm

Table 6.1: Equilibrium data for the Alcator C-Mod test case.

<i>Parameter</i>	<i>Value</i>
R_0 (m)	0.665
a (m)	0.225
δ	0.310
κ	1.680
B_0 (T)	8.500
I_p (MA)	2.500
β_p	0.500
β_t (%)	0.017

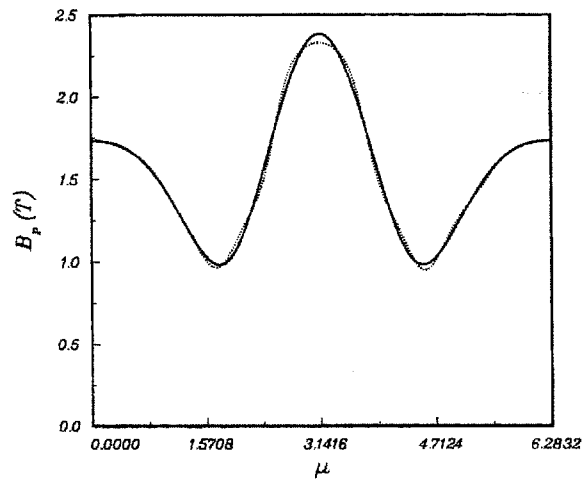


Figure 6-2: Poloidal fields for the unconstrained case. The solid line is the equilibrium field of the plasma. The dotted line represents the field due to the plasma and the PF coils.

Table 6.2: Unconstrained coil forces and currents.

Coil Label	Radial Force (MN)	Axial Force (MN)	Current (kA)
OH1	10.509	-0.014	11.600
OH2U	3.438	-0.774	30.885
OH2L	3.398	0.906	30.186
EF1U	0.496	-2.413	51.274
EF1L	0.434	2.572	54.836
EF2U	-0.456	-0.161	6.618
EF2L	0.041	-0.019	-0.589
EF3U	0.642	0.185	-4.450
EF3L	0.646	-0.242	-4.450
EFCU	0.150	0.082	7.500
EFCL	-0.150	0.095	-7.500
EF4U	2.715	0.669	-54.720
EF4L	2.668	-0.726	-54.720

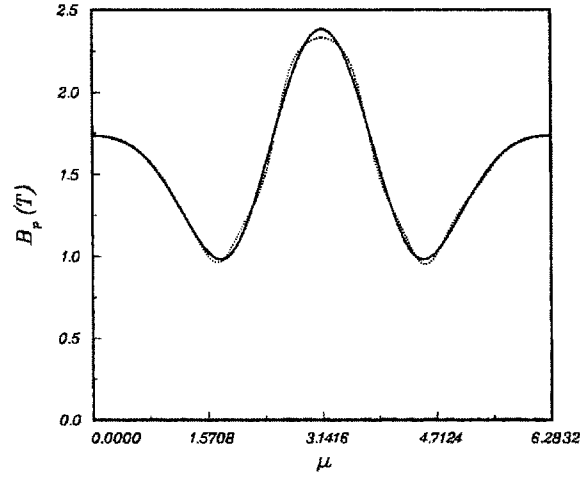


Figure 6-3: Poloidal fields for the case of one force constraint. The solid line is the equilibrium field of the plasma, and the dotted line shows the field from the combination of the plasma and the PF coils.

Table 6.3: Coil forces and currents for the case of one coil with a force constraint.

Coil Label	Radial Force (MN)	Axial Force (MN)	Current (kA)
OH1	10.364	-0.015	11.600
OH2U	3.537	-0.741	30.891
OH2L	3.496	0.877	30.211
EF1U	0.537	-2.457	51.294
EF1L	0.478	2.616	54.777
EF2U	-0.456	-0.162	6.573
EF2L	0.041	-0.018	-0.579
EF3U	0.638	0.180	-4.394
EF3L	0.642	-0.236	-4.394
EFCU	0.152	0.082	7.500
EFCL	-0.152	0.095	-7.500
EF4U	2.722	0.665	-54.796
EF4L	2.676	-0.722	-54.796

fields shown in Figure 6-3 for the constrained case and the fields shown in Figure 6-2 for the unconstrained case.

The next case uses two active constraints. The force constraint on the EF2L coil is kept, and the EF2U coil is also constrained. The unconstrained radial force on the EF2U coil is directed inward, so these two constraints make it possible to test the full functionality of the algorithm. The maximum force in the radial direction is set to 0.45 MN, and the axial force is limited to 0.20 MN. Figure 6-4 compares the resulting poloidal field with that of the equilibrium alone. The coil forces and currents produced for this test are given in Table 6.4. Again, the very small amount by which the constraints are violated gives rise to a reasonably small field error, in this case 1.556010 %.

The third case tests the system for a constraint which is inactive. This is done by retaining the previous constraints and setting the maximum radial force on the EF1U coil to 5.00 MN both inward and outward, and setting the maximum axial force to 5.00 MN. This constraint is clearly satisfied by the all three of the cases presented thus far. The equilibrium field is compared with the poloidal field generated by the plasma and coil set in Figure 6-5, and the coil forces and currents are listed in Table 6.5. The field error for this case is somewhat larger than for the previous cases at 1.663022 %.

The final test for this case adds another inactive constraint to the three constraints already imposed on the system. For this test, the forces on the EF1L coil are limited to 5.0000 MN for both the inward and outward radial force and 5.0000 MN in the axial direction. These constraints are inactive for all of the tests performed so far. The coil forces and currents are listed in Table 6.6 and the tangential components of the equilibrium field and the poloidal field generated by the plasma and coils are illustrated in Figure 6-6. For this case, the field error is 4.007190 %.

The four cases presented in this section clearly show that the imposed force constraints are being satisfied. Also, the effects of the algorithm discussed at the end of Chapter 4 are not as severe for the case of force constraints. This is due to the nonlinear nature of the force equations, which allow the coil currents to vary while keeping the forces on a given coil constant.

6.4 Constraining Grouped Currents

One issue which did not arise for the case of simple current limits is the effect of a constraint when more than one coil carries the same current. This issue did not occur for the case of current

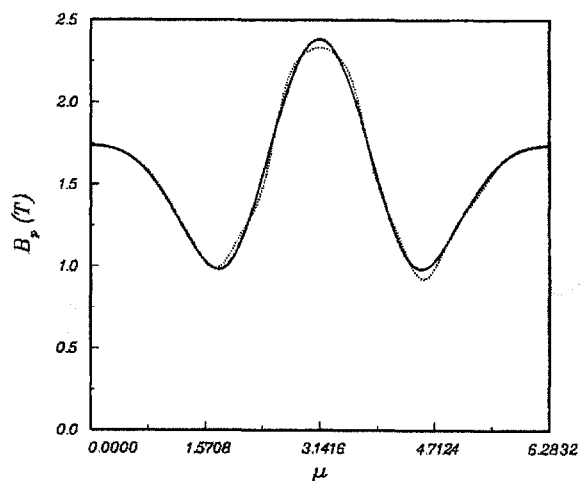


Figure 6-4: Poloidal fields for the case of two force constraints. The solid line represents the equilibrium field of the plasma, and the dotted line represents the field generated by the coils.

Table 6.4: Coil forces and currents for the case of two force constraints.

Coil Label	Radial Force (MN)	Axial Force (MN)	Current (kA)
OH1	10.366	-0.021	11.600
OH2U	3.555	-0.778	31.406
OH2L	3.481	0.833	29.711
EF1U	0.510	-2.422	50.034
EF1L	0.504	2.657	56.224
EF2U	-0.450	-0.162	6.514
EF2L	0.041	-0.018	-0.577
EF3U	0.618	0.175	-4.247
EF3L	0.623	-0.227	-4.247
EFCU	0.151	0.083	7.500
EFCL	-0.152	0.094	-7.500
EF4U	2.750	0.673	-55.114
EF4L	2.710	-0.723	-55.114

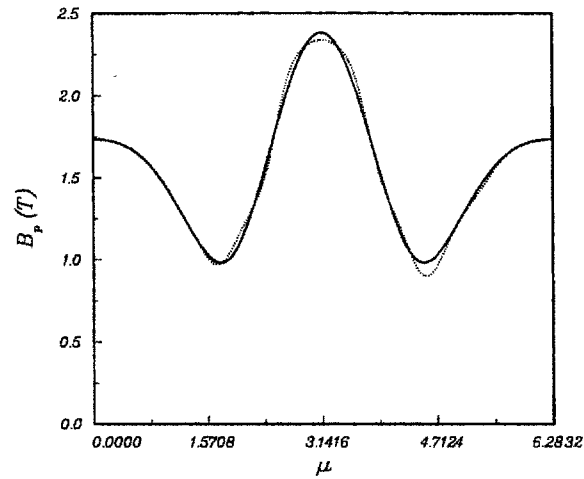


Figure 6-5: Poloidal fields for the case of three force constraints. The solid line is the field associated with the plasma equilibrium, and the dotted line is the sum of the plasma and PF coil fields.

Table 6.5: Coil forces and currents for the case of three force constraints.

Coil Label	Radial Force (MN)	Axial Force (MN)	Current (kA)
OH1	10.367	-0.025	11.600
OH2U	3.534	-0.743	30.831
OH2L	3.484	0.804	29.437
EF1U	0.538	-2.456	51.264
EF1L	0.525	2.691	57.301
EF2U	-0.450	-0.162	6.502
EF2L	0.041	-0.018	-0.576
EF3U	0.612	0.173	-4.198
EF3L	0.617	-0.224	-4.198
EFCU	0.151	0.082	7.500
EFCL	-0.152	0.094	-7.500
EF4U	2.759	0.675	-55.179
EF4L	2.719	-0.725	-55.179

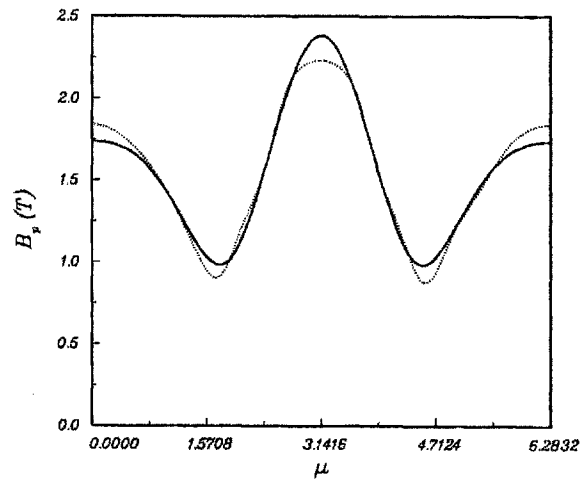


Figure 6-6: Poloidal fields for the case of four force constraints. The solid line shows the equilibrium field of the plasma, and the dotted line represents the sum of the plasma vacuum field and the fields of the PF coils.

Table 6.6: Coil forces and currents for the case of four force constraints.

Coil Label	Radial Force (MN)	Axial Force (MN)	Current (kA)
OH1	9.908	-0.021	11.600
OH2U	3.101	-0.587	26.898
OH2L	3.103	0.692	26.628
EF1U	0.539	-2.445	54.563
EF1L	0.478	2.606	58.073
EF2U	-0.448	-0.162	6.218
EF2L	0.041	-0.018	-0.555
EF3U	0.396	0.098	-2.505
EF3L	0.399	-0.128	-2.505
EFCU	0.153	0.080	7.500
EFCL	-0.153	0.092	-7.500
EF4U	3.390	0.745	-61.665
EF4L	3.345	-0.803	-61.665

constraints because the current carried by the grouped coils is treated as a single unique current by the global minimization algorithm. When grouped coils are subject to a force constraint, however, each coil must be treated independently. The nonlinearities of the force constraints can drastically affect the results. This will be demonstrated using three cases, all of which constrain the EF4U and EF4L coils. The maximum forces allowed on these coils are varied to obtain an idea of how the degree to which a constraint is violated affects the results.

For the unconstrained case presented in the previous section, the forces on the EF4U coil are 2.715 MN and 0.669 MN in the radial and axial directions, respectively. The radial force on the EF4L coil is 2.668 MN and the axial force is -0.726 MN. Setting the maximum value of the radial force to 2.700 MN and the maximum axial force to 1.000 MN gives the first set of test results. The coil currents and forces for this case are listed in Table 6.7. The resulting poloidal field is illustrated in Figure 6-7. The field error for this case is 5.303 %.

The second test imposes another constraint which is only violated by the EF4U coil, but now the violation is much worse. For this case, the maximum radial force on the coils is set to 2.675 MN. The poloidal fields for this case are shown in Figure 6-8, and the coil forces and currents are listed in Table 6.8. The field error for this is 14.044 %, much worse than for the previous case.

The final case for this section sets the maximum force in the radial direction for the EF4U and EF4L coils to 2.650 MN. The forces on both coils violate this constraint using the currents corresponding to the global minimum. The poloidal fields for this case are shown in Figure 6-9 and the coil forces and currents are shown in Table 6.9. The field error for this case is 16.068 %.

For this case, the field error grows steadily worse as the constraints grow more restrictive. This behavior is in part due to the sensitivity of the poloidal field to slight redistributions of the coil currents. The outboard coils (EF2U, EF2L, EFCU, EFCL, EF3U, EF3L, EF4U, and EF4L) are responsible for generating the majority of the poloidal field over the region of $\mu = -\pi/2$ to $\mu = \pi/2$. As the currents in these coils are adjusted to reduce the forces on the EF4U and EF4L coils, the ability of these coils to reproduce the equilibrium field over this region is greatly reduced. This problem may be avoided by adding more coils in this region or by allowing the EF3U, EF3L, EF4U, and EF4L to carry unique currents, giving the system the ability to adjust the current in each of these coils to reproduce the poloidal field at the plasma surface and satisfy the constraints simultaneously. This assertion is born out by the results in Figure 6-10 and

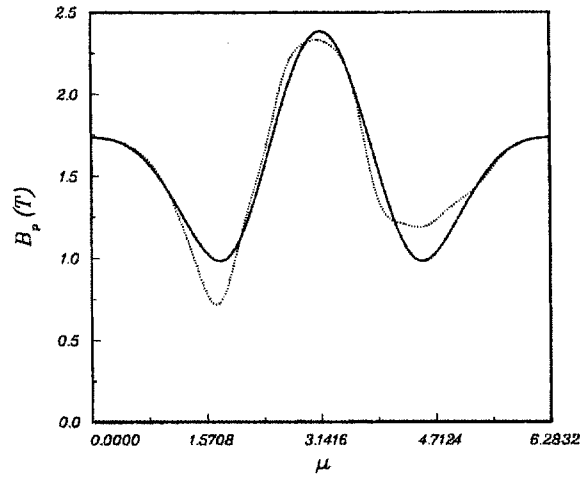


Figure 6-7: Poloidal fields for a force constraint on a set of grouped coils. The equilibrium field of the plasma is represented by the solid line. The dotted line shows the field generated by the PF system.

Table 6.7: Coil forces and currents for grouped coils subject to a force constraint.

Coil Label	Radial Force (MN)	Axial Force (MN)	Current (kA)
OH1	10.358	0.045	11.600
OH2U	3.313	-0.413	26.027
OH2L	3.589	1.313	34.807
EF1U	0.725	-2.813	65.199
EF1L	0.324	2.166	41.434
EF2U	-0.268	-0.091	3.712
EF2L	-0.107	-0.051	1.579
EF3U	0.630	0.193	-4.378
EF3L	0.639	-0.227	-4.378
EFCU	0.158	0.086	7.500
EFCL	-0.146	0.092	-7.500
EF4U	2.699	0.663	-54.654
EF4L	2.668	-0.720	-54.654

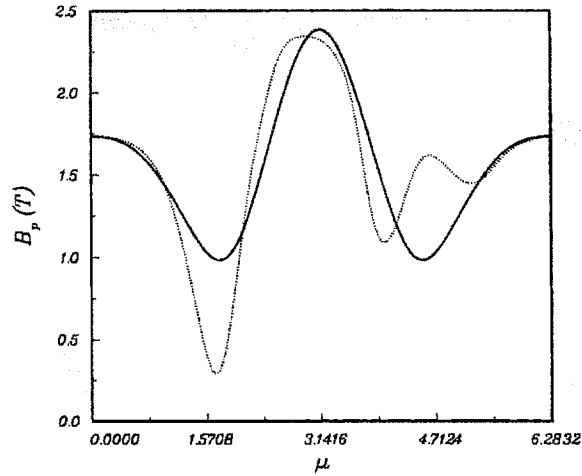


Figure 6-8: Poloidal fields for a constrained set of grouped coils. The equilibrium field of the plasma is shown by the solid line. The dotted line shows the sum of the plasma vacuum field with the field generated by the PF system.

Table 6.8: Coil forces and currents for grouped coils subject to force constraints.

Coil Label	Radial Force (MN)	Axial Force (MN)	Current (kA)
OH1	10.349	0.149	11.600
OH2U	2.632	-0.030	17.609
OH2L	3.477	2.263	42.813
EF1U	1.094	-3.121	89.332
EF1L	0.114	1.095	18.209
EF2U	0.102	0.033	-1.325
EF2L	-0.333	0.174	5.338
EF3U	0.604	0.209	-4.253
EF3L	0.623	-0.206	-4.253
EFCU	0.168	0.094	7.500
EFCL	-0.136	0.088	-7.500
EF4U	2.674	0.664	-54.540
EF4L	2.669	-0.719	-54.540

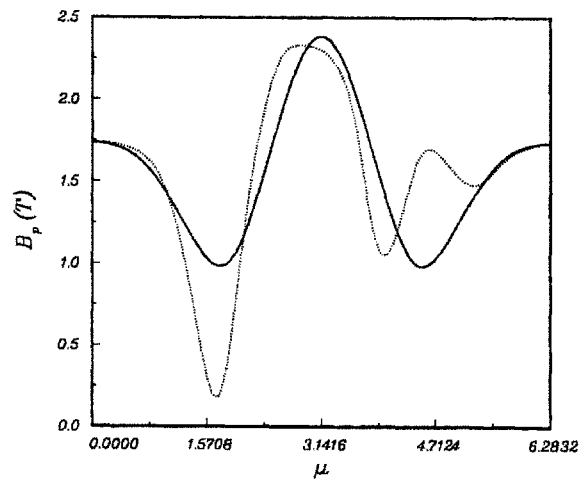


Figure 6-9: Poloidal fields for the case of a constrained set of grouped coils. The solid line shows the equilibrium field of the plasma. The dotted line shows the field due to the PF system.

Table 6.9: Coil forces and currents for the case of constrained grouped coils.

Coil Label	Radial Force (MN)	Axial Force (MN)	Current (kA)
OH1	10.245	0.173	11.600
OH2U	2.298	0.033	14.843
OH2L	3.353	2.420	43.750
EF1U	1.133	-3.111	96.172
EF1L	0.074	0.880	14.380
EF2U	0.332	0.108	-4.235
EF2L	-0.269	0.147	4.401
EF3U	0.551	0.208	-3.940
EF3L	0.571	-0.197	-3.940
EFCU	0.171	0.100	7.500
EFCL	-0.134	0.092	-7.500
EF4U	2.649	0.664	-54.413
EF4L	2.650	-0.719	-54.413

Table 6.10. Here, the constraints imposed on the EF4 coils are those of the previous test, and the EF3U, EF3L, EF4U, and EF4L coils are allowed to carry unique currents. The field error for this case is 5.872 %.

6.5 Combining Constraints

Given that both the linear constraint and force constraint system are based on the same algorithm, it should be possible to have current and force constraints occurring simultaneously within the coil set. For this case, the problem of finding the coil currents is expressed as

$$\begin{aligned}
 &\text{Minimize} && \mathbf{i}^T \cdot \mathbf{M} \cdot \mathbf{i} - 2\mathbf{n}^T \cdot \mathbf{i} + p \\
 &\text{Subject to} && \mathbf{F}_{Ri} \leq \mathbf{F}_R(\mathbf{i}) \leq \mathbf{F}_{Ro} \\
 &&& -\mathbf{F}_{Zm} \leq \mathbf{F}_Z(\mathbf{i}) \leq \mathbf{F}_{Zm} \\
 &&& -\mathbf{b} \leq \mathbf{l} \leq \mathbf{b}
 \end{aligned} \tag{6.12}$$

where \mathbf{l} is the constrained subset of group currents and \mathbf{b} is the corresponding set of maximum allowable currents.

The process of finding a feasible point proceeds as before, only now using three sets of constraint equations and three sets of Lagrange multipliers – two for the forces and one for currents. Since this process simply combines the analyses performed for the linear constraints and the force constraints, the details will be omitted here.

As a demonstration that the final version of the cPFC program can satisfy both current and force constraints, consider the coil set and equilibrium shown in Figure 6-1 once again. For this test, the current in the EF2U coil is limited to 6.500 kA and the forces acting on the EF3U and EF3L coils are limited to 0.640 MN in the radially outward direction and 1.000 MN in the axial direction. The results of this test are shown in Figure 6-11 and the coil currents and forces are listed in Table 6.11. The field error for this test is 2.647 %.

Since the general problem combines both current and force constraints, the discussion at the end of Chapter 4 is applicable here, also. In Chapter 4, it was found that a constraint which was inactive effectively locked the corresponding current to its initial value. Similar behavior was observed in the tests run in this chapter, but the nonlinear nature of the force constraints counteracted these effects, allowing the currents to vary while holding the force constant. These difficulties can be overcome by running cPFC first on the unconstrained case, examining the

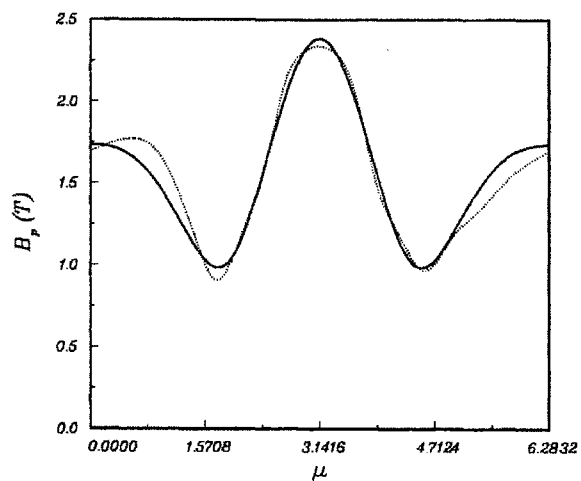


Figure 6-10: Poloidal fields for the previous case with the grouping requirement removed. The solid line shows the plasma equilibrium field. The dotted line shows the field due to the poloidal field coils.

Table 6.10: Coil forces and currents for the previous case with ungrouped coils.

Coil Label	Radial Force (MN)	Axial Force (MN)	Current (kA)
OH1	10.386	-0.006	11.600
OH2U	3.493	-0.593	29.355
OH2L	3.563	0.940	31.027
EF1U	0.390	-2.756	59.330
EF1L	0.537	2.527	52.207
EF2U	0.051	0.017	-0.685
EF2L	0.122	-0.070	-1.994
EF3U	0.802	0.321	-5.758
EF3L	0.302	-0.120	-2.266
EFCU	0.170	0.106	7.500
EFCL	-0.131	0.095	-7.500
EF4U	2.650	0.997	-57.265
EF4L	2.212	-0.391	-46.615

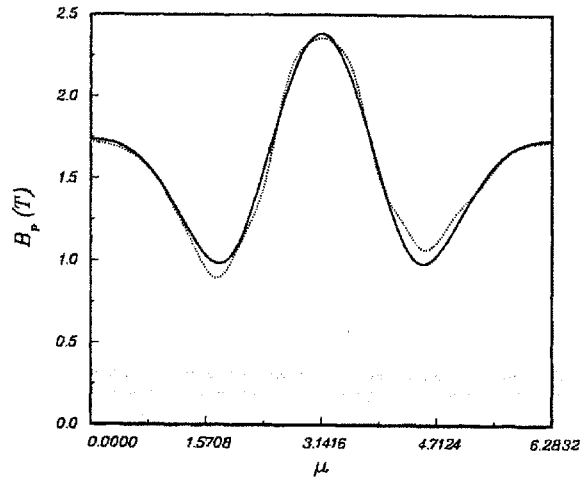


Figure 6-11: Poloidal fields for the general case of current and force constraints. The solid line represents the equilibrium field of the plasma. The dotted line shows the field generated by the PF system.

Table 6.11: Coil forces and currents for the general case of current and force constraints.

Coil Label	Radial Force (MN)	Axial Force (MN)	Current (kA)
OH1	10.482	0.046	11.600
OH2U	3.739	-0.722	32.075
OH2L	3.511	1.008	31.207
EF1U	0.564	-2.576	53.292
EF1L	0.448	2.472	50.292
EF2U	-0.450	-0.161	6.500
EF2L	0.003	-0.001	-0.044
EF3U	0.639	0.182	-4.438
EF3L	0.640	-0.239	-4.438
EFCU	0.152	0.082	7.500
EFCL	-0.149	0.095	-7.500
EF4U	2.665	0.654	-54.036
EF4L	2.609	-0.722	-54.036

results, and setting the constraints appropriately. By adding only one constraint at a time, it is possible to find a set of coil currents which satisfies all of the constraints and adequately supports the equilibrium.

The final topic for discussion is the execution time of the force constraint algorithm. Consider first the last test case of Section 6.3. This test imposed two active and two inactive force constraints on the coil currents. The CPU time necessary to run this case on a Cray-2 was 18.97 seconds. Of this, the force constraint algorithm required 1.025 CPU seconds to determine the coil currents, and the time needed to generate the various quantities for computing the forces was 7.555 seconds. The unconstrained case required only 11.07 CPU seconds to run, of which 0.685 CPU seconds were devoted to finding the coil currents. These results show that the force constraint algorithm increases the total running time by approximately two-thirds.

Chapter 7

Conclusions and Recommendations

As discussed in Chapter 1, this thesis has described the development of a design tool for the poloidal field magnet system of a tokamak. This was done by modifying an existing program to:

1. Better model realistic plasma and coil configurations,
2. Find a set of coil currents which support a specified equilibrium such that the maximum currents in the coils are not exceeded,
3. Find a set of coil currents to support an equilibrium such that the maximum allowable forces on the coils are not exceeded.

All of these goals were achieved with satisfactory results. There is, however, a substantial amount of work which can be done to increase the usefulness of the cPFC program even further.

This work falls into two categories. First, there is additional work needed to further verify the results of the cPFC program. This requires benchmarking the cPFC program against other programs. Since the other available programs solve the free-boundary Grad-Shafranov equation, such a benchmark requires comparing the combined results of the cPFC program and Haney's fast equilibrium solver with those of the other programs. Another, potentially better, benchmark would involve using the cPFC program to reconstruct the coil currents from an actual experiment.

Additional work to the cPFC program itself includes, but is not limited to, the following:

- Implement an automated algorithm which determines an optimal set of coil currents,

- Modify the program to automatically find the coil currents at a number of times during the ohmic discharge,
- Estimate the net force acting on the plasma,
- Add a separate program to calculate the intercoil forces, thereby reducing the execution time for cPFC on finalized designs.

These additions to the program would further enhance its use as a design tool.

Appendix A

Verification of Asymmetric Program

In Chapter 3 the changes needed to transform the original cPFC program into a form which would deal with asymmetric plasmas and coil sets were presented. The primary test of the new version of the program is to guarantee that it produce results which are identical to those obtained using the up-down symmetric version of cPFC for systems which are up-down symmetric. The data for one up-down symmetric case were presented in Chapter 3. In this appendix, data for two more cases will be presented. These three test cases provide sufficient proof that the asymmetric version exactly reproduces the results obtained with the symmetric version for symmetric cases.

A.1 Case 1: A Conventional Tokamak

In this section, the data for the symmetric and asymmetric versions of the cPFC program are compared for the case of the conventional tokamak coil set and plasma illustrated in Figure A-1. This equilibrium is characterized by the parameters in Table A.1.

The coil data for the case of the three coils being grouped up-down is given in Table A.2. The data for the coils being allowed to carry unique currents is presented in Table A.3. As expected for symmetric systems, the coil currents for the grouped and ungrouped cases are identical. The field error for this system is very small, only 0.75 %, indicating that the coils can very accurately produce the poloidal field required to maintain this equilibrium. Finally, the poloidal field data is shown in Figure A-2. The dotted line (indicating the field produced by the coils) is marginally displaced from the solid line representing the plasma's poloidal field.

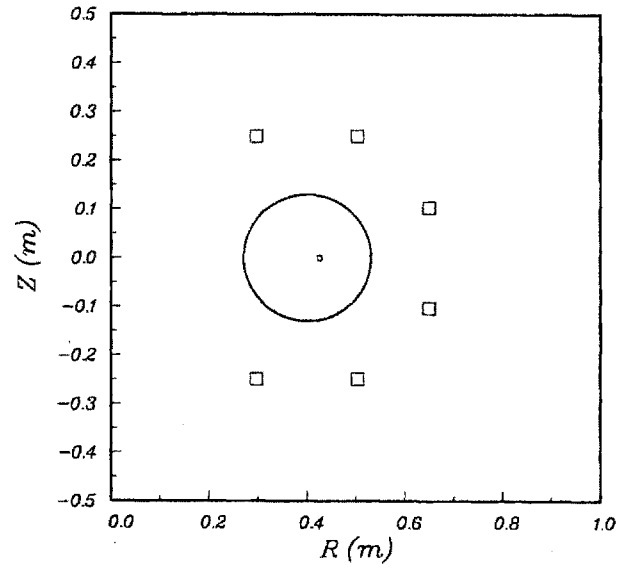


Figure A-1: A conventional tokamak coil set and circular plasma

Table A.1: Equilibrium data for the conventional tokamak test case.

<i>Parameter</i>	<i>Value</i>
R_0 (m)	0.400
a (m)	0.130
δ	0.000
κ	1.000
B_0 (T)	0.700
I_p (kA)	10.000
β_p	1.000
β_t (%)	0.049

Table A.2: Data for coil groups EF1 (T) and EF1 (B), EF2 (T) and EF2 (B), and EF3 (T) and EF3 (B) carrying symmetric currents.

	<i>Symmetric</i>	<i>Asymmetric</i>		<i>Symmetric</i>	<i>Asymmetric</i>
Coil	Current (kA)		Coil	Current (kA)	
EF1 (T)	-1.951	-1.951	EF1 (B)	-1.951	-1.951
EF2 (T)	-1.724	-1.724	EF2 (B)	-1.724	-1.724
EF3 (T)	-1.432	-1.432	EF3 (B)	-1.432	-1.432
	Error (%)				
<i>Field Error</i>	0.75265	0.75265			

Table A.3: Data for coils EF1 (T), EF1 (B), EF2 (T), EF2 (B), EF3 (T), and EF3 (B) carrying unique currents.

	<i>Symmetric</i>	<i>Asymmetric</i>		<i>Symmetric</i>	<i>Asymmetric</i>
Coil	Current (kA)		Coil	Current (kA)	
EF1 (T)	-1.951	-1.951	EF1 (B)	-1.951	-1.951
EF2 (T)	-1.724	-1.724	EF2 (B)	-1.724	-1.724
EF3 (T)	-1.432	-1.432	EF3 (B)	-1.432	-1.432
	Error (%)				
<i>Field Error</i>	0.75265	0.75265			

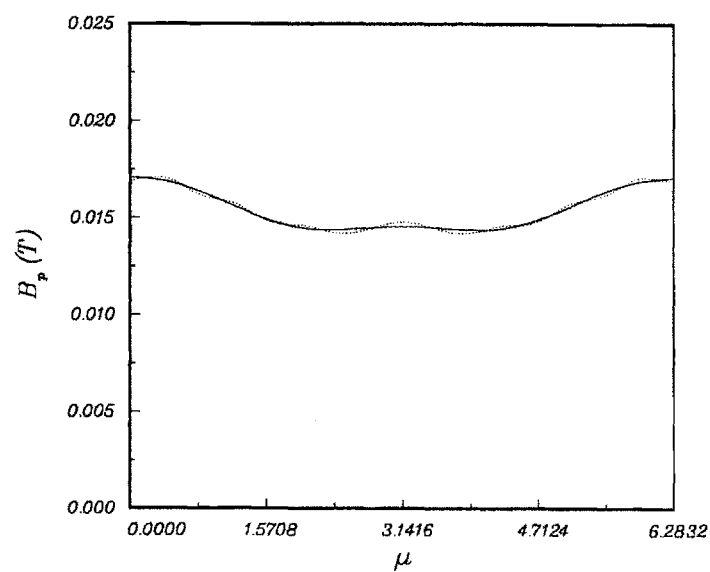


Figure A-2: Poloidal field comparison for the conventional tokamak case. The solid line is the poloidal field due to the plasma at the plasma surface. The dotted line (barely visible) is the field produced by the coils.

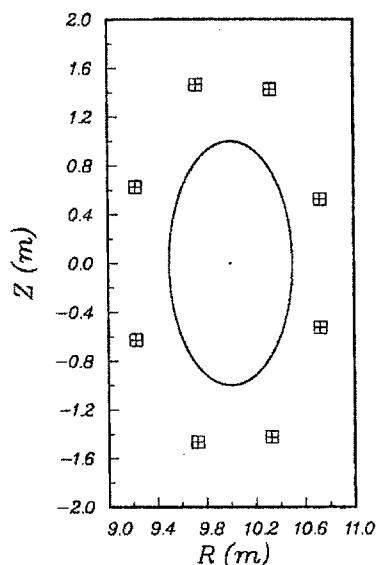


Figure A-3: Highly elongated tokamak plasma and coil set.

A.2 Case 2: An Elongated Tokamak

In this section, the data from the symmetric and asymmetric versions of the cPFC program are compared for the case of the highly elongated tokamak shown in Figure A-3. The plasma shown in Figure A-3 is characterized by the equilibrium data in Table A.4.

This test case is slightly different from the other two in that each coil is now made up of four unique wires. Each wire in an individual coil is constrained to carry the same current (as discussed in Chapter 2). For this case, then, the two tests consist of *coils* which are either grouped up-down or independent, while the wires comprising each coil carry the same current. The data presented here list the *total* current in each coil.

The data for the case where the coils are grouped up-down symmetrically are presented in Table A.5, and the data for the ungrouped case are given in Table A.6. Finally, the poloidal field generated by the combination of these coil currents and the plasma current is compared with the plasma's equilibrium poloidal field in Figure A-4. The difference between the two is quite apparent, clearly illustrating the 10 % field error obtained for this system. This large error is due to the small number of coils in the system and indicates that this coil set is not capable of supporting the specified equilibrium.

Table A.4: Equilibrium data for the highly elongated tokamak.

<i>Parameter</i>	<i>Value</i>
R_0 (m)	10.000
a (m)	0.500
δ	0.000
κ	2.000
B_0 (T)	3.140
I_p (MA)	1.000
β_p	0.001
β_t (%)	0.060

Table A.5: Data for coil groups OH1 (T) and OH1 (B), EF1 (T) and EF1 (B), EF2 (T) and EF2 (B), and EF3 (T) and EF3 (B) carrying symmetric currents.

	<i>Symmetric</i>	<i>Asymmetric</i>		<i>Symmetric</i>	<i>Asymmetric</i>
Coil	Current (kA)		Coil	Current (kA)	
OH1 (T)	20.665	20.665	OH1 (B)	20.665	20.665
EF1 (T)	84.424	84.424	EF1 (B)	84.424	84.424
EF2 (T)	35.775	35.775	EF2 (B)	35.775	35.775
EF3 (T)	-17.739	-17.739	EF3 (B)	-17.739	-17.739
	Error (%)				
<i>Field Error</i>	9.31833	9.31833			

Table A.6: Data for coils OH1 (T), OH2 (B), EF1 (T), EF1 (B), EF2 (T), EF2 (B), EF3 (T), and EF3 (B) carrying unique currents.

	<i>Symmetric</i>	<i>Asymmetric</i>		<i>Symmetric</i>	<i>Asymmetric</i>
Coil	Current (kA)		Coil	Current (kA)	
OH1 (T)	20.665	20.665	OH1 (B)	20.665	20.665
EF1 (T)	84.424	84.424	EF1 (B)	84.424	84.424
EF2 (T)	35.775	35.775	EF2 (B)	35.775	35.775
EF3 (T)	-17.739	-17.739	EF3 (B)	-17.739	-17.739
	Error (%)				
<i>Field Error</i>	9.31833	9.31833			

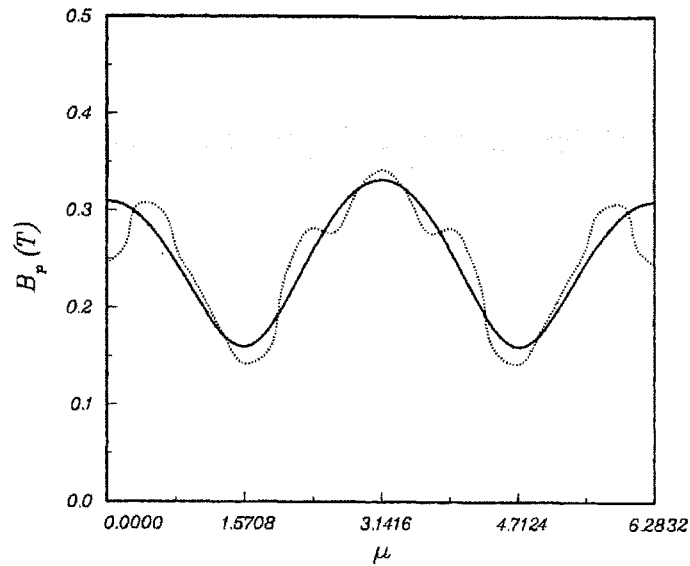


Figure A-4: Field comparison for the highly elongated tokamak case. The equilibrium poloidal field of the plasma is the solid line. The dotted line is the best obtainable match to the equilibrium using this algorithm.

Appendix B

Alcator C-Mod Coil Set

This appendix lists the locations of each of the wires making up the 13 coils of the Alcator C-Mod Coil Set used in Chapters 3, 4, and 6 for testing the modifications to cPFC.

The wires for the EF1U and EF1L coils are listed in Table B.1. Each of these wires is 0.0227 m in thickness and 0.0237 m in height.

Table B.2 lists the locations of the wires for the EF2U and EF2L coils. Each of the wires has a radial thickness of 0.0230 m and an axial height of 0.0237 m.

Each of the wires listed in Table B.3 for the EF3U and EF3L coils has a radial width of 0.0252 m and a height of 0.0240 m.

Table B.4 lists the wire positions making up the EFCU and EFCL coils. These coils are used to control the vertical position of the plasma. Each of the wires making up these coils is 0.0191 m wide by 0.0247 m high.

The wires listed in Table B.5 comprise the EF4U and EF4L coils. Each of these wires is 0.0227 m wide and 0.0237 m high.

The wires making up the upper and lower segments of the OH2 coil are listed in Table B.6. These wires measure 0.0174 m in width by 0.0240 m in height.

Finally, the wires comprising the ohmic transformer (the OH1 coil) are listed in Table B.7. Each of these wires measures 0.0174 m in the radial direction by 0.0240 m in the axial direction.

Table B.1: EF1U and EF1L wire locations.

EF1U			EF1L		
Wire	R (m)	Z (m)	Wire	R (m)	Z (m)
EF1U.01	0.4457	0.5585	EF1L.01	0.4457	-0.5585
EF1U.02	0.4684	0.5585	EF1L.02	0.4684	-0.5585
EF1U.03	0.4912	0.5585	EF1L.03	0.4912	-0.5585
EF1U.04	0.5139	0.5585	EF1L.04	0.5139	-0.5585
EF1U.05	0.4457	0.5822	EF1L.05	0.4457	-0.5822
EF1U.06	0.4684	0.5822	EF1L.06	0.4684	-0.5822
EF1U.07	0.4912	0.5822	EF1L.07	0.4912	-0.5822
EF1U.08	0.5139	0.5822	EF1L.08	0.5139	-0.5822
EF1U.09	0.4457	0.6060	EF1L.09	0.4457	-0.6060
EF1U.10	0.4684	0.6060	EF1L.10	0.4684	-0.6060
EF1U.11	0.4912	0.6060	EF1L.11	0.4912	-0.6060
EF1U.12	0.5139	0.6060	EF1L.12	0.5139	-0.6060
EF1U.13	0.4457	0.6297	EF1L.13	0.4457	-0.6297
EF1U.14	0.4684	0.6297	EF1L.14	0.4684	-0.6297
EF1U.15	0.4912	0.6297	EF1L.15	0.4912	-0.6297
EF1U.16	0.5139	0.6297	EF1L.16	0.5139	-0.6297

Table B.2: EF2U and EF2L wire locations.

EF2U			EF2L		
Wire	R (m)	Z (m)	Wire	R (m)	Z (m)
EF2U_01	0.8423	0.5585	EF2L_01	0.8423	-0.5585
EF2U_02	0.8653	0.5585	EF2L_02	0.8653	-0.5585
EF2U_03	0.8882	0.5585	EF2L_03	0.8882	-0.5585
EF2U_04	0.9112	0.5585	EF2L_04	0.9112	-0.5585
EF2U_05	0.8423	0.5822	EF2L_05	0.8423	-0.5822
EF2U_06	0.8653	0.5822	EF2L_06	0.8653	-0.5822
EF2U_07	0.8882	0.5822	EF2L_07	0.8882	-0.5822
EF2U_08	0.9112	0.5822	EF2L_08	0.9112	-0.5822
EF2U_09	0.8423	0.6060	EF2L_09	0.8423	-0.6060
EF2U_10	0.8653	0.6060	EF2L_10	0.8653	-0.6060
EF2U_11	0.8882	0.6060	EF2L_11	0.8882	-0.6060
EF2U_12	0.9112	0.6060	EF2L_12	0.9112	-0.6060
EF2U_13	0.8423	0.6297	EF2L_13	0.8423	-0.6297
EF2U_14	0.8653	0.6297	EF2L_14	0.8653	-0.6297
EF2U_15	0.8882	0.6297	EF2L_15	0.8882	-0.6297
EF2U_16	0.9112	0.6297	EF2L_16	0.9112	-0.6297

Table B.3: EF3U and EF3L wire locations.

EF3U			EF3L		
Wire	R (m)	Z (m)	Wire	R (m)	Z (m)
EF3U_01	0.9678	0.3899	EF3L_01	0.9678	-0.3899
EF3U_02	0.9930	0.3899	EF3L_02	0.9930	-0.3899
EF3U_03	1.0182	0.3899	EF3L_03	1.0182	-0.3899
EF3U_04	1.0434	0.3899	EF3L_04	1.0434	-0.3899
EF3U_05	0.9678	0.4139	EF3L_05	0.9678	-0.4139
EF3U_06	0.9930	0.4139	EF3L_06	0.9930	-0.4139
EF3U_07	1.0182	0.4139	EF3L_07	1.0182	-0.4139
EF3U_08	1.0434	0.4139	EF3L_08	1.0434	-0.4139
EF3U_09	0.9678	0.4379	EF3L_09	0.9678	-0.4379
EF3U_10	0.9930	0.4379	EF3L_10	0.9930	-0.4379
EF3U_11	1.0182	0.4379	EF3L_11	1.0182	-0.4379
EF3U_12	1.0434	0.4379	EF3L_12	1.0434	-0.4379
EF3U_13	0.9678	0.4619	EF3L_13	0.9678	-0.4619
EF3U_14	0.9930	0.4619	EF3L_14	0.9930	-0.4619
EF3U_15	1.0182	0.4619	EF3L_15	1.0182	-0.4619
EF3U_16	1.0434	0.4619	EF3L_16	1.0434	-0.4619
EF3U_17	0.9678	0.4859	EF3L_17	0.9678	-0.4859
EF3U_18	0.9930	0.4859	EF3L_18	0.9930	-0.4859
EF3U_19	1.0182	0.4859	EF3L_19	1.0182	-0.4859
EF3U_20	1.0434	0.4859	EF3L_20	1.0434	-0.4859
EF3U_21	0.9678	0.5099	EF3L_21	0.9678	-0.5099
EF3U_22	0.9930	0.5099	EF3L_22	0.9930	-0.5099
EF3U_23	1.0182	0.5099	EF3L_23	1.0182	-0.5099
EF3U_24	1.0434	0.5099	EF3L_24	1.0434	-0.5099

Table B.4: EFCU and EFCL wire locations.

EF4U			EF4L		
Wire	R (m)	Z (m)	Wire	R (m)	Z (m)
EFCU_01	0.8403	0.4178	EFCL_01	0.8403	-0.4178
EFCU_02	0.8594	0.4178	EFCL_02	0.8594	-0.4178
EFCU_03	0.8403	0.4425	EFCL_03	0.8403	-0.4425
EFCU_04	0.8594	0.4425	EFCL_04	0.8594	-0.4425

Table B.5: EF4U and EF4L wire locations.

EF4U			EF4L		
Wire	R (m)	Z (m)	Wire	R (m)	Z (m)
EF4U_01	1.4719	0.4107	EF4L_01	1.4719	-0.4107
EF4U_02	1.4946	0.4107	EF4L_02	1.4946	-0.4107
EF4U_03	1.5173	0.4107	EF4L_03	1.5173	-0.4107
EF4U_04	1.5400	0.4107	EF4L_04	1.5400	-0.4107
EF4U_05	1.4719	0.4344	EF4L_05	1.4719	-0.4344
EF4U_06	1.4946	0.4344	EF4L_06	1.4946	-0.4344
EF4U_07	1.5173	0.4344	EF4L_07	1.5173	-0.4344
EF4U_08	1.5400	0.4344	EF4L_08	1.5400	-0.4344
EF4U_09	1.4719	0.4582	EF4L_09	1.4719	-0.4582
EF4U_10	1.4946	0.4582	EF4L_10	1.4946	-0.4582
EF4U_11	1.5173	0.4582	EF4L_11	1.5173	-0.4582
EF4U_12	1.5400	0.4582	EF4L_12	1.5400	-0.4582
EF4U_13	1.4719	0.4819	EF4L_13	1.4719	-0.4819
EF4U_14	1.4946	0.4819	EF4L_14	1.4946	-0.4819
EF4U_15	1.5173	0.4819	EF4L_15	1.5173	-0.4819
EF4U_16	1.5400	0.4819	EF4L_16	1.5400	-0.4819

Table B.6: OH2U and OH2L wire locations.

OH2U			OH2L		
Wire	R (m)	Z (m)	Wire	R (m)	Z (m)
OH2U_01	0.3584	0.2637	OH2L_01	0.3584	-0.2637
OH2U_02	0.3584	0.2877	OH2L_02	0.3584	-0.2877
OH2U_03	0.3584	0.3117	OH2L_03	0.3584	-0.3117
OH2U_04	0.3584	0.3356	OH2L_04	0.3584	-0.3356
OH2U_05	0.3584	0.3596	OH2L_05	0.3584	-0.3596
OH2U_06	0.3584	0.3836	OH2L_06	0.3584	-0.3836
OH2U_07	0.3584	0.4075	OH2L_07	0.3584	-0.4075
OH2U_08	0.3584	0.4315	OH2L_08	0.3584	-0.4315
OH2U_09	0.3584	0.4555	OH2L_09	0.3584	-0.4555
OH2U_10	0.3584	0.4795	OH2L_10	0.3584	-0.4795
OH2U_11	0.3584	0.5034	OH2L_11	0.3584	-0.5034
OH2U_12	0.3584	0.5274	OH2L_12	0.3584	-0.5274
OH2U_13	0.3584	0.5514	OH2L_13	0.3584	-0.5514
OH2U_14	0.3758	0.2397	OH2L_14	0.3758	-0.2397
OH2U_15	0.3758	0.2637	OH2L_15	0.3758	-0.2637
OH2U_16	0.3758	0.2877	OH2L_16	0.3758	-0.2877
OH2U_17	0.3758	0.3117	OH2L_17	0.3758	-0.3117
OH2U_18	0.3758	0.3356	OH2L_18	0.3758	-0.3356
OH2U_19	0.3758	0.3596	OH2L_19	0.3758	-0.3596
OH2U_20	0.3758	0.3836	OH2L_20	0.3758	-0.3836
OH2U_21	0.3758	0.4075	OH2L_21	0.3758	-0.4075
OH2U_22	0.3758	0.4315	OH2L_22	0.3758	-0.4315
OH2U_23	0.3758	0.4555	OH2L_23	0.3758	-0.4555
OH2U_24	0.3758	0.4795	OH2L_24	0.3758	-0.4795
OH2U_25	0.3758	0.5034	OH2L_25	0.3758	-0.5034
OH2U_26	0.3758	0.5274	OH2L_26	0.3758	-0.5274
OH2U_27	0.3758	0.5514	OH2L_27	0.3758	-0.5514

Table B.7: Wire locations of the OH1 ohmic transformer.

OH1					
Wire	R (m)	Z (m)	Wire	R (m)	Z (m)
OH1_001	0.3236	-0.5514	OH1_002	0.3236	-0.5274
OH1_003	0.3236	-0.5034	OH1_004	0.3236	-0.4795
OH1_005	0.3236	-0.4555	OH1_006	0.3236	-0.4315
OH1_007	0.3236	-0.4075	OH1_008	0.3236	-0.3836
OH1_009	0.3236	-0.3596	OH1_010	0.3236	-0.3356
OH1_011	0.3236	-0.3117	OH1_012	0.3236	-0.2877
OH1_013	0.3236	-0.2637	OH1_014	0.3236	-0.2397
OH1_015	0.3236	-0.2158	OH1_016	0.3236	-0.1918
OH1_017	0.3236	-0.1678	OH1_018	0.3236	-0.1438
OH1_019	0.3236	-0.1199	OH1_020	0.3236	-0.0959
OH1_021	0.3236	-0.0719	OH1_022	0.3236	-0.0479
OH1_023	0.3236	-0.0240	OH1_024	0.3236	+0.0000
OH1_025	0.3236	+0.0240	OH1_026	0.3236	+0.0479
OH1_027	0.3236	+0.0719	OH1_028	0.3236	+0.0959
OH1_029	0.3236	+0.1199	OH1_030	0.3236	+0.1438
OH1_031	0.3236	+0.1678	OH1_032	0.3236	+0.1918
OH1_033	0.3236	+0.2158	OH1_034	0.3236	+0.2397
OH1_035	0.3236	+0.2637	OH1_036	0.3236	+0.2877
OH1_037	0.3236	+0.3117	OH1_038	0.3236	+0.3356
OH1_039	0.3236	+0.3596	OH1_040	0.3236	+0.3836
OH1_041	0.3236	+0.4075	OH1_042	0.3236	+0.4315
OH1_043	0.3236	+0.4555	OH1_044	0.3236	+0.4795
OH1_045	0.3236	+0.5034	OH1_046	0.3236	+0.5274
OH1_047	0.3236	+0.5514	OH1_048	0.3410	-0.5514
OH1_049	0.3410	-0.5274	OH1_050	0.3410	-0.5034

Table B.7: Continued

OH1					
Wire	R (m)	Z (m)	Wire	R (m)	Z (m)
OH1.051	0.3410	-0.4795	OH1.052	0.3410	-0.4555
OH1.053	0.3410	-0.4315	OH1.054	0.3410	-0.4075
OH1.055	0.3410	-0.3836	OH1.056	0.3410	-0.3596
OH1.057	0.3410	-0.3356	OH1.058	0.3410	-0.3117
OH1.059	0.3410	-0.2877	OH1.060	0.3410	-0.2637
OH1.061	0.3410	-0.2397	OH1.062	0.3410	-0.2158
OH1.063	0.3410	-0.1918	OH1.064	0.3410	-0.1678
OH1.065	0.3410	-0.1438	OH1.066	0.3410	-0.1199
OH1.067	0.3410	-0.0959	OH1.068	0.3410	-0.0719
OH1.069	0.3410	-0.0480	OH1.070	0.3410	-0.0240
OH1.071	0.3410	+0.0000	OH1.072	0.3410	+0.0240
OH1.073	0.3410	+0.0479	OH1.074	0.3410	+0.0719
OH1.075	0.3410	+0.0959	OH1.076	0.3410	+0.1199
OH1.077	0.3410	+0.1438	OH1.078	0.3410	+0.1678
OH1.079	0.3410	+0.1918	OH1.080	0.3410	+0.2277
OH1.081	0.3410	+0.2517	OH1.082	0.3410	+0.2757
OH1.083	0.3410	+0.2997	OH1.084	0.3410	+0.3236
OH1.085	0.3410	+0.3476	OH1.086	0.3410	+0.3716
OH1.087	0.3410	+0.3955	OH1.088	0.3410	+0.4195
OH1.089	0.3410	+0.4435	OH1.090	0.3410	+0.4675
OH1.091	0.3410	+0.4914	OH1.092	0.3410	+0.5154
OH1.093	0.3410	+0.5394	OH1.094	0.3410	+0.5754
OH1.095	0.3584	-0.1918	OH1.096	0.3584	-0.1678
OH1.097	0.3584	-0.1438	OH1.098	0.3584	-0.1199
OH1.099	0.3584	-0.0959	OH1.100	0.3584	-0.0719

Table B.7: Continued

OH1					
Wire	R (m)	Z (m)	Wire	R (m)	Z (m)
OH1_101	0.3584	-0.0479	OH1_102	0.3584	-0.0240
OH1_103	0.3584	+0.0000	OH1_104	0.3584	+0.0240
OH1_105	0.3584	+0.0479	OH1_106	0.3584	+0.0719
OH1_107	0.3584	+0.0959	OH1_108	0.3584	+0.1199
OH1_109	0.3584	+0.1438	OH1_110	0.3584	+0.1678
OH1_111	0.3584	+0.1918	OH1_112	0.3758	-0.2038
OH1_113	0.3758	-0.1798	OH1_114	0.3758	-0.1558
OH1_115	0.3758	-0.1319	OH1_116	0.3758	-0.1079
OH1_117	0.3758	-0.0839	OH1_118	0.3758	-0.0599
OH1_119	0.3758	-0.0360	OH1_120	0.3758	-0.0120
OH1_121	0.3758	+0.0120	OH1_122	0.3758	+0.0360
OH1_123	0.3758	+0.0599	OH1_124	0.3758	+0.0839
OH1_125	0.3758	+0.1079	OH1_126	0.3758	+0.1319
OH1_127	0.3758	+0.1558	OH1_128	0.3758	+0.1798
OH1_129	0.3758	+0.2038			

Appendix C

Symmetry Relations

In this appendix, various symmetry relations for the function $G(r, z; r', z')$ are developed. These relations are then used to demonstrate the symmetry of the energy $U_{j \rightarrow i}$ which, in turn, is used to demonstrate the symmetry of the mutual inductance M_{ij} .

C.1 Symmetry of $G(r, z; r', z')$

In this section, the symmetry of the function

$$G(r, z; r', z')$$

with respect to the exchange of variables

$$\begin{aligned} r &\longleftrightarrow r' \\ z &\longleftrightarrow z' \end{aligned}$$

will be demonstrated. The function $G(r, z; r', z')$ is defined as

$$G(r, z; r', z') = \frac{2A}{rr'} \left[\left(1 - \frac{k^2}{2}\right) K(k) - E(k) \right]$$

where

$$\begin{aligned} A^2 &= (r + r')^2 + (z - z')^2 \\ k^2 &= \frac{4rr'}{A^2} \end{aligned}$$

so that by demonstrating the symmetry of A and k , the symmetry of G will follow.

C.1.1 Exchange of r and r'

Under the exchange of r and r' , we obtain:

$$\begin{aligned} A'^2 &= (r' + r)^2 + (z - z')^2 \\ &= (r + r')^2 + (z - z')^2 \\ &= A^2 \end{aligned}$$

and

$$\begin{aligned} k'^2 &= \frac{4r'r}{A'^2} \\ &= \frac{4rr'}{A^2} \\ &= k^2 \end{aligned}$$

so that

$$\begin{aligned} G(r', z; r, z') &= \frac{2A'}{r'r} \left[\left(1 - \frac{k'^2}{2}\right) K(k') - E(k') \right] \\ &= \frac{2A}{rr'} \left[\left(1 - \frac{k^2}{2}\right) K(k) - E(k) \right] \\ &= G(r, z; r', z') \end{aligned}$$

C.1.2 Exchange of z and z'

The exchange of z with z' proceeds in a similar manner:

$$\begin{aligned} A'^2 &= (r + r')^2 + (z' - z)^2 \\ &= (r + r')^2 + (-1)^2 (z - z')^2 \\ &= (r + r')^2 + (z - z')^2 \\ &= A^2 \end{aligned}$$

and

$$k'^2 = \frac{4rr'}{A'^2} = \frac{4rr'}{A^2} = k^2$$

resulting in

$$G(r, z'; r', z) = G(r, z; r', z')$$

C.1.3 Results

Quoting the previous results:

$$\begin{aligned} G(r, z; r', z') &= G(r', z; r, z') \\ &= G(r, z'; r', z) \end{aligned}$$

and, by extension,

$$G(r, z; r', z') = G(r', z'; r, z)$$

C.2 Symmetry of $U_{j \rightarrow i}$

In this section, the symmetry relation

$$U_{j \rightarrow i} = U_{i \rightarrow j}$$

will be demonstrated. The full expression for $U_{j \rightarrow i}$ is given by

$$U_{j \rightarrow i} = \frac{\mu_0}{4} \int_{Z_i - \frac{h_i}{2}}^{Z_i + \frac{h_i}{2}} \int_{R_i - \frac{w_i}{2}}^{R_i + \frac{w_i}{2}} \int_{Z_j - \frac{h_j}{2}}^{Z_j + \frac{h_j}{2}} \int_{R_j - \frac{w_j}{2}}^{R_j + \frac{w_j}{2}} J_i J_j r r' G(r, z; r', z') dr' dz' dr dz \quad (\text{C.1})$$

Exchanging the subscripts i and j gives

$$U_{i \rightarrow j} = \frac{\mu_0}{4} \int_{Z_j - \frac{h_j}{2}}^{Z_j + \frac{h_j}{2}} \int_{R_j - \frac{w_j}{2}}^{R_j + \frac{w_j}{2}} \int_{Z_i - \frac{h_i}{2}}^{Z_i + \frac{h_i}{2}} \int_{R_i - \frac{w_i}{2}}^{R_i + \frac{w_i}{2}} J_j J_i r r' G(r', z'; r, z) dr' dz' dr dz$$

Now, rearranging the order of integration results in

$$U_{i \rightarrow j} = \frac{\mu_0}{4} \int_{Z_i - \frac{h_i}{2}}^{Z_i + \frac{h_i}{2}} \int_{R_i - \frac{w_i}{2}}^{R_i + \frac{w_i}{2}} \int_{Z_j - \frac{h_j}{2}}^{Z_j + \frac{h_j}{2}} \int_{R_j - \frac{w_j}{2}}^{R_j + \frac{w_j}{2}} J_i J_j r r' G(r', z'; r, z) dr dz dr' dz'$$

Now, making the exchange of variables

$$\begin{aligned} r &\longleftrightarrow r' \\ z &\longleftrightarrow z' \end{aligned}$$

and making use of the symmetry relations for G developed in the previous section gives

$$U_{i \rightarrow j} = \frac{\mu_0}{4} \int_{Z_i - \frac{h_i}{2}}^{Z_i + \frac{h_i}{2}} \int_{R_i - \frac{w_i}{2}}^{R_i + \frac{w_i}{2}} \int_{Z_j - \frac{h_j}{2}}^{Z_j + \frac{h_j}{2}} \int_{R_j - \frac{w_j}{2}}^{R_j + \frac{w_j}{2}} J_i J_j r r' G(r, z; r', z') dr' dz' dr dz$$

where the right-hand side is identical to the right-hand side of equation C.1 so that

$$U_{j \rightarrow i} = U_{i \rightarrow j}$$

C.3 Symmetry of M_{ij}

In this section the symmetry relation

$$M_{ij} = M_{ji}$$

is demonstrated.

The mutual inductance M_{ij} is defined as

$$M_{ij} = \frac{2U_{j \rightarrow i}}{I_i I_j}$$

Exchanging the subscripts i and j results in

$$\begin{aligned} M_{ji} &= \frac{2U_{i \rightarrow j}}{I_j I_i} \\ &= \frac{2U_{j \rightarrow i}}{I_i I_j} \\ &= M_{ij} \end{aligned}$$

where use has been made of the symmetry of the energy (demonstrated in the previous section).

Appendix D

Derivation of the Intercoil Force Expressions

The expression for the force on coil i due to all other coils can be easily compute from

$$\mathbf{F} = -\nabla_i U_t$$

where U_t is the total magnetic energy of the system. The total energy, in turn, can be written as

$$U_t = \sum_{i=1}^N \sum_{j=1}^N U_{j \rightarrow i}$$

where N is the total number of coils in the system and $U_{j \rightarrow i}$ is the magnetic energy associated with the two components i and j . For the simple case of $N = 2$, this gives

$$U_t = U_{1 \rightarrow 1} + U_{2 \rightarrow 1} + U_{1 \rightarrow 2} + U_{2 \rightarrow 2}$$

Since

$$U_{i \rightarrow j} = U_{j \rightarrow i}$$

the total energy of the system is given by

$$U_t = U_{1 \rightarrow 1} + 2U_{2 \rightarrow 1} + U_{2 \rightarrow 2}$$

Taking the gradient of the energy with respect to coil 1 gives

$$\nabla_1 U_t = \nabla_1 U_{1 \rightarrow 1} + 2\nabla_1 U_{2 \rightarrow 1}$$

The $\nabla_1 U_{1 \rightarrow 1}$ gives the self-force of the coil, and the $\nabla_1 U_{2 \rightarrow 1}$ term yields the interaction force on coil 1 due to coil 2.

In this appendix, the explicit relations used to compute the forces on a coil are derived from the magnetic energy. This will be carried out first for the filamentary current case, and then for the more general case of distributed currents.

D.1 Filamentary Currents

D.1.1 Force Between Two Coils

The interaction energy of a filamentary current I_i in the magnetic field produced by another filamentary current I_j is given by

$$U_{j \rightarrow i} = \frac{\mu_0 I_i I_j}{4} R_i R_j G(R_i, Z_i; R_j, Z_j)$$

where

$$\begin{aligned} G(R_i, Z_i; R_j, Z_j) &= \frac{2A}{R_i R_j} \left[\left(1 - \frac{k^2}{2}\right) K(k) - E(k) \right] \\ A^2 &= (R_i + R_j)^2 + (Z_i - Z_j)^2 \\ k^2 &= \frac{4R_i R_j}{A^2} \end{aligned}$$

The ∇_i operator is given by

$$\nabla_i = \mathbf{e}_R \frac{\partial}{\partial R_i} + \mathbf{e}_Z \frac{\partial}{\partial Z_i}$$

where the \mathbf{e}_ϕ component has been neglected due to toroidal symmetry. This gives

$$\mathbf{F} = \mathbf{e}_R \frac{\partial U_{j \rightarrow i}}{\partial R_i} + \mathbf{e}_Z \frac{\partial U_{j \rightarrow i}}{\partial Z_i}$$

Concentrating on the \mathbf{e}_R component first yields

$$\begin{aligned} \frac{\partial U_{j \rightarrow i}}{\partial R_i} &= \frac{\mu_0 I_i I_j}{2} \frac{\partial}{\partial R_i} \left\{ A \left[\left(1 - \frac{k^2}{2}\right) K(k) - E(k) \right] \right\} \\ &= \frac{\mu_0 I_i I_j}{2} \left\{ \frac{\partial A}{\partial R_i} \left[\left(1 - \frac{k^2}{2}\right) K(k) - E(k) \right] \right. \\ &\quad \left. + A \frac{\partial}{\partial k} \left[\left(1 - \frac{k^2}{2}\right) K(k) - E(k) \right] \frac{\partial k}{\partial R_i} \right\} \end{aligned}$$

From the definitions of A and k given above,

$$\begin{aligned}\frac{\partial A}{\partial R_i} &= \frac{R_i + R_j}{A} \\ \frac{\partial k}{\partial R_i} &= \frac{2A^2 R_j - 4R_i R_j (R_i + R_j)}{kA^4}\end{aligned}$$

Next,

$$\frac{\partial}{\partial k} \left[\left(1 - \frac{k^2}{2}\right) K(k) - E(k) \right] = -kK(k) + \left(1 - \frac{k^2}{2}\right) \frac{\partial K(k)}{\partial k} - \frac{\partial E(k)}{\partial k}$$

The derivatives of the elliptic integrals $K(k)$ and $E(k)$ are given by the identities

$$\begin{aligned}\frac{\partial K(k)}{\partial k} &= \frac{E(k)}{k(1-k^2)} - \frac{K(k)}{k} \\ \frac{\partial E(k)}{\partial k} &= \frac{E(k) - K(k)}{k}\end{aligned}$$

Substituting the elliptic integral derivatives and simplifying results in

$$\frac{\partial}{\partial k} \left[\left(1 - \frac{k^2}{2}\right) K(k) - E(k) \right] = \frac{k}{2} \left[\frac{E(k)}{1-k^2} - K(k) \right]$$

Incorporating this result and the partial derivatives of A and k into the derivative of the energy gives

$$\begin{aligned}\frac{\partial U_{j \rightarrow i}}{\partial R_i} &= \frac{\mu_0 I_i I_j}{2} \frac{R_i + R_j}{A} \left\{ \left[\left(1 - \frac{k^2}{2}\right) K(k) - E(k) \right] \right. \\ &\quad \left. + \left(\frac{R_j}{R_i + R_j} - \frac{k^2}{2} \right) \left[\frac{E(k)}{1-k^2} - K(k) \right] \right\}\end{aligned}$$

Using the definition of k^2 and simplifying results in

$$\frac{\partial U_{j \rightarrow i}}{\partial R_i} = \frac{\mu_0 I_i I_j}{2} \frac{R_i + R_j}{A} \left\{ K(k) \left[\frac{R_i}{R_i + R_j} \right] + \frac{E(k)}{1-k^2} \left[\frac{k^2}{2} - \frac{R_i}{R_i + R_j} \right] \right\}$$

While the various values of A , k , $K(k)$ and $E(k)$ are computed, the quantity $\frac{\partial U_{j \rightarrow i}}{\partial R_j}$ should be computed. The resulting expression is given by

$$\frac{\partial U_{j \rightarrow i}}{\partial R_j} = \frac{\mu_0 I_i I_j}{2} \frac{R_i + R_j}{A} \left\{ K(k) \left[\frac{R_j}{R_i + R_j} \right] + \frac{E(k)}{1-k^2} \left[\frac{k^2}{2} - \frac{R_j}{R_i + R_j} \right] \right\}$$

The derivation of the e_z component of the force is similar. Taking the Z_i derivatives of A and k ,

$$\begin{aligned}\frac{\partial A}{\partial Z_i} &= \frac{Z_i - Z_j}{A} \\ \frac{\partial k}{\partial Z_i} &= -\frac{4R_i R_j (Z_i - Z_j)}{kA^4}\end{aligned}$$

The Z_i derivative of the energy is then given by

$$\frac{\partial U_{j \rightarrow i}}{\partial Z_i} = \frac{\mu_0 I_i I_j}{2} \frac{Z_i - Z_j}{A} \left\{ \left[\left(1 - \frac{k^2}{2}\right) K(k) - E(k) \right] - \frac{2R_i R_j}{A^2} \left[\frac{E(k)}{1 - k^2} - K(k) \right] \right\}$$

Simplifying this expression results in

$$\frac{\partial U_{j \rightarrow i}}{\partial Z_i} = \frac{\mu_0 I_i I_j}{2} \frac{Z_i - Z_j}{A} \left[K(k) + \frac{E(k)}{1 - k^2} \left(\frac{k^2}{2} - 1 \right) \right]$$

For the case of the \mathbf{e}_z component, it can be shown that

$$\frac{\partial U_{j \rightarrow i}}{\partial Z_j} = -\frac{\partial U_{j \rightarrow i}}{\partial Z_i}$$

Thus, the total force on coil i due to coil j is given by

$$\begin{aligned} \mathbf{F}_{j \rightarrow i} &= \mu_0 I_i I_j \frac{R_i + R_j}{A} \left\{ K(k) \left[\frac{R_i}{R_i + R_j} \right] + \frac{E(k)}{1 - k^2} \left[\frac{k^2}{2} - \frac{R_i}{R_i + R_j} \right] \right\} \mathbf{e}_R \\ &+ \mu_0 I_i I_j \frac{Z_i - Z_j}{A} \left\{ K(k) + \frac{E(k)}{1 - k^2} \left(\frac{k^2}{2} - 1 \right) \right\} \mathbf{e}_z \end{aligned} \quad (\text{D.1})$$

and the force on coil j due to coil i is given by

$$\begin{aligned} \mathbf{F}_{i \rightarrow j} &= \mu_0 I_i I_j \frac{R_i + R_j}{A} \left\{ K(k) \left[\frac{R_j}{R_i + R_j} \right] + \frac{E(k)}{1 - k^2} \left[\frac{k^2}{2} - \frac{R_j}{R_i + R_j} \right] \right\} \mathbf{e}_R \\ &- \mu_0 I_i I_j \frac{Z_i - Z_j}{A} \left\{ K(k) + \frac{E(k)}{1 - k^2} \left(\frac{k^2}{2} - 1 \right) \right\} \mathbf{e}_z \end{aligned}$$

D.1.2 Self Force of a Filamentary Current

The magnetic energy of a single filamentary coil interacting with its own magnetic field is expressed as

$$U_{i \rightarrow i} = \frac{\mu_0}{2} I_i^2 R_i \left[\ln \left(\frac{8R_i}{a} \right) - 2 \right]$$

The gradient of this expression can be computed directly and is given by

$$\nabla_i U_{i \rightarrow i} = \mathbf{e}_R \frac{\mu_0}{2} I_i^2 \left[\ln \left(\frac{8R_i}{a} \right) - 1 \right]$$

Computing the self force of this coil results in

$$\mathbf{F}_{i \rightarrow i} = \frac{\mu_0}{2} I_i^2 \left[\ln \left(\frac{8R_i}{a} \right) - 1 \right] \mathbf{e}_R \quad (\text{D.2})$$

D.2 Distributed Currents

D.2.1 Force Between Two Coils

The interaction energy of a distributed current J_i in the magnetic field produced by a current J_j is given by

$$\begin{aligned} U_{j \rightarrow i} &= \frac{1}{2} \int_V \mathbf{J}_i(\mathbf{r}) \cdot \mathbf{A}_j(\mathbf{r}) d\tau \\ &= \frac{\mu_0 J_i J_j}{4} \int_{Z_i - \frac{h_i}{2}}^{Z_i + \frac{h_i}{2}} \int_{R_i - \frac{w_i}{2}}^{R_i + \frac{w_i}{2}} \int_{Z_j - \frac{h_j}{2}}^{Z_j + \frac{h_j}{2}} \int_{R_j - \frac{w_j}{2}}^{R_j + \frac{w_j}{2}} r r' G(r, z; r', z') dr' dz' dr dz \end{aligned}$$

It has been shown that [23]

$$\frac{d}{d\alpha} \int_{u_0(\alpha)}^{u_1(\alpha)} f(x, \alpha) dx = f(u_1, \alpha) \frac{du_1}{d\alpha} - f(u_0, \alpha) \frac{du_0}{d\alpha} + \int_{u_0(\alpha)}^{u_1(\alpha)} f_\alpha(x, \alpha) dx \quad (\text{D.3})$$

with the proviso that $u_0(\alpha)$ and $u_1(\alpha)$ are differentiable and $f(x, \alpha)$, and $f_\alpha(x, \alpha)$ are continuous.

Using this expression to compute $F_{j \rightarrow i}$ results in

$$\begin{aligned} F_{j \rightarrow i} &= \mathbf{e}_R \frac{\mu_0 J_i J_j}{2} \int_{Z_i - \frac{h_i}{2}}^{Z_i + \frac{h_i}{2}} \int_{Z_j - \frac{h_j}{2}}^{Z_j + \frac{h_j}{2}} \int_{R_j - \frac{w_j}{2}}^{R_j + \frac{w_j}{2}} (R_i + \frac{w_i}{2}) r' G(R_i + \frac{w_i}{2}, z; r', z') dr' dz' dz \\ &\quad - \mathbf{e}_R \frac{\mu_0 J_i J_j}{2} \int_{Z_i - \frac{h_i}{2}}^{Z_i + \frac{h_i}{2}} \int_{Z_j - \frac{h_j}{2}}^{Z_j + \frac{h_j}{2}} \int_{R_j - \frac{w_j}{2}}^{R_j + \frac{w_j}{2}} (R_i - \frac{w_i}{2}) r' G(R_i - \frac{w_i}{2}, z; r', z') dr' dz' dz \\ &\quad + \mathbf{e}_Z \frac{\mu_0 J_i J_j}{2} \int_{R_i - \frac{w_i}{2}}^{R_i + \frac{w_i}{2}} \int_{Z_j - \frac{h_j}{2}}^{Z_j + \frac{h_j}{2}} \int_{R_j - \frac{w_j}{2}}^{R_j + \frac{w_j}{2}} r r' G(r, Z_i + \frac{h_i}{2}; r', z') dr' dz' dr \\ &\quad - \mathbf{e}_Z \frac{\mu_0 J_i J_j}{2} \int_{R_i - \frac{w_i}{2}}^{R_i + \frac{w_i}{2}} \int_{Z_j - \frac{h_j}{2}}^{Z_j + \frac{h_j}{2}} \int_{R_j - \frac{w_j}{2}}^{R_j + \frac{w_j}{2}} r r' G(r, Z_i - \frac{h_i}{2}; r', z') dr' dz' dr \end{aligned} \quad (\text{D.4})$$

D.2.2 Self Force of a Distributed Current

The energy of a single distributed current interacting with its own magnetic field is found from

$$\begin{aligned} U_{i \rightarrow i} &= \frac{1}{2} \int_V \mathbf{J}_i(\mathbf{r}) \cdot \mathbf{A}_i(\mathbf{r}) d\tau \\ &= \frac{\mu_0 J_i^2}{4} \int_{Z_i - \frac{h_i}{2}}^{Z_i + \frac{h_i}{2}} \int_{R_i - \frac{w_i}{2}}^{R_i + \frac{w_i}{2}} \int_{Z_i - \frac{h_i}{2}}^{Z_i + \frac{h_i}{2}} \int_{R_i - \frac{w_i}{2}}^{R_i + \frac{w_i}{2}} r r' G(r, z; r', z') dr' dz' dr dz \end{aligned}$$

Using equation D.3 to compute the gradient of this expression gives:

$$\begin{aligned} \frac{\partial U_{i \rightarrow i}}{\partial R_i} &= \frac{\mu_0 J_i^2}{4} \int_{Z_i - \frac{w_i}{2}}^{Z_i + \frac{w_i}{2}} \int_{Z_i - \frac{h_i}{2}}^{Z_i + \frac{h_i}{2}} \int_{R_i - \frac{w_i}{2}}^{R_i + \frac{w_i}{2}} (R_i + \frac{w_i}{2}) r' G(R_i + \frac{w_i}{2}, z; r', z') dr' dz' dz \\ &\quad - \frac{\mu_0 J_i^2}{4} \int_{Z_i - \frac{w_i}{2}}^{Z_i + \frac{w_i}{2}} \int_{Z_i - \frac{h_i}{2}}^{Z_i + \frac{h_i}{2}} \int_{R_i - \frac{w_i}{2}}^{R_i + \frac{w_i}{2}} (R_i - \frac{w_i}{2}) r' G(R_i - \frac{w_i}{2}, z; r', z') dr' dz' dz \\ &\quad + \frac{\mu_0 J_i^2}{4} \int_{Z_i - \frac{w_i}{2}}^{Z_i + \frac{w_i}{2}} \int_{R_i - \frac{w_i}{2}}^{R_i + \frac{w_i}{2}} \int_{Z_i - \frac{h_i}{2}}^{Z_i + \frac{h_i}{2}} r (R_i + \frac{w_i}{2}) G(r, z; R_i + \frac{w_i}{2}, z') dz' dr dz \\ &\quad - \frac{\mu_0 J_i^2}{4} \int_{Z_i - \frac{w_i}{2}}^{Z_i + \frac{w_i}{2}} \int_{R_i - \frac{w_i}{2}}^{R_i + \frac{w_i}{2}} \int_{Z_i - \frac{h_i}{2}}^{Z_i + \frac{h_i}{2}} r (R_i - \frac{w_i}{2}) G(r, z; R_i - \frac{w_i}{2}, z') dz' dr dz \end{aligned}$$

where conservation of flux has resulted in a sign reversal.

The final expression for the self-force is found by making use of the symmetry relations for G developed in Appendix C and relabeling r as r' in the last two integrals simplifies the preceding expression to

$$\begin{aligned} \frac{\partial U_{i \rightarrow i}}{\partial R_i} &= \frac{\mu_0 J_i^2}{2} \int_{Z_i - \frac{w_i}{2}}^{Z_i + \frac{w_i}{2}} \int_{Z_i - \frac{h_i}{2}}^{Z_i + \frac{h_i}{2}} \int_{\alpha}^{\beta} \beta r' G(\beta, z; r', z') dr' dz' dz \\ &\quad - \frac{\mu_0 J_i^2}{2} \int_{Z_i - \frac{w_i}{2}}^{Z_i + \frac{w_i}{2}} \int_{Z_i - \frac{h_i}{2}}^{Z_i + \frac{h_i}{2}} \int_{\alpha}^{\beta} \alpha r' G(\alpha, z; r', z') dr' dz' dz \end{aligned} \quad (D.5)$$

where α and β are constants given by:

$$\begin{aligned} \alpha &= R_i - \frac{w_i}{2} \\ \beta &= R_i + \frac{w_i}{2} \end{aligned}$$

Appendix E

Gaussian Quadrature

In this appendix, the Gaussian integration algorithm is reviewed. The algebraic transformations required to evaluate the various integrals presented in Appendix D are described and, as an example, Equation D.5 is expressed in terms of those transformations.

Most numerical integration (quadrature) schemes require that the values of the integrand be known at evenly spaced points (e.g. the Newton-Cotes formulae). This works well for cases where the integrand is known or even where the exact functional form of the integrand is unknown and only a set of discrete values are available for integration. For cases where the functional form of the integrand is known, however, it is possible to determine the points where the integrand is to be evaluated such that the accuracy of the scheme is increased. The purpose of Gaussian quadrature is to find an optimal manner for determining these points.

Gaussian quadrature relies on orthogonal functions to determine the optimal points. Of the schemes available, the one chosen here uses Legendre polynomials, which are orthogonal in the region $[-1, 1]$. This gives

$$\int_{-1}^1 P(x) dx = \sum_{i=1}^n c_i P(x_i) \quad (\text{E.1})$$

where the x_i are the roots of the Legendre polynomial of degree n and the c_i are normalization coefficients. The values of x_i and c_i for many values of n are tabulated in [24]. This scheme is exact for all polynomials of degree at most $2n - 1$ and has an error of

$$E_t = \frac{2^{2n+1} [(n)!]^4}{(2n+1)[(2n)!]^3} f^{(2n)}(x)$$

where n is the number of points used for quadrature, $f^{(2n)}(x)$ is the $2n$ th derivative of $f(x)$, and x is in the region $[-1, 1]$.

The integral in equation E.1 has limits of $[-1, 1]$. Any set of limits $[a, b]$ in x can be mapped into $[-1, 1]$ in α by the transformation

$$\alpha = \frac{2}{b-a} \left[x - \frac{b+a}{2} \right]$$

so that

$$\int_a^b f(x) dx = \frac{b-a}{2} \int_{-1}^1 f\left(\frac{b+a}{2} + \frac{b-a}{2}\alpha\right) d\alpha$$

Throughout this thesis, the current density across a coil has been assumed constant:

$$J_i = \frac{I_i}{w_i h_i}$$

Combining this with the previous results allows us to write equation D.5 as

$$\begin{aligned} \mathbf{F} = & \mathbf{e}_\rho \frac{\mu_0 I_i^2}{2} \frac{1}{8w_i} \int_{-1}^1 \int_{-1}^1 \int_{-1}^1 \left(R_i + \frac{w_i}{2}\right) g(\beta) G\left(R_i + \frac{w_i}{2}, f(\alpha); g(\beta), h(\gamma)\right) d\beta d\gamma d\alpha \\ & - \mathbf{e}_\rho \frac{\mu_0 I_i^2}{2} \frac{1}{8w_i} \int_{-1}^1 \int_{-1}^1 \int_{-1}^1 \left(R_i - \frac{w_i}{2}\right) g(\beta) G\left(R_i - \frac{w_i}{2}, f(\alpha); g(\beta), h(\gamma)\right) d\beta d\gamma d\alpha \end{aligned}$$

where

$$\begin{aligned} f(\alpha) &= Z_i + \frac{h_i}{2}\alpha \\ g(\beta) &= R_i + \frac{w_i}{2}\beta \\ h(\gamma) &= Z_i + \frac{h_i}{2}\gamma \end{aligned}$$

The rapid convergence of this quadrature scheme is clearly illustrated in Figure E-1, where the coefficient of the self-force ($\frac{F_{i-i}}{\mu_0 I_i^2}$) of a coil with $R_c = 0.50$, $Z_c = 0.00$, $w = 0.05$ and $h = 0.05$ is plotted as a function of the number of quadrature points (n) used. The rapid convergence is especially interesting since the number of computations required to compute the force scales as n^3 . For example, the self-force coefficient computed with 8 points is 2.095841, while that for 100 points is 2.092711. The result of the 8 point scheme is only 0.15 per cent greater than the result of the 100 point scheme, and requires approximately $5 \cdot 10^{-4}$ as much time to compute. Because of the reasonable accuracy and speed of the 8 point scheme, it is used throughout the program to compute the required triple integrals.

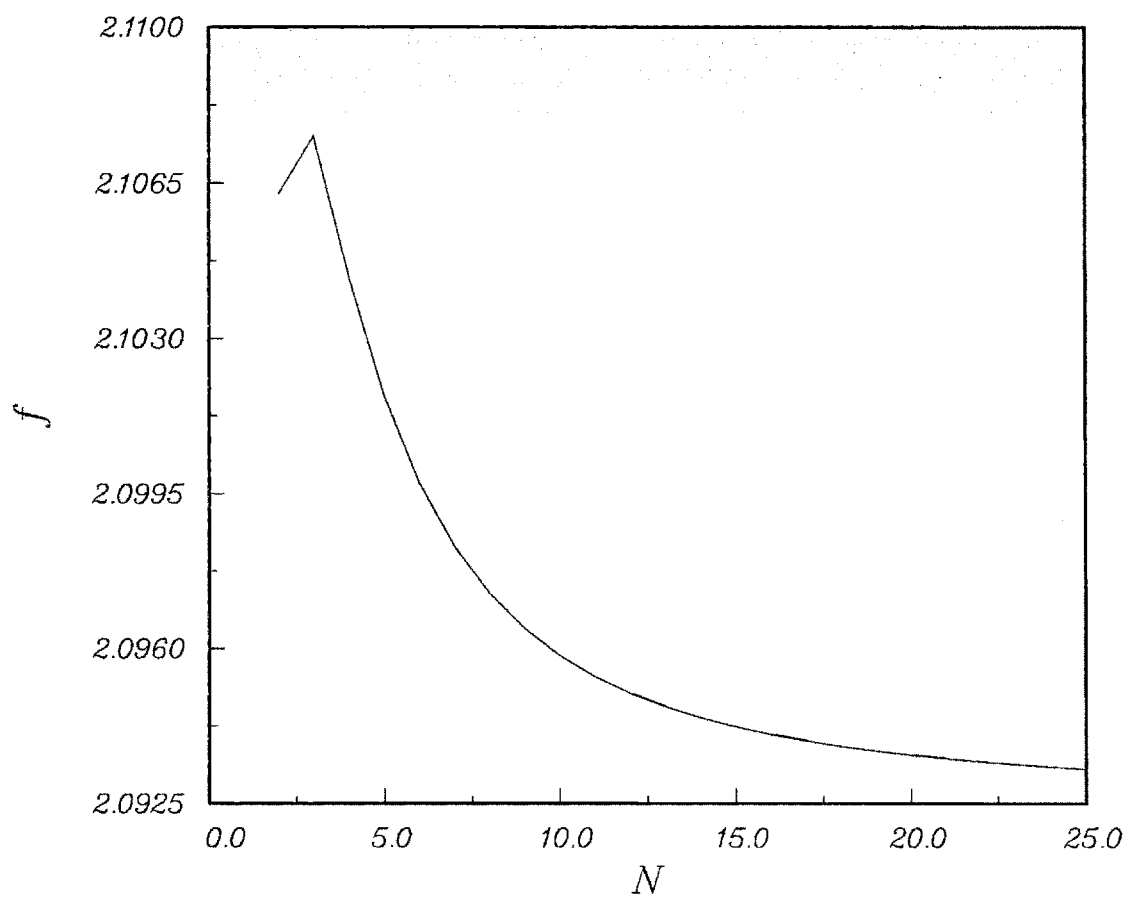


Figure E-1: Self-force coefficient as a function of the number of quadrature points used.

Bibliography

- [1] T. Baumeister, E. A. Avallone, and T. Baumeister III, editors. *Marks' Standard Handbook for Mechanical Engineers*, pages 5-2 – 5-51. McGraw-Hill Book Company, eighth edition, 1978.
- [2] Richard L. Burden, J. Douglas Faires, and Albert C. Reynolds. *Numerical Analysis*, pages 448–453. PWS Publishers, second edition, 1981.
- [3] J. P. Freidberg. *Ideal Magnetohydrodynamics*, pages 59 – 61. Plenum Press, 1987.
- [4] J. P. Freidberg. *Ideal Magnetohydrodynamics*, pages 86–87. Plenum Press, 1987. Problem 4.5.
- [5] J. P. Freidberg and W. Grossman. Magnetohydrodynamic stability of a sharp boundary model of tokamak. *Physics of Fluids*, 18(11):1494, 1975.
- [6] J. P. Freidberg, W. Grossman, and F. A. Haas. Stability of a high- β , $l = 3$ stellarator. *Physics of Fluids*, 19(10):1599, 1976.
- [7] J. P. Freidberg and F. A. Haas. Kink instabilities in a high- β tokamak with elliptic cross section. *Physics of Fluids*, 17(2):440, 1974.
- [8] P. E. Gill, W. Murray, and M. H. Wright. *Practical Optimization*, pages 167–182. Academic Press, 1981.
- [9] P. E. Gill, W. Murray, and M. H. Wright. *Practical Optimization*, pages 1–5. Academic Press, 1981.
- [10] I. S. Gradshteyn and I. M. Ryzhik. *Table of Integrals, Series, and Products*, page 907. Academic Press, fourth edition, 1980.

- [11] S. P. Hakkarainen and J. P. Freidberg. *Reconstruction of Vacuum Flux Surfaces from Diagnostic Measurements in a Tokamak*. Technical Report, Massachusetts Institute of Technology, 1987. M.I.T. Report PFC/RR-87-2.
- [12] Scott W. Haney. *Methods for the Design and Optimization of Shaped Tokamaks*. PhD thesis, Massachusetts Institute of Technology, May 1988.
- [13] Scott W. Haney. *Methods for the Design and Optimization of Shaped Tokamaks*. PhD thesis, Massachusetts Institute of Technology, May 1988. pages 105 – 141.
- [14] Scott W. Haney. *Methods for the Design and Optimization of Shaped Tokamaks*. PhD thesis, Massachusetts Institute of Technology, May 1988. pages 128 – 132.
- [15] Scott W. Haney. *Methods for the Design and Optimization of Shaped Tokamaks*. PhD thesis, Massachusetts Institute of Technology, May 1988. pages 93 – 104.
- [16] F. B. Hildebrand. *Advanced Calculus for Applications*, pages 357–359. Prentice-Hall, Inc., second edition, 1976.
- [17] F. B. Hildebrand. *Advanced Calculus for Applications*, pages 352–354. Prentice-Hall, Inc., second edition, 1976.
- [18] F. B. Hildebrand. *Advanced Calculus for Applications*, pages 215–223. Prentice-Hall, Inc., second edition, 1976.
- [19] J. P. Holman. *Heat Transfer*, pages 35 – 37. McGraw-Hill Book Company, fifth edition, 1981.
- [20] J. Mathews and R. L. Walker. *Mathematical Methods of Physics*, page 260. Benjamin/Cummings Publishing Company, second edition, 1970.
- [21] P. B. Powell, editor. *Planning for Software Validation, Verification, and Testing*. U.S. Dept. of Commerce, National Bureau of Standards, 1982. NBS Special Publication; 500-98.
- [22] W. H. Press, B. P. Flannery, S. A. Teuolsky, and W. T. Vetterling. *Numerical Recipes in C*, page 29. Cambridge University Press, 1988.
- [23] I.S. Sokolnikoff and R. M. Redheffer. *Mathematics of Physics and Modern Engineering*, pages 347–350. McGraw-Hill Book Company, second edition, 1966.

- [24] A. H. Stroud and D. Secrest. *Gaussian Quadrature Formulas*. Prentice-Hall, Inc., 1966.
- [25] R. K. Wangsness. *Electromagnetic Fields*, pages 323–326. John Wiley & Sons, 1979.